IPP-Report

Max-Planck-Institut für Plasmaphysik

Felix Warmer

Reactor Extrapolation of Wendelstein 7-X

IPP 13/21
March, 2013

UNIVERSITÄT LEIPZIG
FAKULTÄT FÜR PHYSIK UND GEOWISSENSCHAFTEN
MAX-PLANCK-INSTITUT FÜR PLASMAPHYSIK

Reactor Extrapolation of Wendelstein 7-X

Felix Warmer

Master Thesis

First Reviewer: Prof. Dr. Dr. h.c. Bernd Rauschenbach
Second Reviewer: Priv.-Doz. Dr. Andreas Dinklage
Submission: 3rd January 2013

Reactor Extrapolation of Wendelstein 7-X

Felix Warmer

Master Thesis

Universität Leipzig
Fakultät für Physik und Geowissenschaften
Conducted at the Max-Planck-Institut für Plasmaphysik, Greifswald

Abstract

An ultimate goal of fusion research is to demonstrate the feasibility of economic production of electricity. Consequently, the more specified envisaged fusion reactors are, the more efficient can the experimental programs of research devices on the way to fusion be planned. Key experiments are on the so-called Tokamak line - ITER [1] and on the so-called Stellarator line of magnetic confinement - Wendelstein 7-X [2].

This work contributes to this development by upscaling W7-X to reactor-like parameters. Upscalings are usually done using zero-dimensional approximations as, e.g., in Tokamak DEMO studies [3]. Here, the method used in [3] was adopted for Stellarators using the ISS04 confinement scaling. The results employing the 0-D scaling showed higher net electric power output of helium cooling due to the higher thermal conversion efficiency compared to conventional water cooling. The calculations demonstrated also a strong increase of performance if advanced magnet technology would be employed, e.g. Nb_3Sn superconductors. Furthermore, if magnetic configurations could be optimised to lead to longer confinement times by a factor of 1.5, the radius required for ignition would be drastically reduced from around $R \approx 20$ m to 14 m for an HSR4/18 reactor parameters [4].

In addition to the 0-D studies, a one dimensional code [5] was employed to study Stellarator transport effects and the impact of profiles on reactor-like W7-X magnetic configurations. The resulting 1-D simulations showed discrepancies to the 0-D scalings especially in terms of confinement time. It could be shown that the transport characteristics of the Stellarator $1/\nu$-regime for the electrons and $\sqrt{\nu}$-regime for the ions needs to be accounted while the ISS04 scaling is compliant with the collisional plateau regime. This finding could explain the differences of the 0-D and the 1-D approach. Addressing profile effects, hollow density profiles [6] were found to result in positive electric fields. This Stellarator specific effect could be beneficial with respect to helium ash exhaust and impurity transport but requires further exploration.

Finally, the 1-D code, incorporated with self-consistent fusion power [5], has been used. A technologically conservative and an advanced scenario were simulated. Such an advancement would reduce the reactor size significantly

from around $R \approx 22$ m to 16 m. The simulation results indicate that the 1-D results approach the 0-D findings with larger plasma volumes. Along those scenarios a comparison was made regarding profile form and anomalous transport models. The results showed, that a hollow density profile [6] decreases the overall performance of a reactor slightly and may again develop a positive electric field in the core region of the plasma. Although little in known about the anomalous transport in Stellarators, the models showed, that a high anomalous heat and particle flux have a great impact on reactor performance. Therefore more reliable models of anomalous transport are of large importance for the reactor extrapolation of Stellarators.

Zusammenfassung

Das höchste Ziel der Fusionsforschung ist der Nachweis von ökonomischer Stromerzeugung. Um die experimentellen Programme von Forschungsreaktoren auf dem Weg zur Fusion effizient zu planen, ist es daher notwendig die angstrebten Fusionsrekatoren genau zu spezifizieren. Schlüsselexperimente sind in diesem Rahmen auf der sogenannten Tokamak-Linie das Experiment - ITER [1] und auf der sogenannten Stellarator-Linie des magnetischen Einschlusses - Wendelstein 7-X [2].

Diese Arbeit trägt zu diesem Vorhaben durch das Aufskalieren von W7-X zu Reaktor relevanten Parametern bei. Solche Aufskalierungen werden normalerweise mit null-dimensionalen Näherungen gemacht wie z.B. in Tokamak DEMO Studien [3]. In dieser Arbeit wurde die Methode von [3] für die Anwendung auf Stellaratoren adaptiert unter Benutzung der ISS04 Einschlussskalierung. Die Ergebnisse dieser 0-D Skalierung zeigten eine höhere netto elektrische Leistung von Heliumkühlung aufgrund ihrer höheren thermischen Konvertierungseffizienz gegenüber konventioneller Wasserkühlung. Die Rechnungen zeigten ebenso einen starken Anstieg der Reaktorleistung unter Verwendung von hochentwickelter Magnettechnologie, z.B. durch die Nutzung von Nb_3Sn Supraleitern. Wenn darüber hinaus Magnetfeldkonfigurationen weiter optimiert werden könnten um höhere Einschlusszeiten zu erreichen, z.b. um einen Faktor 1.5, würde sich der Radius der nötig ist, um ein Plasma zu zünden, deutlich von $R \approx 20$ m auf 14 m verkürzen für HSR4/18 Parameter [4].

Zusäztlich zu den 0-D Studien wurde ein ein-dimensionaler Code [5] eingesetzt um Stellarator Transporteffekte und den Einfluss von Profilen auf Reaktorähnliche W7-X Magnetfeldkonfigurationen zu studieren. Die Resultate der 1-D Simulationen zeigten Abweichungen zur 0-D Skalierung, besonders im Hinblick auf die Einschlusszeiten. Es konnte gezeigt werden, dass die Transportcharakteristiken des Stellarator $1/\nu$-Regimes der Elektronen und des $\sqrt{\nu}$-Regimes der Ionen berücksichtigt werden müssen, da die ISS04 Skalierung ähnlich wie das Plateau-Regime skaliert. Dieser Befund könnte den Unterschied zwischen den 0-D und den 1-D Rechnungen erklären. Bei der Untersuchung von Profileffekten stellte sich heraus, dass hohle Dichteprofile [6] ein positives

elektrischen Feld erzeugen können. Dieser Stellarator-spezifische Effekt könnte vorteilhaft für die Abfuhr von Helium-Asche und Verunreinigungen sein, erfordert aber weitere Erforschung.

Schließlich wurde der 1-D Code für weitere Benutzung mit selbstkonsistenter Fusionsleistung erweitert [5]. Ein technologisch konservatives und ein fortschrittliches Szenario wurden simuliert. Solch eine technische Erweiterung würde die benötigte Reaktorgröße deutlich von $R \approx 22$ m auf 16 m reduzieren. Die Simulationen deuten an, dass die 1-D Resultate sich den 0-D Werten für große Plasmavolumen annähern. Einhergehend mit diesen Szenarien wurden Vergleiche von Profilformen und anomalen Transportmodellen gemacht. Die Ergebnisse zeigten, dass hohle Dichteprofile [6] die generelle Leistung leicht reduzieren und auch hier zu positiven elektrischen Feldern im Plasmazentrum führen können. Obwohl nur wenig über den anomalen Transport in Stellaratoren bekannt ist, zeigten die Modelle, dass ein hoher anomaler Energie- und Teilchenfluss großen Einfluss auf die Reaktoreffizienz hat. Darum sind verlässlichere Modelle für den anomalen Transport von hoher Wichtigkeit für Reaktorextrapolationen von Stellaratoren.

Standing over the empty and destroyed world
we looked up to the sun - and were reborn

Preface

This work is submitted to the Fakultät für Physik und Geowissenschaften of the Universität Leipzig as a master thesis. It serves for the purpose of attaining the academic degree 'Master of Science'.

My deepest gratitude goes to Prof. Dr. Dr. h.c. Bernd Rauschenbach for the kind support and supervision from the Leipzig University and the possibility of this cooperation. Equally, I thank Prof. Dr. Robert Wolf and Priv.-Doz. Dr. Andreas Dinklage, who made it possible for me to write this thesis at the Max-Planck-Institut für Plasma Physik in Greifswald and supported me with many discussions, ideas and good advice.

I also wish to thank Dr. Yuriy Turkin, who provided me with his code and took so much time for explanations. With regard to theoretical aspects, I owe deep gratitude to Dr. Craig Beidler, who always had an open door for me and illuminated me with so much in-depth theoretical knowledge.

Additionally, I am grateful for a lot of advices from my friend Johannes Zähle.

Last but not least, I am indebted to my family for the comprehensive support and the large financial aid, which made this work possible at all.

Contents

Introduction

In the recent two hundred years our world has changed faster and more drastically than ever before. One major driver of this development was the human desire for 'prosperity' pursued through technological advancement. This led to the invention of cornerstone technologies, beginning with the steam engine and the resulting industrialisation. This rapid growth of technology was amplified with the introduction of electricity and its various applications. Through the exploitation of oil - using cars and planes our society changed and evolved to a point which is today referred to as the Information Age. The consequence of this development and our more and more refined technology, is an ever increasing demand for energy. It appears to be evident that a sufficient supply and availability of energy is a necessary condition for the development of societies. Figure 1 shows an attempt to quantify this statement. The human development index (being a composition of the life expectancy, education and income of a nation) is plotted against the energy consumption per person. This empirical relationship indicates that more developed countries also have a higher per capita energy demand.

Currently, the main global energy sources are (86 %) hydrocarbon fuels, namely coal, oil and gas. Hydroelectric and nuclear power contribute to 6 % each [8]. This fact, together with estimates for future energy needs, gives rise to several problems. The shortage of highly concentrated uranium resources as well as the reducing oil output known as Peak-Oil means that in the long term the energy demand can only be stilled by coal [9], given the technological possibilities of today. However, the huge amounts of carbon dioxide emission aligned with this scenario would at least double or triple the CO_2 concentration in our atmosphere in the next hundred years. A full understanding of the impact of CO_2 concentration in the atmosphere on the global temperature increase is lacking, but there is clear evidence that there is a strong correlation between temperature and CO_2 concentration. Today, the CO_2 concentration

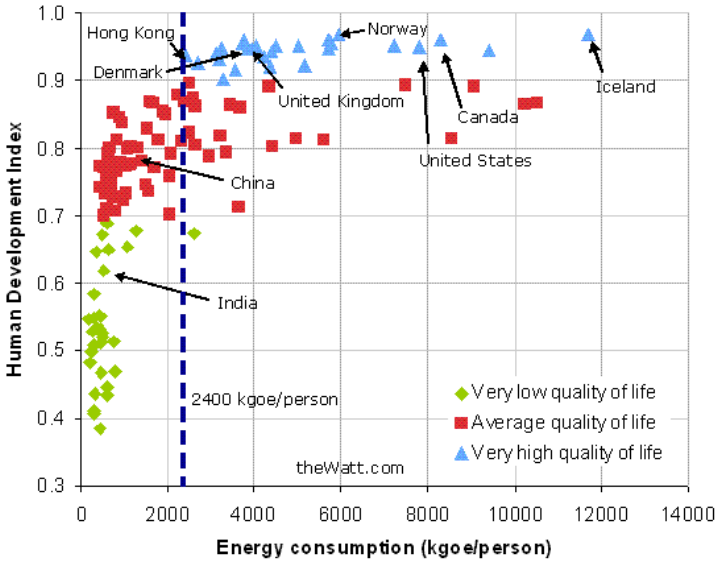

Figure 1: Human development index as defined in the United Nations Development Report in dependence of the per capita energy consumption for the year 2003 in units of kilogramme oil equivalent (kgoe) [7].

in our atmoshphere is around 390 ppm and thereby higher than ever before [10]. Consequently, current climate models predict a dramatic temperature increase and global climate changes in the next hundred years [11].

Confronted with these facts, the United Nations have started to take actions to reduce the emission of greenhouse gases, e.g. through the Kyoto Protocol. Associated with the climate problem is the concept of *sustainable development* as baseline for future national and international politics [9]. Nevertheless, especially the energy sector with its mainly conventional hydrocarbon sources is by nature in contradiction with sustainable development and therefore sustainable energy poses the greatest challenge for mankind. In this discussion, *fusion* can be regarded as an option for a possible future energy source with virtually unlimited supply of fuel, namely deuterium and lithium, making it one of the few sustainable energy sources [12]. Although a short-term ($<$ 20 years) impact of fusion power on the energy supply cannot be expected, the significance of the energy problem requires to investigate all options for sustainable energy sources.

Fusion in the first place made life on earth possible being the power source of the sun. The sun predominantly consists of hydrogen confined through the gravitational force. The high mass of the sun leads to high pressure in its

core region. Due to the high pressure and the high temperature, a part of the hydrogen is starting fusion. This is the beginning of the so-called proton-proton chain reaction. In the first step, the hydrogen fuses to deuterium setting free a positron and a neutrino. In the next step, deuterium and hydrogen fuses to ^{3}He and a gamma ray. Finally, ^{3}He fuses to two hydrogen atoms and one ^{4}He. The gamma rays of the fusion reactions follow a random walk through the bulk of the sun, loosing some energy at each step. When reaching the photosphere of the sun, the energy of of the gamma rays will be reduced to visible light escaping into space. The reactivity of the proton-proton chain, however, is very low due to the nuclear physics of the reaction and taking place at pressures too high to be for relevance on earth. The most suitable fusion reaction is the fusion of deuterium and tritium with a high reactivity, taking place at relatively low temperatures (10 . . . 20 keV).

$$\mathrm{D} + \mathrm{T} \longrightarrow \mathrm{n}\ (14\ \mathrm{MeV}) + \alpha\ (3.5\ \mathrm{MeV})$$

But even at temperatures around 10 . . . 20 keV the number of collisions which lead to fusion is some orders of magnitude smaller compared to the Coulomb collisions. This can clearly be seen in figure 2 showing, that the cross section of the Coulomb scattering is much higher than the fusion cross section of the D-T reaction at reasonable temperatures < 30 keV. To effectively use the energy which is needed to bring a D-T plasma to fusion conditions, it is essential to *confine* the charged particles long enough to allow a sufficient fraction of the particles to undergo a fusion reaction.

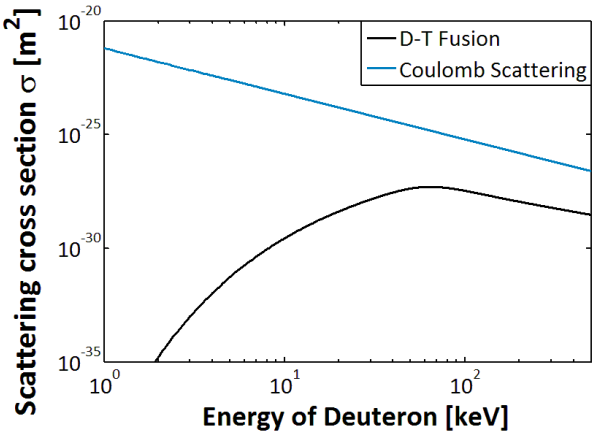

Figure 2: Cross section of Coulomb scattering in a fusion plasma and the corresponding fusion cross section of the D-T reaction [13].

The sun provides the confinement of the hydrogen by gravity, but to realise fusion on earth different concepts are required. One of the most promising concepts is magnetic confinement. The charged particles are bound to the magnetic field lines through the Lorentz force. But to avoid particle losses of linear devices, the magnetic field must be toroidally closed. As will be explained in section 2.1.4, this does not suffice to confine a plasma. In addition to the toroidal magnetic field component, a poloidal component is required to balance the particle drifts. In the field of magnetic confinement two different reactor types are leading candidates to create such a magnetic field, namely the *Tokamak* and the *Stellarator*. Both will be explained in section 2.1.4.

This work is dedicated to the Stellarator baseline where basic technical aspects of a reactor are introduced in chapter 1 in order to give the later explored physics an overall context. Following this, chapter 2 will explore the required physical background of magnetic confinement and plasma transport which is necessary for the chapters 3 and 4, where the Stellarator experiment *Wendelstein 7-X* (W7-X) will be used as basis for a physically orientated upscaling of the experiment to reactor size. This scaling study is investigated at first from a zero dimensional view in chapter 3 and is followed by an in-depth investigation in chapter 4 using a dedicated one dimensional code. In this context, transport regimes and the change of transport channels are studied under different parameters. The main results learned from this procedure will be summarised in chapter 5, followed by a brief outlook.

Chapter 1

Fusion Reactor and Technology

Although this work is dedicated to a physics-based extrapolation of a reactor, technical and engineering aspects are explored to define technological constraints and boundary conditions in the physical context. Therefore the first chapter shall introduce the conceptual design of a Stellarator fusion reactor and its key technologies. The explanations of this chapter are mainly based on Refs. [14, 15].

Reactor Concept

In contrast to a physics-based extrapolation, reactor design studies are devoted to identifying engineering problems and their impact on research and cost. Based on physics boundaries, engineering design studies determine required size and concepts of components. A conceptual sketch of such a Stellarator power plant can be seen in figure 1.1. In the centre of the figure the magnetic confined plasma can be seen where the fusion reactions are taking place. The resulting fusion power in form of alpha particles heats the plasma while the arising neutrons are going directly into the blanket. The neutrons not only deposit their energy in the blanket but also are meant to fuse with ^{7}Li to produce the fuel tritium. To protect the superconducting magnets from the not absorbed neutron flux, a shield adjacent to the blanket is required. Additionally the divertor, responsible for the particle exhaust, will be strongly heated by the plasma. A cooling system transfers the heat from the divertor and the blanket to a generator transforming it to electricity. Before going into the power grid some of the electrical power needs to be recirculated to operate all power plant facilities. Due to the radioactive nature of T, a closed cycle

is needed which brings the tritium from the blanket to the tritium cleaning facility as well as the particle exhaust from the divertor. The facility purifies the exhausts to pure deuterium and tritium which is then injected into the plasma as fuel. Besides that, a reactor needs an external heating source, e.g. ECRH, for the start-up phase of the reactor. The components of the reactor are held in place by a strong support structure enclosed by the outer vessel (not shown in the figure). All the relevant components seen in figure 1.1 will be discussed in more detail throughout the chapter.

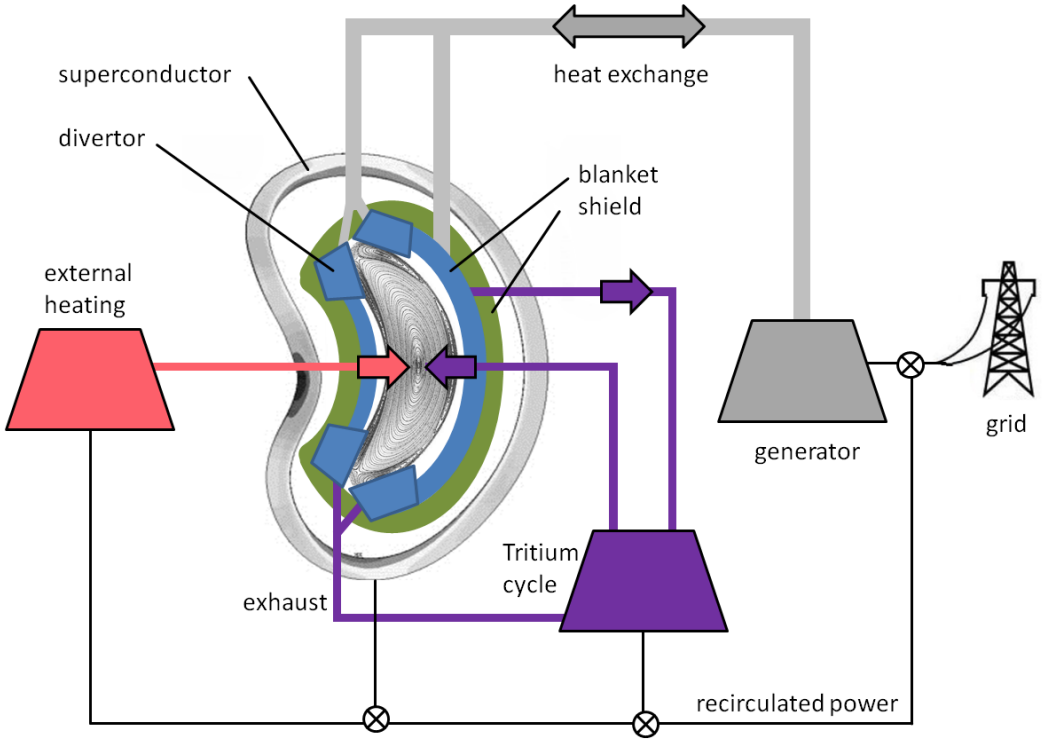

Figure 1.1: Conceptual sketch of a Stellarator power plant showing the radial build of the reactor with the most important components and the main facilities required to operate the reactor.

First Wall

As the name states, the *first wall* is the border separating the plasma from the actual vessel. The first wall must withstand the direct contact with radiation, charged particles and a high amount of neutron flux. In order to not contaminate the plasma, the first wall must also be as resistant as possible to

erosion, sputtering and blistering caused by nuclear transmutation reactions. Although the first wall will be replaced several times during the lifetime of the reactor, it must survive the high heat flux and thermal stresses over a period of years to be economically reasonable. Maintenance and replacement scenarios must therefore be incorporated from the beginning including remote handling necessary due to activation caused by the neutron flux passing through the first wall. Candidates for first wall materials are for example tungsten, ferritic steels or vanadium alloys.

Blanket and Shield

The *blanket* of a fusion reactor is one of the most important components since it is to breed the fuel for the fusion reactions. It is situated between the first wall and superconducting magnets. Because of the high fusion power output of a reactor, the blanket is exposed to severe amounts of radiation, both of electromagnetic and nuclear nature. The blanket must withstand the resulting thermal and chemical stresses reliably for long time periods to ensure economic operation of a plant and at the same time fulfill three major functions. It must shield the superconducting coils outside the blanket, convert the fusion energy into heat energy and breed tritium.

Due to the radiation and the 14 MeV neutrons the temperature in the blanket may be up to 900 K meaning liquid metals, e.g. LiPb, are likely to be used for heat transfer or as breeding material. To ensure sufficient production of tritium, neutron multipliers like ^{7}Li and Be could be used. The tritium must be safely extracted from the blanket and reprocessed to make it available for refuelling. Also large amounts of heat must be transferred to a generator using a cooling fluid or gas, e.g. water or helium. Influencing the aspects of lifetime - maintenance, repair, reassembly and safety criteria must be met.

Although the blanket absorbs most of the heat and the neutrons, an extra *shield* adjacent to the blanket is essential for protecting the more sensitive components. The shield is to moderate the neutron flux and to protect all outer components of the reactor from thermal flux and radiation. Depending on its design, a shield may consist of advanced borated ferritic steels or even silicon carbide. Some concepts also incorporate a graphite region between blanket and shield to reflect escaping neutrons back into the blanket.

Due to its massive nature consisting of high-technology parts, the blanket

and shield together is one of the most expensive components of the reactor and will have a major impact on safety and economic features. To ensure enough space for blanket and shield (1 . . . 1.5 m) restrictions are given for the minimal size of a fusion reactor.

Magnetic Field Coils

As reactors require a high field strength (10 . . . 12 T on the surface of a coil) to sufficiently confine the plasma, the coils must maintain large currents. This can only be done when the coil is in a superconducting state with the electrical resistivity dropping to almost zero. This state only occurs in a small operation window with respect to temperature and current density. To reach and use this state at high enough magnetic fields, the coils must be cooled with liquid helium to 4.2 K. One of the main problems arising from this necessity is to prevent the superconductor from reverting to the normal state, that is, to undergo a *quench*. In a quench the helium is heated too strongly accidentally forming a small film of helium vapour isolating the superconductor and finally heating up the coil. A sudden loss of superconductivity would follow requiring to dump the magnetic energy of the coils on resistors. To avoid damage to the coils in a quench, precautionary measures must be taken.

Figure 1.2: CAD casing of 3-D magnetic field coils of HELIAS 5-B. These figures appear courtesy of F. Schauer and K. Egorov, IPP Greifswald.

An engineering problem is the construction of Stellarator superconducting coils with their complex three-dimensional shape. Such a 3-D shape can be seen in figure 1.2 which shows the CAD model casing of superconducting coils of the HELIAS 5-B reactor. The challenging coils of W7-X were constructed

using niobium-titanium (NbTi) as superconducting material. To achieve even higher field strengths niobium-tin (Nb_3Sn) and niobium-aluminium (Nb_3Al) are considered. Such large fields would mean, that the coils of a reactor store an immense amount of magnetic energy during operation of up to 160 GJ. Moreover with charged coils very large forces are expected to act on the reactor structure of the order of several hundred MPa. To stabilise the components, a robust support structure is required compensating the strong magnetic forces.

Due to size, shape and material the superconducting coils of a Helias reactor are expected to be the most expensive investment of a Stellarator reactor. The magnetic field strength also has a major impact on the fusion power output as will be discussed in section 3.3 and 4.4.

Divertor

To ensure a steady-state operation of a fusion reactor, the accumulation of the fusion ash helium and first wall impurities must be prevented. This is done with the plasma facing *divertor* with its main functions being both the removal of particles and heat out of the plasma.

Due to the three-dimensional shape of a Stellarator, the placement of the divertor plates must be carried out carefully. Most recent concepts [16] exploit the existence of large magnetic islands at the boundary. This so-called island divertor concept [17] is designed to match the 3-D shape of the plasma. Therefore the divertor plates are located in the region where the islands are of maximal radial extent. The island itself and small angles of incidence of the magnetic field lines are envisaged to arrive at a uniform particle distribution on the divertor plates to avoid peaked loads [18]. Due to the strong radial temperature gradient, the arriving ions get cooled down near the divertor. But the high mobility of the electrons causes a negative potential on the divertor plates essentially accelerating the ions. The turbomolecular pumps which are located behind the divertor plates then remove the striking particles. Another concept for a Stellarator divertor is the helical divertor being tested at LHD [19].

Because of the direct interaction with the plasma, the divertor must withstand very high heat loads in continuous operation. Therefore the divertor must have a modular segmentation to allow for fast replacement. The question of possible materials is still under research but materials are expected to

endure no more than 10 MW/m^2.

Tritium Cycle

As already stated, the required tritium for the reactor operation is directly bred in the blanket. But tritium can also be found in the gas exhaust of the divertor pumped from the plasma. Due to the radioactive nature of tritium and to save the fuel for the fusion reactions a closed circulation cycle in the reactor is dedicated to tritium processing. The main function of this cycle is the safe and independent transport of the tritium enriched gases as well as their purification and isotope separation. The purification system removes all non-hydrogen isotope impurities like helium and metals. After this procedure the leftover hydrogen isotopes and its chemical bondings must be separated and split into tritium, deuterium and hydrogen streams. The pure tritium and deuterium can then be used for refuelling.

Refuelling

Due to the different transport mechanisms and the divertor pumping, the plasma will constantly loose fusion products and unburned fuel. In order to ensure continuous operation of the reactor those losses must be compensated by constant or cyclic refuelling.

It is also desirable to bring the fuel as close to the plasma axis as possible where the temperature is highest and most fusion reactions happen. An option for refuelling is possibly pellet injection, e.g. to shoot small D-T ice capsules into the plasma. This can only be done using advanced pellet injection techniques, e.g. railgun or pneumatic injection. First the deuterium and recycled tritium must be cooled and compressed to solid ice pellets which are, depending on technique, accelerated up to several km/s and shot into the plasma. To sustain a burning fusion plasma this procedure must be done at a sufficiently high frequency.

Plasma Heating

A fusion reactor can only efficiently work with temperatures higher than 10 keV. To reach this temperature in the first place an external heating system is required for the start-up phase. In the course of fusion research different heating concepts were developed but only the *electron cyclotron resonance*

heating (ECRH) is considered to be of relevance for a Stellarator reactor. This is done in a Stellarator fusion reactor with an array of *gyrotrons* which are designed so, that their emitted microwaves are of the same frequency as the electron gyration frequency in the magnetic field at the plasma core[1]. The gyrotron microwaves are transmitted to the reactor port and launched into the plasma. Then the electromagnetic waves are absorbed by the electrons and thermalised by collisions, effectively increasing the plasma temperature.

Once the plasma exceeds a certain temperature at which a significant amount of fusion takes place the produced 3.5 MeV alpha particles will start self-heating the plasma as they give up their energy in the process of 'slowing down'. When the power losses of the plasma are of the same magnitude as the heating power by alpha particles, the reactor is in equilibrium working in a steady state.

Balance of Plant

Along with the main heat generating system, a fusion plant needs, like every power plant, components for power conversion and distribution, generally known as *balance of plant* (BOP). Often only known from side remarks the balance of plant plays an important role for the reliable operation of a power plant. The objectives which must be achieved by the balance of plant is an efficient conversion of thermal power to electricity, reliable supply of electricity of the power plant components and effective operation of all auxiliary systems. To make a fusion power plant economical the balance of plant systems must work with high efficiency and availability at low construction costs. Conceptually the design of the balance of plant of a fusion power plant is similar to those of fission or conventional power plants although the use of a different coolant changes the structure of the balance of plant.

[1] It is also possible to use higher harmonics of the electron cylotron frequency, which is, e.g., done in W7-X, but not relevant for a fusion reactor due to the lower electron cut-off density.

Chapter 2

Theoretical background

Even if all particles are well confined by a magnetic field in a fusion device, plasma transport perpendicular to the field will occur. As the plasma volume at some point must have a cold boundary, a temperature gradient will always be present. Therefore thermodynamic forces are present in every fusion device and will cause transport. As confinement and transport and the underlying physics are of major interest for fusion reactors and their efficiency, this chapter introduces magnetic confinement and plasma transport in a general way.

2.1 Magnetic Confinement

The explanations used here are based on the work of Francis F. Chen [20] and the book of Robert J. Goldston and Paul H. Rutherford [21].

2.1.1 Particle Motion in Magnetic Field

If a particle with mass m and charge q is moving in an electric field with field vector $\mathbf{E}$ and in a magnetic field with flux density $\mathbf{B}$, the trajectory will be described by the equation

$$m\frac{\mathrm{d}\mathbf{v}}{\mathrm{d}t} = q\left(\mathbf{E} + \mathbf{v} \times \mathbf{B}\right). \tag{2.1}$$

The influence of the magnetic field on the particle is called the *Lorentz force*[1] which can be derived in the frame of the classical field theory [22]. It is hereby useful to define the particle velocity $\mathbf{v}_{\parallel}$ parallel to the magnetic field and $\mathbf{v}_{\perp}$

[1] In the english-speaking world the definition of the Lorentz force includes $\mathbf{E}$.

perpendicular to the magnetic field, fulfilling $v_\parallel^2 + v_\perp^2 = v^2$ and $\mathbf{v}_\parallel + \mathbf{v}_\perp = \mathbf{v}$. In the case of a homogeneous magnetic field $\mathbf{B}$ and in absence of an electric field, $\mathbf{E} = 0$, this relation is reduced to a differential equation having the form of an harmonic oscillator with the solution

$$\begin{aligned} \mathbf{r} &= \mathbf{r}_0 + \mathbf{r}_\parallel + \mathbf{r}_\perp, \\ \mathbf{r}_\parallel &= \mathbf{v}_\parallel \cdot t, \\ \mathbf{r}_\perp &= R(\omega_c\, t) \cdot \frac{\mathbf{v}_\perp}{\omega_c} \end{aligned} \tag{2.2}$$

for the trajectory $\mathbf{r}$ with the rotation matrix R. In this representation the projection of the motion in the plane perpendicular to $\mathbf{B}$ yields a circular path and the eigenfrequency of this circular motion is given the name *cyclotron frequency*

$$\omega_c = \frac{|q|\, B}{m} \tag{2.3}$$

and the radius is known as *Larmor-radius*[2]

$$r_L = \frac{v_\perp}{\omega_c} = \frac{m\, v_\perp}{|q|\, B}. \tag{2.4}$$

The particles can therefore move freely along the field line, but are bound to circular motion perpendicular to the magnetic field line. The axis of the circular motion is thus called *guiding centre*.

2.1.2 Classical Diffusion

A collision of a charged particle in a plasma with another particle will lead to an abrupt change of velocity and trajectory. Due to the high density of fusion plasmas, collisions occur often. Considering the central collision of particles of the same mass, they just exchange their orbits and the gyrocentres remain effectively unchanged. In an extreme case the velocity direction changes with 90 degree, which shifts the gyrocentres but leaves the centre of mass untouched. The diffusion due to equal particles is therefore minimal.

Completely different is the situation when particles of different mass collide. These collisions are in a fusion plasma in general between electrons and ions. Due to the mass difference, the electrons get reflected randomly. The ions on the other side get at every collision a small momentum leading to a random

[2]The Larmor-radius is often also called gyroradius or gyration-radius.

walk as described by *Einstein's Brownian movement*. This means that diffusion by collisions in a magnetically confined plasma is mainly due to the collisions between particles of unequal mass [21], but only as long as trapped particles are not considered.

It is evident, that the collisions are independent of each other and the direction of the deflection is random. Using methods of probability calculus it can be shown [21], that the diffusion coefficient

$$D = \frac{\langle \Delta x^2 \rangle}{2\Delta t} \tag{2.5}$$

is dependent on the mean quadratic step width. Classical collisional transport in plasmas employ the Larmor-radius for the step width and the time between two Coulomb collisions of particles of unequal mass for the time interval τ_{ei}. The resulting classic diffusion coefficient

$$D_{cl} = \frac{r_L^2}{\tau_{ei}} \tag{2.6}$$

however, is several orders of magnitude smaller then observed in experiments.

One reason for the deviation is due to the different drift motions in conjunction with inhomogeneous magnetic fields. The resulting trapped particles have much larger step widths than the Larmor-radius. Transport accounting for the structure of the magnetic field is called *neoclassical transport*.

2.1.3 Drift Motions

Drift by a force perpendicular to B

The equation of motion (2.1) can be generalised by replacing the electric field $\mathbf{E}$ with a general external force $\mathbf{F}$

$$m\frac{\mathrm{d}\mathbf{v}}{\mathrm{d}t} = \mathbf{F} + q\,\mathbf{v} \times \mathbf{B}. \tag{2.7}$$

Using the cross product with $\mathbf{B}$ from the right yields

$$\begin{aligned} m\,\dot{\mathbf{v}} \times \mathbf{B} &= \mathbf{F} \times \mathbf{B} + q\,(\mathbf{v} \times \mathbf{B}) \times \mathbf{B} \\ &= \mathbf{F} \times \mathbf{B} - qB^2\,\mathbf{v}_\perp. \end{aligned}$$

Reordering of the equation to $\mathbf{v}_\perp$ gives

$$\mathbf{v}_\perp = \frac{\mathbf{F} \times \mathbf{B}}{qB^2} - \frac{m\,\dot{\mathbf{v}} \times \mathbf{B}}{qB^2}. \tag{2.8}$$

The second term in this equation is equivalent with the time derivative of the gyration. Taking the mean value over the gyration leads to a drift caused by the external force

$$\mathbf{v}_F = \frac{\mathbf{F} \times \mathbf{B}}{qB^2}. \tag{2.9}$$

This means that every force which acts perpendicular to the magnetic field on the particles causes a drift motion. If the force does not depend linearly on q, ions and electrons drift in opposite directions.

Single Particle Drifts

Cause of Force	**Drift velocity**
General Force $\mathbf{F}$	$\mathbf{v}_F = \frac{\mathbf{F} \times \mathbf{B}}{qB^2}$
Electric field $\mathbf{E}$	$\mathbf{v}_E = \frac{\mathbf{E} \times \mathbf{B}}{B^2}$
Gradient of $\mathbf{B}$ field	$\mathbf{v}_{\nabla B} = \pm\frac{1}{2} v_\perp r_L \frac{\mathbf{B} \times \nabla B}{B^2}$
Curvature of $\mathbf{B}$ field	$\mathbf{v}_c = \frac{m v_\parallel^2}{qB^2}\,\boldsymbol{\kappa} \times \mathbf{B}$

Table 2.1: Summary of single particle drifts caused by electric and magnetic forces.

Directly taking the results from the above subsection, the general external force can be replaced by certain forces occurring in a toroidally confined plasma. This is on the one hand the force from the electric field $\mathbf{F} = q\,\mathbf{E}$

and on the other hand forces which are due to the non-uniform magnetic field, namely due to the gradient of the magnetic field ∇B and the curvature of the magnetic field $\boldsymbol{\kappa} = \mathbf{R}_c/R_c^2$ with $\mathbf{R}_c$ constant radius of curvature or more general using $\mathbf{b} = \mathbf{B}/B$ for $\boldsymbol{\kappa} = \mathbf{b} \cdot \nabla \mathbf{b}$, summarised in table 2.1.

Diamagnetic Drift

Additionally to the described drifts caused by a single particle approach, other drifts exist in the context of a fluid picture. Of major interest is one effect which dominates the plasma background

$$v_{dia} = -\frac{\nabla p \times B}{q\, n B^2} \tag{2.10}$$

which is called the *diamagnetic drift*. Because the field lines are roughly aligned in the toroidal direction and the pressure gradient in the radial direction, the diamagnetic drift is poloidal. Although ions and electrons move in opposite directions, the whole plasma background may rotate poloidally giving rise to a diamagnetic current.

Lawson criterion

It was already indicated in the introduction that the rate of Coulomb collisions is some orders of magnitude larger than the rate of collisions which lead to fusion at $T < 30$ keV. As Coulomb collisions generally lead to the diffusion of particles, it is essential to have concepts for the proper confinement of particles on earth. But to reach a adequate amount of fusion, confinement alone is not sufficient. It is imaginable, that a plasma must be sufficiently dense and hot to satisfy the demand for fusion power. This can be formulated with the so-called *Lawson criterion* which states, that a plasma must exceed a critical value of the *tripple product* $nT\tau_E$ to achieve a self-sustaining state, called ignition. In this criterion n is the line averaged density, T the line averaged temperature and τ_E the energy confinement time of the plasma. An approximative power balance [23] then gives

$$nT\tau_E > 3 \cdot 10^{21} \mathrm{m}^{-3}\mathrm{keVs} \tag{2.11}$$

as ignition condition. To achieve the Lawson criterion, refined magnetic configurations are required which will be discussed in the following.

2.1.4 Configurations for Magnetic Confinement

Magnetohydrostatic Equilibria

In a hot fusion plasma in thermal equilibrium the particles reside nearly in a Maxwell-distribution. This means, that the plasma pressure behaves like an ideal gas $p = \sum_\alpha n_\alpha k_B T_\alpha$. The confinement of the plasma in a finite volume leads to a pressure gradient ∇p corresponding to a force. This force must be compensated by the electromagnetic force

$$\nabla p = \mathbf{j} \times \mathbf{B} \tag{2.12}$$

for magnetic confinement. From this equation follows that $\mathbf{B}$ is perpendicular to ∇p and therefore

$$\mathbf{B} \cdot \nabla p = 0. \tag{2.13}$$

Mathematically, there is only one topology fulfilling those criteria - the torus [24]. Therefore torii are of central importance in the area of plasma confinement and fusion research.

In order to describe the particle motion in torii, it is possible to construct an isomorphism with Hamiltonian mechanics. The poloidal magnetic flux $\psi_p(\psi_t, \theta_m, \phi)$ represents a Hamilton function and the canonical momentum is the corresponding toroidal flux ψ_t. The poloidal angle θ_m will then be the canonical coordinate and the toroidal angle ϕ the canonical time. With this Hamilton function and the constraint $\mathbf{B} \cdot \nabla p = 0$, the magnetic field can then be expressed as

$$2\pi \mathbf{B} = \nabla \psi_t \times \nabla \theta_m + \nabla \phi \times \nabla \psi_p \tag{2.14}$$

in its symplectic form[3] [24, 25]. In magnetic coordinates (ψ_t, θ_m, ϕ), ψ_p is a function of ψ_t alone allowing the definition of the *rotational transform*

$$\iota = \frac{1}{2\pi} \frac{\mathrm{d}\psi_p}{\mathrm{d}\psi_t}, \tag{2.15}$$

which represents the twisting of the magnetic field lines and gives the number of poloidal turns per toroidal revolution. In fusion devices ι is choosen to be irrational in order for a particular field line to form a magnetic surface which are enumerated by the toroidal flux ψ_t or the normalised radius $\rho = r/a$ [25].

[3] Here differential geometry of mathematical physics can be used to gain results for abstract Hamilton mechanics.

2.1.5 Conservation of Magnetic Moment

As is known by the *Noether Theorem* from classical mechanics, every symmetry of motion implies a conserved quantity [26].

The connection with gyration is therefore apparent. The action of a particle over one gyration must be constant.

$$\begin{aligned} I &= \oint \mathbf{p}\,\mathrm{d}\mathbf{q} = const. \\ &= \oint (m\mathbf{v} + q\mathbf{A})\,\mathrm{d}\mathbf{q} = 2\pi m v_\perp r_L + q\int_S (\nabla \times \mathbf{A})\,\mathrm{d}\mathbf{S} \\ &= 2\pi\frac{m^2 v_\perp^2}{qB} + q\pi B r_L^2 = 3\pi\frac{m^2 v_\perp^2}{qB} \end{aligned} \tag{2.16}$$

Within the calculated action of the gyration the magnetic moment

$$\mu = \frac{m v_\perp^2}{2B} \cong const., \tag{2.17}$$

appears, which is therefore a conserved quantity of motion.

The gyration is a periodic motion but the particle trajectories don't follow closed paths in an inhomogeneous magnetic field. Therefore the action is a well defined integral but can no longer be seen as a strict invariant. Because the change of the system is small compared to the periodic motion, the change of the conserved quantity is marginal. Such quantities are called *Adiabatic Invariants*.

Poloidal Magnetic Field

The last subsection made clear, that a torus is best suited to magnetically confine a plasma. But the radial magnetic field gradient ∇B of such a toroidal configuration leads to a charge separation (∇B drift) causing a vertical electric field. The resulting $\mathbf{E} \times \mathbf{B}$ drift would therefore push the particles radially out of the torus. To render these radial drift motions innocuous, a poloidal magnetic field component is required. To realise such a poloidal field component additional to a toroidal field, different concepts have been developed. The most advanced concepts are the Tokamak and the Stellarator as explained in the following.

Tokamak One possibility is the induction of a strong current parallel to the toroidal field resulting in a poloidal magnetic field. This idea was developed in the Soviet Union by Tamm and Sakharov in the mid 1960's [23] and is the basis of the so-called *Tokamak*. The drawback of this technique is the central transformer itself, which can only induce the current for a finite time.

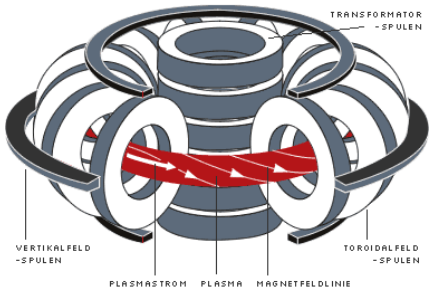

Figure 2.1: Schematic design [27] of a Tokamak with toroidal field coils and plasma current, responsible for the poloidal twist of the field lines.

Stellarator An alternative confinement concept which is independent of plasma current is the *Stellarator* invented by Lyman Spitzer at Princeton in the early 1960's [28]. Here the poloidal field component is created by external coils wound around the plasma torus. The current of the external coils can be controlled from the outside which allows the Stellarator to work in a steady state. To realise such a configuration, the coils must have a complex three dimensional shape. The variety of possible magnetic fields led to different Stellarator concepts, e.g. Heliotron and Optimised Stellarator, figure 2.2.

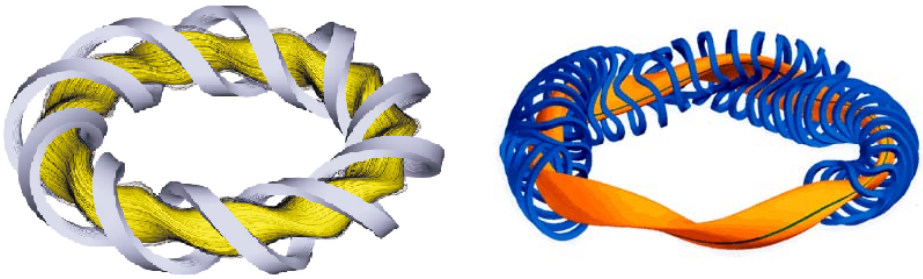

Figure 2.2: Magnetic field configuration and main coils of the Large Helical Device (LHD - Heliotron), Japan (left) and of Wendelstein 7-X (W7-X - Optimised Stellarator), under construction in Germany (right).

2.1.6 Magnetic Mirror

The conservation of the magnetic moment induces a force parallel to the magnetic field lines. This can be illustrated using a simple physical picture. If a particle is moving along a field line and if the magnetic field strength $|\mathbf{B}|$ increases along this line, the adiabatic invariance of the magnetic moment (2.17) leads to an increase of the velocity perpendicular to the magnetic field $v_\perp$. But due to the likewise conservation of the kinetic energy $\frac{1}{2}mv_0^2 = \frac{1}{2}m\left(v_\perp^2 + v_\parallel^2\right)$ of the particle, the velocity parallel to the field $v_\parallel$ must decrease. This means, that a force $\mathbf{F}_\parallel$ acts antiparallel to $\mathbf{B}$. To calculate this force, the kinetic energy and the equation (2.17) must be combined to $v_\parallel^2 = v_0^2 - \frac{2\mu B}{m}$ and taking the total time derivative $\frac{\mathrm{d}}{\mathrm{d}t}$ of this expression yields

$$\frac{\mathrm{d}}{\mathrm{d}t}\left(\mathbf{v}_\parallel \cdot \mathbf{v}_\parallel\right) = 2\,\frac{\mathrm{d}\mathbf{v}_\parallel}{\mathrm{d}t} \cdot \mathbf{v}_\parallel = -2\,\frac{\mathrm{d}}{\mathrm{d}t}\left(\frac{\mu B}{m}\right). \tag{2.18}$$

Because $\mathbf{v}_\parallel$ is the velocity along the field line, it is possible to express it in this case as $\mathbf{v}_\parallel = \frac{\mathrm{d}\mathbf{s}}{\mathrm{d}t}$. Multiplication of the inverse with equation (2.18) yields

$$\mathbf{F}_\parallel = -\mu\frac{\mathrm{d}B}{\mathrm{d}\mathbf{s}} = -\mu\nabla_\parallel B \tag{2.19}$$

for the antiparallel force.

From the expression of the parallel velocity it is evident, that for a parallel velocity small enough, the particle gets slowed down to $v_\parallel = 0$ and then begins to move in the opposite direction. If the strength of the magnetic field increases in this direction too, the particle will again be reflected at some point. The particle is therefore trapped in a region of weak magnetic field. This is generally known as the the *magnetic mirror* effect.

Consider the particle at the point of minimal field B_{min} to have the velocity $v_\perp = v_{\perp min}$ and $v_\parallel = v_{\parallel min}$. Then the particle is just barely trapped, if it has at the point of maximal field B_{max} the velocity $v_\perp = v_0$ and $v_\parallel = 0$. Using the equation of the kinetic energy $v_0^2 = v_{\perp min}^2 + v_{\parallel min}^2$ and the equation of the magnetic moment $\frac{m}{2}\frac{v_{\perp min}^2}{B_{min}} = \frac{m}{2}\frac{v_\perp^2}{B_{max}}$ it follows that

$$\frac{B_{min}}{B_{max}} = \frac{v_{\perp min}^2}{v_\perp^2} = \frac{v_{\perp min}^2}{v_0^2} = \sin^2 p_{min} \tag{2.20}$$

with the so-called *pitch-angle* p. This means, all particles with a pitch-angle

$p \geq p_{min} = \arcsin \frac{B_{min}}{B_{max}}$ are trapped in the region of weak magnetic field.

The principle of the magnetic mirror is important for the understanding of particle motion in magnetic configurations of fusion plasmas, particularly in toroidal devices. Those fields have regions of weak and strong magnetic field. If particles get locally trapped in such a configuration, collisions can lead to radial transport of the particle with large step widths. These losses can sum up to a major transport loss of the plasma.

2.1.7 Trapped Particle Orbits

The curved magnetic field of a toroidal device decreases radially as $B \propto 1/R$ with the major radius R, because the distance between two coils is larger on the outboard side of the torus. Due to the additional poloidal magnetic field, the field lines are wound around the torus. Therefore a field line will pass through regions of low magnetic field on the outboard side and high magnetic field on the more inboard side. In a Tokamak this field variation can easily be described by a cosine as schematically illustrated in figure 2.3.

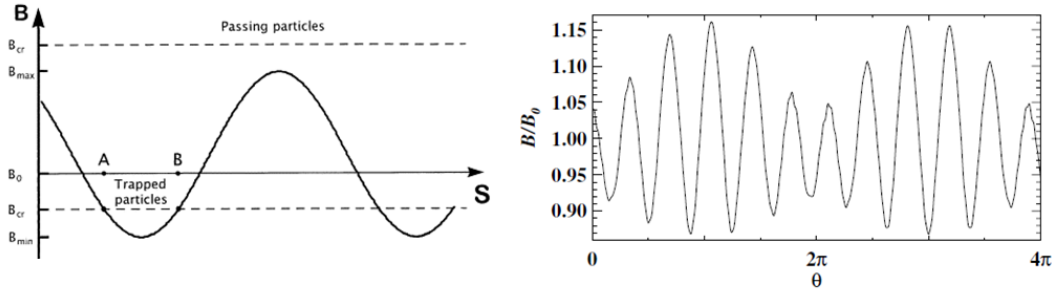

Figure 2.3: Schematic view of the magnetic field variation along a field line **S** in a Tokamak (left) and for the high mirror configuration of W7-X (right). Figures appear courtesy of B. Wolle [29] and C. Beidler [30].

As a result, particles with velocity vectors nearly perpendicular to the magnetic field are trapped in the weak magnetic field on the outside of the torus following the concept of the magnetic mirror as described in the last subsection. The orbits of such trapped particles are much larger than the gyroradius indicating a large random-walk step size for these particles [31].

To demonstrate this behaviour, the diffusion for the so-called *banana* orbits of Tokamaks shall be briefly calculated here. To determine the diffusion caused by the trapped particles with the random-walk method, the fraction of trapped

particles J, the step width $(\Delta r)^2$ and the effective collision frequency ν_{eff} is necessary $D \propto J\,(\Delta r)^2\,\nu_{eff}$. The fraction of trapped particles can be calculated from the general mirror principle of the last subsection with

$$J \propto \frac{v_\parallel}{v_\perp} = \sqrt{\frac{B_{max}}{B_{min}} - 1}. \tag{2.21}$$

The magnetic field of a Tokamak can in general be approximated by $B/B_0 = 1 - \epsilon_t \cos(\theta)$ which yields for the maximum and minimum field strength

$$\frac{B_{max}}{B_{min}} = \frac{1+\epsilon_t}{1-\epsilon_t} \approx 1 + 2\,\epsilon_t. \tag{2.22}$$

Inserting in the above equation gives the number of trapped particles $J \propto \sqrt{\epsilon_t}$. In contrast to classical diffusion are already small-angle scatterings sufficient to bring a trapped particle from one banana orbit to another. As the trapped particles occupy in phase space only a small region of angles $\Delta\xi \leq \sqrt{\epsilon_t}$, it is clear that the effective collision frequency for scattering by $\Delta\xi$ is

$$\nu_{eff} \sim \frac{\nu}{(\Delta\xi)^2} \sim \frac{\nu}{\epsilon_t}. \tag{2.23}$$

The width of the orbit is defined by $\Delta r = \dot{r}/\dot{\theta}$ with $\dot{r}$ governed by the drift velocity $\dot{r} \propto v_d$ and $\dot{\theta}$ following a simple geometric circular sector $\dot{\theta} = \iota\, v_\parallel / R_0$. Combining all arguments and considering that here the collisions of equal mass are important, the so-called neoclassic banana diffusion [32] yields

$$D_b \propto \sqrt{\epsilon_t} \left(\frac{v_d\, R_0}{\iota\, v_\parallel} \right)^2 \frac{\nu}{\epsilon_t} = \frac{1}{\iota^2\, \epsilon_t^{3/2}} \frac{r_L^2}{\tau_{ii}} \tag{2.24}$$

with τ_{ii} being the time between two ion-ion collisions. Comparing classic diffusion (2.6) and neoclassic banana diffusion results in

$$\frac{D_b}{D_{cl}} = \frac{1}{\iota^2\, \epsilon_t^{3/2}} \sqrt{\frac{m_i}{m_e}} \sim 200 \tag{2.25}$$

for standard Tokamak values. Due to the three dimensional shape of Stellarators, trapped particle orbits are more difficult to calculate, but have an even greater importance. The shown example emphasises the impact of trapped particles on diffusion and plasma transport. How this neoclassical transport can be calculated from first principles will be the topic of the next section.

2.2 General Transport Theory

The main goal of transport theory in general refers to the calculation of particle and heat fluxes $\mathbf{\Gamma}$ and $\mathbf{q}$. As known from *Fick's Law* and *Fourier's Law of thermal conduction* such fluxes are normally related to thermodynamic forces and their gradients ∇n and ∇T such, that

$$\begin{aligned} \mathbf{\Gamma} &= -D\,\nabla n \\ \mathbf{q} &= -\chi\,\nabla T \end{aligned}$$

with the diffusion coefficient D and the heat conductivity χ [31]. Both convection and heat conduction are caused by the collective interaction of particles on microscopic scale. As fusion plasmas consist of non-equilibrium thermodynamics, a description is necessary which is based on local effects. Useful is therefore *Boltzmann's H-Theorem*[4] stating that every point of a gas strives for a *Maxwell-Boltzmann-Distribution* leading to a random walk of the particles through collisions, in general called collisional transport. This and the kinetic theory of magnetic confinement will be discussed in the following.

2.2.1 Transport Matrix

To describe and relate fluxes and diffusion, a transport matrix is often employed which makes use of the concept of *local thermodynamic equilibrium*. This means, that the system must be spatially and temporally divided in cells of infinitesimal size, in which classical thermodynamic equilibrium conditions are fulfilled in adequate approximation. Especially in the case of gas mixtures such a state is present including both mass and heat transfer. Following the very general concept of the *Onsager reciprocal relations*, a flux I_i must be caused by the action of all thermodynamic forces A_j. This can be written in the form of

$$I_i = c \sum_j L_{ij}\, A_j \tag{2.26}$$

with a factor c and the kinetic transport coefficients L_{ij} [33].

[4] Often also called *Eta-Theorem*.

In the case of a plasma, where the electric field $\mathbf{E}_r$ must be considered, the *transport matrix* [34] takes the form

$$\begin{bmatrix} \frac{\Gamma_\alpha}{n_\alpha} \\ \frac{Q_\alpha}{n_\alpha T_\alpha} \end{bmatrix} = - \begin{bmatrix} L_{11}^\alpha & L_{12}^\alpha \\ L_{21}^\alpha & L_{22}^\alpha \end{bmatrix} \cdot \begin{bmatrix} \frac{\nabla n_\alpha}{n_\alpha} - \frac{Z_\alpha E_r}{T_\alpha} - \frac{3}{2}\frac{\nabla T_\alpha}{T_\alpha} \\ \frac{\nabla T_\alpha}{T_\alpha} \end{bmatrix} \tag{2.27}$$

with the index α denoting the particle species and the particle flux as

$$\mathbf{\Gamma} = n\,\mathbf{u} = \int \mathbf{v}\, f\, \mathrm{d}^3\mathbf{v}. \tag{2.28}$$

To effectively use these equations, the thermal diffusion coefficients L_{ij}^α must be determined. How the diffusion coefficients may be calculated will be shown conceptually in the next section.

It must be noticed here, that it is essential to make a difference between the heat flux $\mathbf{q}$ and the energy flux $\mathbf{Q}$

$$\mathbf{q} = \int \frac{m}{2} (\mathbf{v} - \mathbf{u})^2 (\mathbf{v} - \mathbf{u})\; f\, \mathrm{d}^3\mathbf{v} \tag{2.29}$$

$$\mathbf{Q} = \int \frac{mv^2}{2} \mathbf{v}\, f\, \mathrm{d}^3\mathbf{v} \tag{2.30}$$

which are identified to be different velocity-space moments of the distribution function [35, 36].

2.2.2 Ambipolarity Constraint

Due to the high mass of the ions and the resulting larger Larmor-radius, ions diffuse much faster out of the plasma than electrons. But as the ions leave the electrons behind, a strong electric field develops, somewhat accelerating the electrons and thus slowing down the ions. The field to maintain the ambipolarity is called *ambipolar electric field* and the adjustment of the radial flow velocity is called *Ambipolar Diffusion* and leads to a balance of particle fluxes for both the ions and electrons. This fact can be expressed in the *Ambipolarity Constraint*

$$\Gamma_e = \sum_i Z_i\, \Gamma_i \tag{2.31}$$

with the charge number Z_i of the ions.

In addition, the ambipolar electric field leads to a poloidal drift motion of the particles (cf. $\mathbf{E} \times \mathbf{B}$-drift in subsection 2.1.3). This drift may delocalise particles trapped in the magnetic wells and is therefore capable of reducing diffusion [37]. Such a field is therefore desirable, but it cannot be freely chosen or adjusted because it is an intrinsic property of the plasma.

2.3 Kinetic Theory of Neoclassical Transport

If an ideal gas resides in thermal equilibrium, the velocity distribution of the particles is described by the Maxwell-Boltzmann-distribution. This is based on the statistical velocity distribution of the particles. In the case of the Maxwell-Boltzmann-distribution the absolute value of the velocity is represented by a normal distribution.

The Vlasov-Equation

Due to the strong density and temperature gradients in a fusion plasma every point in the plasma has different and therefore local velocity distribution. Coulomb collisions may lead to temporal change of the distribution. In the case of a fusion plasma, the distribution function

$$f = f(\mathbf{r}, \mathbf{v}, t) \tag{2.32}$$

has seven independent variables. With $f(\mathbf{r}, \mathbf{v}, t)$ the density in position space

$$n(\mathbf{r}, t) = \int f(\mathbf{r}, \mathbf{v}, t)\, \mathrm{d}^3 v \tag{2.33}$$

can be calculated. Taking the total time derivative of the velocity distribution, the partial derivative of all variables must be taken to get the *Boltzmann equation*

$$\frac{\mathrm{d}f}{\mathrm{d}t} = \frac{\partial f}{\partial t} + \mathbf{v} \cdot \nabla f + \frac{\mathbf{F}}{m} \cdot \frac{\partial f}{\partial \mathbf{v}}. \tag{2.34}$$

If the plasma is sufficiently hot, collisions can be neglected, meaning $\frac{\mathrm{d}f}{\mathrm{d}t} = 0$. Taking only electromagnetic forces into account, equation (2.34) takes the form

$$\frac{\partial f}{\partial t} + \mathbf{v} \cdot \nabla f + \frac{q}{m} (\mathbf{E} + \mathbf{v} \times \mathbf{B}) \cdot \frac{\partial f}{\partial \mathbf{v}} = 0. \tag{2.35}$$

This special formulation is called the *Vlasov-Equation* [20], often used for simulations of hot plasmas for which collision times are long compared to the development of f.

The Focker-Planck-Operator

Collisions in a plasma lead to a change of the distribution function f. If collisions are considered, the assumption $\frac{\mathrm{d}f}{\mathrm{d}t} = 0$ is no longer valid. Then collisions provide a non-vanishing contribution

$$\frac{\mathrm{d}f}{\mathrm{d}t} = C(f) \tag{2.36}$$

where $C(f)$ is called the *Collision operator*. Because the Coulomb interaction is a far reaching force, every collision leads only to a small change of the velocity $\Delta\mathbf{v}$ of a particle. The distribution function $f(\mathbf{r}, \mathbf{v}, t)$ can therefore be expanded in powers of $\Delta\mathbf{v}$. If terms up to the second order are considered, the collision operator takes the form

$$-\frac{\partial}{\partial \mathbf{v}} \cdot \left(\frac{\mathrm{d}\langle \Delta\mathbf{v} \rangle}{\mathrm{d}t} f \right) + \frac{1}{2} \frac{\partial^2}{\partial \mathbf{v} \partial \mathbf{v}} : \left(\frac{\mathrm{d}\langle \Delta\mathbf{v}\Delta\mathbf{v} \rangle}{\mathrm{d}t} f \right) = C(f) \tag{2.37}$$

which is known as the *Focker-Planck-Operator*[5] [21].

In this notation $\frac{\mathrm{d}\langle \Delta\mathbf{v} \rangle}{\mathrm{d}t}$ describes the mean change of velocity of a particle by Coulomb collisions. Those collisions in general slow down the particles, which is why $\frac{\mathrm{d}\langle \Delta\mathbf{v} \rangle}{\mathrm{d}t}$ is also called the *dynamic friction*. The *velocity diffusion* $\frac{\mathrm{d}\langle \Delta\mathbf{v}\Delta\mathbf{v} \rangle}{\mathrm{d}t}$ accelerating the distribution of the velocity acts against this friction leading on average to an energy gain of cold particles, but energy loss for hot particles [21].

2.3.1 The Drift Kinetic Equation

The equations discussed in the last subsections are still too general to calculate diffusion coefficients. Therefore the Boltzmann equation (2.34) must be approximated regarding small Larmor radius and large gyrofrequency. This can be done using perturbation theory [38] or recursion methods [39].

[5] With $\frac{\partial^2}{\partial \mathbf{v} \partial \mathbf{v}} : \frac{\mathrm{d}\langle \Delta\mathbf{v}\Delta\mathbf{v} \rangle}{\mathrm{d}t}$ is here the double scalar product meant between the two dyad's $\frac{\partial^2}{\partial \mathbf{v} \partial \mathbf{v}}$ und $\frac{\mathrm{d}\langle \Delta\mathbf{v}\Delta\mathbf{v} \rangle}{\mathrm{d}t}$ which can be expressed in the index notation $\sum \frac{\partial^2}{\partial v_i \partial v_j} \frac{\mathrm{d}\langle \Delta v_i \Delta v_j \rangle}{\mathrm{d}t}$

Averaging the Boltzmann equation (2.34) over one gyration

$$\langle G \rangle = \frac{1}{2\pi} \int G \, \mathrm{d}\phi \tag{2.38}$$

yields the mean-value of the distribution function $\langle f \rangle = \overline{f}$. Then the velocity of the gyration centre can be seen as two components, a component parallel to the magnetic field $\mathbf{v}_\parallel$ and a component incorporating the drift motions $\mathbf{v}_D$

$$\mathbf{v}_{gc} = \mathbf{v}_\parallel + \mathbf{v}_D \tag{2.39}$$

where the drift velocity is described by

$$\mathbf{v}_D = \frac{\mathbf{E} \times \mathbf{B}}{B^2} + \frac{\mu}{q} \frac{\mathbf{B} \times \nabla B}{B} + \frac{v_\parallel^2}{\omega_c} \frac{\mathbf{B} \times \boldsymbol{\kappa}}{B} \tag{2.40}$$

which is a combination of the effects of section 2.1.

Using the energy of the gyration centre

$$U = \frac{m v_\parallel^2}{2} + e\Phi + \mu B \tag{2.41}$$

and the magnetic moment μ, the derivative with respect to the velocity

$$\frac{\mathrm{d}\mathbf{v}}{\mathrm{d}t} \cdot \frac{\partial f}{\partial \mathbf{v}} = \frac{\mathrm{d}U}{\mathrm{d}t} \frac{\partial f}{\partial U} + \frac{\mathrm{d}\mu}{\mathrm{d}t} \frac{\partial f}{\partial \mu} \tag{2.42}$$

can be reformulated.

Due to the conservation of the mangetic moment, the derivative with respect to μ is negligible. Taking the results together with $\mathbf{E}_A = -\frac{\partial \mathbf{A}}{\partial t}$ yields

$$\frac{\partial \overline{f}}{\partial t} + \left(\mathbf{v}_\parallel + \mathbf{v}_D\right) \cdot \nabla \overline{f} + q \, \mathbf{v}_\parallel \cdot \mathbf{E}_A \frac{\partial \overline{f}}{\partial U} = \overline{C}\left(\overline{f}\right) \tag{2.43}$$

as *drift kinetic Equation* of first order $\mathcal{O}(\delta)$ [40].

The drift kinetic equation can, if desired, be generalised to higher orders of $\delta = \frac{\rho}{L}$, where ρ is the thermal gyroradius and L the scale length characterising the plasma. The equation builds the basis for the calculation of diffusion coefficients, which will be explained in the next subsection.

2.3.2 Calculation of Diffusion Coefficients

To obtain the diffusion coefficients for a certain magnetic field configuration, generally speaking, the drift kinetic equation (2.43) must be solved. This is an extremely extensive problem and therefore only a small insight shall be given here following the concept used in [30].

In the usual approach, small deviations f_1 from an equilibrium distribution f_0 are considered allowing to express f with an expansion factor c as

$$f = c \cdot f_0 + f_1 \tag{2.44}$$

where the equilibrium distribution function in general can be chosen as Maxwell distribution

$$f_0 = f_M = n \left(\frac{m}{2\pi T} \right)^{\frac{3}{2}} e^{-K}. \tag{2.45}$$

with $K = mv^2/2T$. As was already stated in subsection 2.2.1, a transport matrix can be formulated which relates the flux-surface-averaged flows I_i to the driving thermodynamic forces A_j

$$I_i = -n \sum_j L_{ij} A_j. \tag{2.46}$$

Having a solution for f_1 the flux-surface-averaged flows can be defined connecting I_1 with the radial component of the particle flux density $\mathbf{\Gamma}$ and I_2 with the radial component of the energy flux density $\mathbf{Q}$ through

$$I_1 = \langle \mathbf{\Gamma} \cdot \nabla r \rangle = \left\langle \int \frac{\mathrm{d}r}{\mathrm{d}t} f_1 \, \mathrm{d}^3 v \right\rangle \tag{2.47}$$

$$I_2 = \left\langle \frac{\mathbf{Q}}{T} \cdot \nabla r \right\rangle = \left\langle \int K \frac{\mathrm{d}r}{\mathrm{d}t} f_1 \, \mathrm{d}^3 v \right\rangle \tag{2.48}$$

with the thermodynamic forces

$$\begin{aligned} A_1 &= \frac{1}{n}\frac{\mathrm{d}n}{\mathrm{d}r} - \frac{q\,E_r}{T} - \frac{3}{2}\frac{1}{T}\frac{\mathrm{d}T}{\mathrm{d}r} \\ A_2 &= \frac{1}{T}\frac{\mathrm{d}T}{\mathrm{d}r}. \end{aligned}$$

This means that the perturbation f_1 of the distribution function is the main driver of the plasma transport. Inserting the perturbation ansatz $f = c \cdot f_0 + f_1$ with magnetic flux coordinates [24] into the drift kinetic equation

(2.43), a linearised and radially local drift equation can be obtained [41]. This equation is lacking derivatives of f_1 with respect to r and v reducing the drift kinetic equation to three phase space variables. Neglecting additionally parallel transport, it is possible to write the first order distribution function in the form [30]

$$f_1 = \frac{v_d\, R_0}{\nu}\,(A_1 + K\, A_2)\; f_M\, \widehat{f_{\mathrm{II}}} \tag{2.49}$$

with the drift velocity $v_d = mv^2/2qB_0R$. Inserting this equation in the flux-surface-averaged flows I_i and comparing with the transport matrix yields the thermal diffusion coefficients (2.27) discussed in section 2.2.1

$$L_{ij} = \frac{2}{\sqrt{\pi}} \int_0^\infty \sqrt{K}\, e^{-K}\, D_\perp(K)\, h_i\, h_j\; \mathrm{d}K \tag{2.50}$$

with $h_1 = 1$, $h_2 = K$ and $D_\perp$ being the *radial monoenergetic diffusion coefficient*

$$D_\perp = -\frac{v_d^2 R_0}{2\,\nu} \left\langle \int_{-1}^{1} \frac{1}{v_d} \frac{\mathrm{d}r}{\mathrm{d}t}\, \widehat{f_{\mathrm{II}}}\, \mathrm{d}p \right\rangle \tag{2.51}$$

which can be calculated using the solution of the simplified drift kinetic equation for $\widehat{f_{\mathrm{II}}}$, the pitch angle $p = v_\parallel/v$ as integration variable and averaging over the flux surface indicated by the brackets.

As already stated solving the drift kinetic equation and obtaining monoenergetic diffusion coefficients is a non-trivial task requiring optimised codes and large vector computers. Nonetheless is the effort worthwhile as this procedure possesses several advantages. E.g. the monoenergetic diffusion coefficients are only dependent on the flux label ψ and two dimensionless quantities, namely collisionality $\nu^* = \nu\, R_0/v\, \iota$ and normalised $\mathbf{E} \times \mathbf{B}$ drift velocity $v_E^* = E_r/v\, B_0$, it is sufficient to create a database for which the dimensionless quantities are varied over the physically relevant range of values. By interpolating these results it is possible to completely describe any plasma of a certain magnetic field configuration, which may then be directly used in the 1-D simulations explained later in chapter 3.

2.3.3 Transport Regimes in a Stellarator

Calculations for the monoenergetic diffusion coefficients were done by different groups worldwide and compared [30], see figure 2.4.

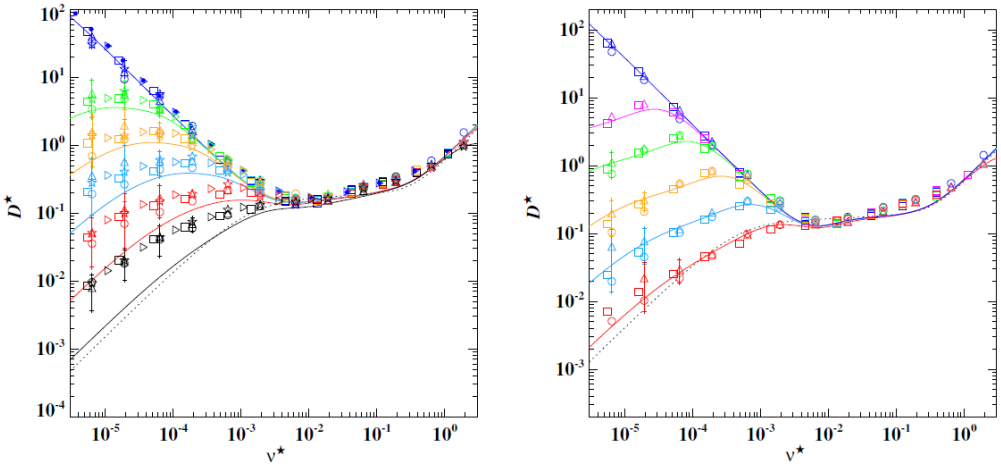

Figure 2.4: Normalised radial monoenergetic diffusion coefficient as function of collisionality for increasing electric field from dark blue to black for W7-X standard configuration at $\rho = 0.5$ (left) and $\rho = 0.25$ (right) where $\rho = \sqrt{\psi_t/\psi_{max}} = r/a$ with the minor plasma radius a, different symbols represent different codes with the dashed line being the Tokamak-reference. Figures appear courtesy of C.D. Beidler [30].

As the above figure indicates, different regimes can be identified. Again, the whole physical explanation of these regimes would be out of proportion for this work and only the basic features shall be named in the following.

The dominant regime for the electrons is in general the $1/\nu$-*regime* represented by the dark blue line in figure 2.4 where the diffusion is very high due to the very low collisionality. The dominant regime for the ions is often the $\sqrt{\nu}$-*regime* represented by the other colored lines at low collisionalities which strongly depends on the radial electric field. For moderate collisionalities all the lines come together and build a *plateau-regime* with a constant diffusion coefficient independent of electric field.

The drift kinetic equation can be approximated for those extreme cases and analytical expressions found [42]. Those are normally expressed in terms of the drift velocity $v_d = mv^2/2qB_0R$ and collision frequency $\nu = \nu^\alpha = \sum_\beta \nu^{\alpha/\beta}$, where the collision frequency of species α is given by the sum of all collision

frequencies with each of the background plasma species β

$$\nu^{\alpha/\beta} = \nu_0^{\alpha/\beta} \left\{ \mathrm{erf}(\sqrt{K^{\alpha/\beta}}) \left(1 - \frac{1}{2K^{\alpha/\beta}}\right) + (\pi K^{\alpha/\beta})^{-1/2} \exp(-K^{\alpha/\beta}) \right\}$$

with the reference collision frequency

$$\nu_0^{\alpha/\beta} = \frac{n^\beta (q^\alpha\, q^\beta)^2 (\ln\Lambda)^{\alpha/\beta}}{4\pi(\epsilon_0 m^\alpha)^2 v^3}$$

and $K^{\alpha/\beta} = (m^\beta/m^\alpha)(T^\alpha/T^\beta)K$, $K = mv^2/2T$ as well as the Coulomb logarithm $\ln\Lambda$. Parameters related to the structure of the magnetic field are the inverse aspect ratio $\epsilon_t = r/R$, the poloidal and helical modulation of $\mathbf{B}$, respectively ϵ and ϵ_h as well as the $\mathbf{E}\times\mathbf{B}$ precessional frequency $\Omega_E = E_r/rB_0$ and $\kappa = (\epsilon_t/\epsilon)^2$, characterising the analytical diffusion coefficients.

$$\begin{aligned} D_{1/\nu} &= \frac{4}{9\pi}\, v_d^2\, \frac{(2\,\epsilon_{eff})^{3/2}}{\nu} \\ D_{\sqrt{\nu}} &= \frac{4\sqrt{2}}{9\pi}\, v_d^2\, \frac{\sqrt{\nu}}{|\Omega_E|^{3/2}}\, \frac{1}{\kappa} \\ D_{pl} &= \frac{\pi}{4} \frac{v_d^2\, R_0}{v\,\iota}\, \frac{1}{\kappa} \end{aligned} \tag{2.52}$$

Strictly speaking, the coefficient for the $\sqrt{\nu}$ regime is only valid for a classical Stellarator but as the form is very similar, this approximation is sufficient.

As the particle fluxes of the electrons and ions are not intrinsically ambipolar, the constraint $\Gamma_e = \sum_i Z_i \Gamma_i$ causes a radial electric field to appear, bringing the particle fluxes to the same level. The arising electric field has also impact on the diffusion coefficients $D_{ij}(E_r)$. As both the particle fluxes and the diffusion coefficients are dependent on the electric field, the solution for E_r is highly non-linear. If the ambipolar condition is solved algebraical as implicit equation of the electric field, more than one solution may arise. This is demonstrated in figure 2.5 where the particle fluxes are shown as function of E_r. The circles in the figure indicate the point where the electron and ion flux are the same, corresponding to the solution of the electric field. On the left side of the figure, both electrons and ions have the same temperature which generally leads to only one solution with negative electric field. This is the normal case for fusion plasmas and is called the *ion root*. In a collisionless plasma it can also happen, that the electrons are heated strongly leading to a

high electron temperature and particle flux. In this case can again only one solution be found, namely the so-called *electron root* with a strong positive electric field. Between those two extreme cases, multiple solutions exist where a transition between the different roots is possible as seen in the middle of figure 2.5.

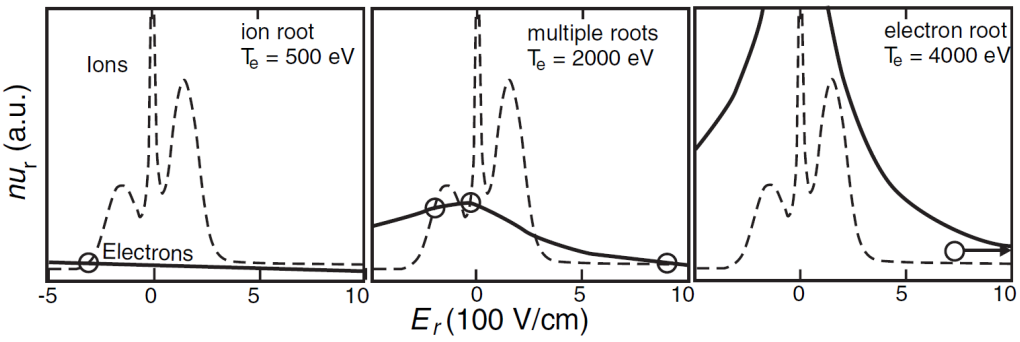

Figure 2.5: Neoclassical electron and ion particle fluxes in the Stellarator W7-AS for different electron temperatures at fixed ion temperature of $T_i = 0.5$ keV calculated at $r = 13$ cm with the DKES code. The circles mark possible solutions for the ambipolar electric field. Figures appear courtesy of U. Stroth [43].

2.4 Anomalous Transport

The neoclassical transport described so far is in good accordance with experimental results, e.g. W7-AS [44]. But this is only true for the plasma core region. At the plasma edge diffusion coefficients are measured which are significantly larger than predicted by neoclassical transport. This additional transport is therefore called *anomalous transport*. Especially in Tokamaks this kind of transport has a leading role. A lot of aspects concerning anomalous transport are not yet clear but it is believed that the general underlying mechanism is *turbulence* [43]. Due to the complexity of this issue, only some conceptional topics will be presented in the following.

2.4.1 Turbulence and Instabilities

Fluctuation measurements at existing experiments gave evidence that turbulence is caused by micro instabilities inside the plasma [45]. There exist many

different types of instabilities contributing to the turbulence. E.g. instability driven by the *ion-temperature gradient* (ITG) or by the *electron-temperature gradient* (ETG) as well as instabilities which are caused by *trapped electrons* (TEM). But all this instabilities can be understood with the general concept of drift waves explained in the following.

Drift Waves

Drift waves are of electrostatic nature meaning that magnetic fluctuations can be neglected for this picture. Essential for the occurrence of a drift wave is a perturbation $\widetilde{n}$ of the density n. Due to the high mobility, electrons respond directly to the density perturbation which creates a positive charge in the region of the positive density perturbation and vice versa leading to an electrostatic potential perturbation $\widetilde{\phi}$ in poloidal direction [43]; see figure 2.6. As the plasma must fulfill the Boltzmann distribution, the density perturbation $\widetilde{n}$ and electrostatic potential perturbation $\widetilde{\phi}$ can be related to

$$\frac{\widetilde{n}}{n} = \frac{e\widetilde{\phi}}{T}. \tag{2.53}$$

The resulting perturbed electric field $\widetilde{\mathbf{E}}$ is directed from the region of increased density to the region of decreased density. If $\widetilde{\mathbf{E}}$ has a part perpendicular to $\mathbf{B}$, the associated $\widetilde{\mathbf{E}} \times \mathbf{B}$ drift will cause a radial density advection. If the density and electric field perturbation are in phase, the net plasma transport is zero and the wave propagates through the plasma. If the perturbations are out of phase the particles are transported to the positive density perturbation essentially amplifying the wave.

Ion-Temperature Gradient Instability

In the case of an ITG instability the drive does not come from the density perturbation alone. The regions of higher density can then be identified with hotter ions and the regions of lower density with colder ions. The hotter fluid drifts faster than the colder one leading to the same charge separation as in the general drift wave picture.

If the amplifying of the mode is maintained a radial elongated vortex may arise which is known as a *streamer*. Due to the large gyroradius of the ions the plasma may develop a kind of self-organisation, the so called *zonal flow*.

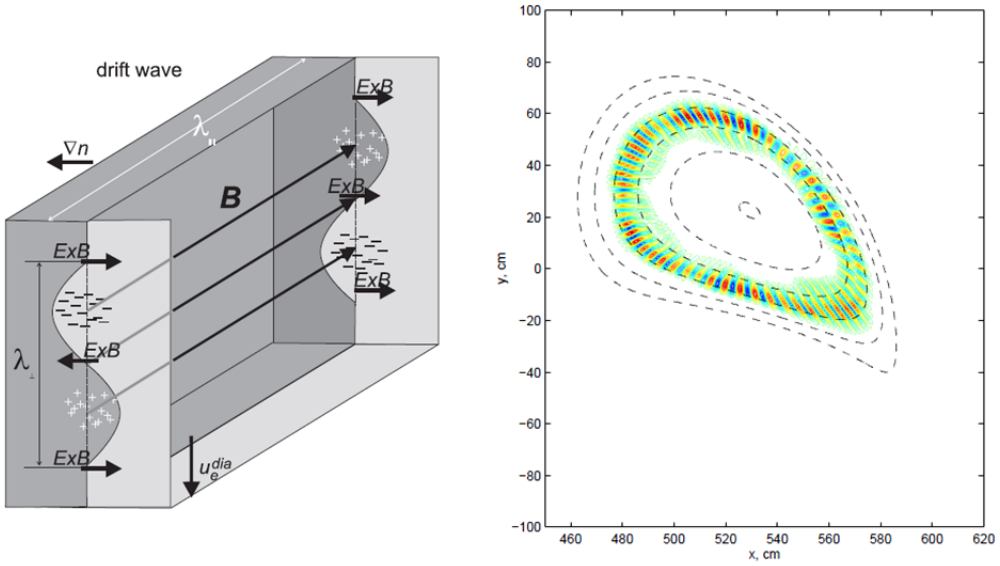

Figure 2.6: Conceptual properties of a linear drift wave (left) and gyrokinetic simulation of an ITG mode in W7-X with $\beta = 4$ % showing level contours of electric potential Φ (right). Figures appear courtesy of U. Stroth [43] and V. Kornilov [46].

This term, borrowed from geophysics, describes a poloidal particle flux which is able to suppress the elongated vortices. From a macroscopic point of view it is plausible that such a mode cannot develop for flat temperature profiles. But if the temperature gradient exceeds a critical value, the instabilities can tap the free energy of the temperature gradient causing modes to grow. This is especially seen in Tokamaks where the anomalous transport increases when a critical temperature gradient is overcome leading to a resilient temperature profile with a constant gradient. This behaviour was not yet seen in Stellarators but is investigated with gyrokinetic simulations.

Electron-Temperature Gradient Instability

Analogue to the ITG instability the role of electrons and ions can be exchanged resulting in the conceptionally equivalent ETG phenomenon. The impact of ETG turbulence on plasma transport is still under investigation. What can be said is that ETG produces only small scale fluctuations on the scale of electron gyro radius which is assumed to yield only a low level of transport [43].

Trapped-Electron-Mode

As already mentioned, particles may be trapped in magnetic wells. If an initial density perturbation is along the trapped particle orbits, the magnetic curvature drift will lead to a charge separation as this drift is in opposite directions for electrons and ions. The resulting perturbation of the electrostatic potential then causes an $\mathbf{E} \times \mathbf{B}$ flow which again enhances the amplitude of the wave.

2.4.2 Kinetic Theory of Anomalous Transport

As stated the anomalous transport is based on micro instabilities and perturbations of electric and magnetic field inside the plasma. To arrive at a kinetic description of the perturbated plasma, the kinetic equation (2.35) must be studied with respect to fluctuations. Therefore relevant quantities are divided into an unperturbed and perturbed part.

$$G = G_0 + G_1 \tag{2.54}$$

In contrast to the drift kinetic equation (2.43), here a very slow temporal evolution of G_0 is assumed. Particularly

$$\frac{\partial G_0}{\partial t} = 0 \tag{2.55}$$

can be assumed, because the instability is of major interest which develops on a much faster time scale. From the conceptual picture it is clear that every perturbation develops a wave and for that reason the temporal derivative can be written as

$$\frac{\partial G_1}{\partial t} \approx -i\omega G_1. \tag{2.56}$$

Beyond that, linearised mean values must be determined for all relevant quantities and inserted into the kinetic equation (2.35) to obtain a *gyrokinetic equation* which can for example be found within the work of R. D. Hazeltine [38]. As in the neoclassical theory, gyrokinetic equations can be solved using high amounts of computer power and extensive codes. At the moment this issue is the major topic in Tokamak theory and the research for this area has also been initiated in the Stellarator community [47].

Chapter 3

0-D Model

Within the roadmap to fusion power plants, demonstrating the feasibility of magnetic confined fusion for electricity production is a cornerstone. A facility fulfilling this requirement is called *DEMO*. In reference [3], the minimum size of such a DEMO reactor of the Tokamak type has been assessed. As in this work Stellarators shall be addressed, the proposed zero dimensional (0-D) methods for Tokamaks of [3] was adapted for the use of Stellarators, which will be explained in this chapter.

3.1 Similarity and Scaling laws

Similarity Principle

To link the physical behaviour of model experiments to application oriented processes the concept of similarity might apply. Comparisons of small scale experiments and large scale processes can be made using the theory of similitude commonly known from windtunnel experiments in fluid mechanics. To ensure physical similarity of a process in a model experiment and the original, a set of dimensionless quantities describing the physical processes, must have comparable values for both cases. To find such a set of dimensionless quantities, different methods can be employed, namely the *Buckingham* Π-*Theorem* (dimensional analysis) [48] and the *scale invariance* method [49, 50]. For toroidal plasmas B. Kadomtsev [51] derived three dimensionless plasma physics parameters which are commonly used. These parameters are the ratio of plasma pressure to magnetic field pressure β, the relative gyroradius ρ^* and the collision frequency normalised to its bounce frequency, known as

collisionality ν^*, defined as follows:

$$\beta = 2\mu_0 \frac{p}{B_t}, \qquad \rho^* = \frac{v_i\, m_i}{e\, B\, a}, \qquad \nu^* = \frac{R_0\, \nu}{v\, \iota}. \tag{3.1}$$

Here a is the minor plasma radius, R_0 the major radius of the device and v the thermal velocity of the particles. Although this set is not unique, the defined quantities are usually employed in the context of upscaling devices with similar geometry. Therefore, the evolution of these quantities in upscaling simulations will also be used at the end of this chapter and throughout the next chapter.

Confinement time

One of the most important aspects of a fusion device is the confinement of particles and energy. To effectively describe these requirements, *confinement times* are used which serve as figures of merit. The confinement time has a direct connection with the *Lawson criterion* for a burning plasma, which states, that if $nT\tau_E$ exceeds a critical value the plasma is self-sustained. The energy confinement time τ_E refers per definition to a plasma with the internal energy W and the heating power P required to sustain the plasma. With these quantities the energy confinement time can be written as

$$\tau_E = \frac{W}{P - \dot{W}}\,. \tag{3.2}$$

Due to the complexity and the multitude of different geometries of fusion devices it is up to now not possible to find a scaling for the confinement time from first principles. Nonetheless two approaches can be followed to find scaling laws. The first method is the regression on the basis at experimental results to obtain empirical scaling laws which will be used in this chapter. The second method is a theory based approach which will be discussed in more detail in the course of the next chapter. Here the most recent Stellarator scaling ISS04 [52]

$$\tau_E^{\mathrm{ISS04}} = 0.465\, a^{2.28} R^{0.64} P^{-0.61} \bar{n}_e^{0.54} B_t^{0.84} \iota_{2/3}^{0.41} \tag{3.3}$$

is used with the minor radius a, major radius R, heating power P, line-averaged density $\bar{n}_e$ in 10^{20} m^{-3}, the magnetic field strength B_t on axis and the rotational transform $\iota = \iota/2\pi$ at 2/3 of the minor radius. This scaling is the basis of the 0-D model because it combines all physic mechanisms in a simple power law and

can therefore be easily used for all following approximations. As the size of a reactor is an important parameter, the major radius R_0 is kept as dimensional variable in the following approximations while the rest of the plasma physics parameters are expressed as dimensionless variables. From a technological point of view B is also kept as dimensional variable to demonstrate directly the influence of advances in technology on plasma performance.

Fusion power

For toroidal geometry, the fusion power can be calculated as

$$P_{fus} = E\,(2\pi a)^2\,R_0 \int_0^1 \rho\, n_D\, n_T\, \langle\sigma v\rangle\, \mathrm{d}\rho \tag{3.4}$$

with the normalised minor radius $\rho = r/a$ and the energy $E = 17.6$ MeV of the D-T reaction. Since the density of tritium and deuterium should be nearly equal in a fusion power plant it is possible to assume $n_D = n_T = n = \frac{n_e}{2}$ as first approximation. Moreover is it possible to approximate the rate coefficient of the D-T reaction $\langle\sigma v\rangle \sim T^2$ in the relevant temperature region between 10 and 20 keV as can be seen from figure 3.1.

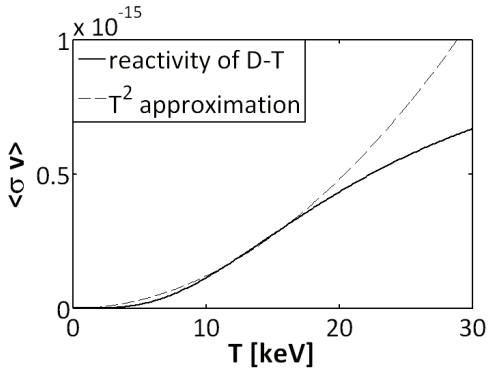

Figure 3.1: Comparison of the real D-T fusion rate coefficient with an T^2 approximation.

In the next step, the integral has been resolved by replacing the density and temperature profiles with line averaged values[1] obtaining the relation

$$P_{fus} \sim\ a^2 R_0\, \bar{n}^2\, \bar{T}^2. \tag{3.5}$$

[1]Here line-averaged values are those with an overline, e.g. $\bar{n} = \int n\,\mathrm{d}\rho$.

To eliminate density and temperature, the dimensionless plasma β is useful. The plasma β reflects the effectiveness of magnetic confinement, but is primarily a physics parameter relevant to stability and equilibrium. With the plasma pressure $p = \sum_j n_j\, k\, T_j$, the plasma $\beta = 2\,\mu_0 \frac{p}{B^2} \sim \frac{n\,k\,T}{B^2}$ can be used to express P_{fus} as

$$P_{fus} = c_1 \frac{\beta^2\, B^4\, R_0^3}{A^2} \tag{3.6}$$

with the aspect ratio $A = \frac{R_0}{a}$. As c_1 is strongly dependent on the profile forms of n and T, c_1 is fitted to comply with more sophisticated transport modelling and resulting values of reactor studies and their operation parameters at a working point.

Power Loss

By inverting the definition of the confinement time (3.2), the power loss of a fusion plasma is

$$P_{loss} = \frac{W}{\tau_E}. \tag{3.7}$$

The plasma energy for a torus geometry can be calculated as

$$W = \frac{3}{2}\,(2\pi a)^2\, R_0\, k \int_0^1 \rho \sum_j n_j\, T_j\, \mathrm{d}\rho. \tag{3.8}$$

With the use of line averaged values one arrives at

$$W \sim\, a^2 R_0\, n\, T. \tag{3.9}$$

As shown in the previous subsection the density and temperature is replaced by the plasma parameter β to obtain the 0-D scaling

$$W = c_2 \frac{\beta\, B^2 R_0^3}{A^2} \tag{3.10}$$

for the plasma energy with a constant c_2 which must analogue be fitted using reactor studies.

The scaling is in principle only valid for already existing, non-ignited devices with nearly no fusion power at all. Therefore the power P of the ISS04 scaling (3.3) refers in existing devices purely to the external heating power P_{Heat}. But as here power plant reactors are considered, which are ignited in a

stationary operation scenario with high amounts of fusion power, P is by far exceeding its validated range. This drawback will here be accepted in favour of the 0-D approximations. Based on the fact, that a fusion plasma in an equilibrium state needs as much heating power as it looses, the approximation

$$P \approx P_{loss} \tag{3.11}$$

may be justified. Finally, one arrives at an implicit equation for the power loss

$$P_{loss} = \frac{W}{\tau_E\left(P_{loss}\right)}. \tag{3.12}$$

This equation can be solved by a root-finder since τ_E is a function of P.

Fitting of constants

To effectively use the derived zero dimensional approximations for the fusion power P_{fus} and power loss P_{loss} it is necessary to fit the constants c_1 and c_2 using values of reactor studies where sufficient modelling exists. Here, the Helias reactor study [53] was selected for fitting and the results are summarised in table 3.1.

Configuration	$\mathbf{c}_1$	$\mathbf{c}_2$
HSR4/18	0.004276	0.117512
HSR5/22	0.004215	0.116933

Table 3.1: Constants for the 0-D scalings using values of the HSR4 and HSR5 reactor studies for fitting.

3.2 Power balance of a fusion reactor

A fusion reactor uses an exothermic reaction to release energy. The released power $P_{fus} = P_n + P_\alpha$ is thereby concentrated as kinetic energy in fast particles, respectively in 14.1 MeV neutrons and 3.5 MeV alpha particles. The neutrons are absorbed by the blanket and the shield and get slowed down while their kinetic energy is transformed into heat. This heat will be conducted by the integrated cooling system and converted to electricity with an efficiency η_{th}.

$$P_{el} = \eta_{th} P_{th} \tag{3.13}$$

The thermal power is thereby composed of the fusion power $M \cdot P_{fus}$, where the factor M is the additional energy generated by nuclear reactions in the blanket, of the external heating power P_{Heat} and of the usable thermal energy produced by the balance of plant $\eta_{BOP}P_{BOP}$, see definition in chapter 1:

$$P_{th} = M \cdot P_{fus} + P_{Heat} + \eta_{BOP}P_{BOP} \tag{3.14}$$

During the startup phase of the power plant it is essential to bring as much external heating power into the plasma as is lost. When the temperature is sufficiently high, the fusion reaction contributes significantly and the alpha particles start to heat the plasma in the core region. This can be written as

$$P_{Heat} = P_{loss} + P_{Brems} - P_{\alpha} \tag{3.15}$$

for the required external heating power. To operate a fusion power plant, power is required to maintain all operating systems summarised in P_{BOP} and also requiring power for the external heating source $\frac{P_{Heat}}{\eta_{Heat}}$. These two main parts build the auxiliary power system

$$P_{AUX} = \frac{P_{Heat}}{\eta_{Heat}} + P_{BOP} \tag{3.16}$$

which can directly be supplied by the electrical power produced by the plant. The resulting net electrical power

$$P_{el.net} = P_{el} - P_{AUX} \tag{3.17}$$

can be provided to the power grid. The fraction of power, which must be recirculated into the power plant is therefore given by

$$f_{rec} = \frac{P_{AUX}}{P_{el}}. \tag{3.18}$$

Finally the fusion gain Q shall be defined here:

$$Q = \frac{P_{fus}}{P_{Heat}} \tag{3.19}$$

In that frame, a fusion plasma is called *burning* if only a small amount of external heating power is required ($Q \gg 1$) and a self-sustaining plasma is called *ignited* with no external heating power at all ($Q = \infty$).

3.3 Application of the 0-D approximations

Using the described tools, parameter scans can be carried out to study the operation parameters of reactors. The following studies investigate the minimum size for ignition using different scalings and the net electrical power which can be supplied to the power grid as well as the fraction of power which needs to be recirculated to operate the power plant. Finally the impact of a higher magnetic field strength on plasma performance and the importance of the renormalisation factor will be investigated.

Fusion power and fusion gain

An essential geometrical parameter of a Stellarator is the major radius R_0. While keeping the aspect ratio constant, the major radius represents the size of the machine. A larger volume has positive aspects in matter of constructibility and plasma confinement, but the costs of a reactor scale with the volume, too. Therefore from an economic point of view a reactor should be kept small.

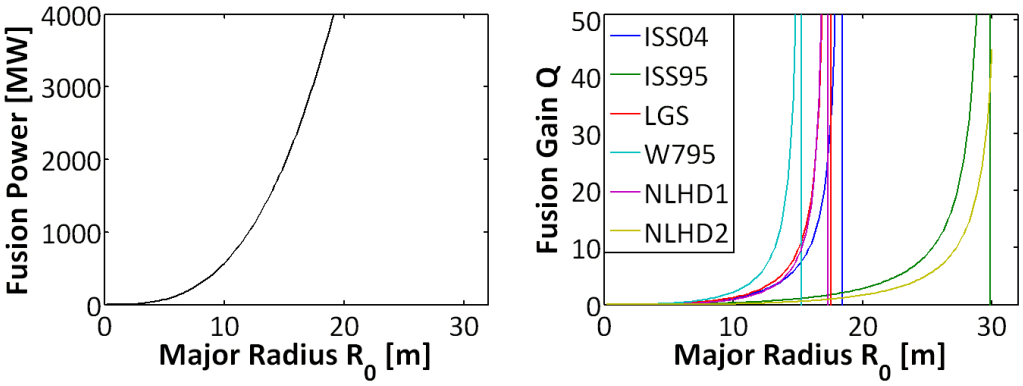

Figure 3.2: Fusion power dependent on reactor size using ISS04 (left) and fusion gain in dependence of reactor size for different scalings [53] (right) with parameters of the reactor study HSR4/18 [4].

The left side of figure 3.2 shows the strong increase of the fusion power with volume due to the R_0^3 dependence of the fusion power formula (3.6). A sufficient supply of electrical power to the power grid, e.g. like from fission power plants, is normally in the range of around 1 GW. Depending on the thermal efficiency, a fusion power plant needs at least $3 \ldots 4$ GW of fusion power to produce the required electrical power, see figure 3.3 below. Therefore a Helias reactor must have a size between $18 \ldots 20$ m following the ISS04 prediction of the left plot

of the figure 3.2. The right hand side of the figure shows the ignition radius for different scalings [53] represented by the vertical lines where $Q = \infty$. It shows also the large scattering of the results for the different scalings. Most optimistic size gives the W795 scaling with an ignition radius of 15 m while the most pessimistic results come from the NLHD2 scaling with ignition at 30 m. The results predicted from NLHD1, LGS [53] and ISS04 are in a moderate range between 17.5 m and 19 m with some scatter.

Net electrical and recirculating power

The net electrical power which can be supplied to the power grid and the fraction of power to be recirculated for plant systems are simple figures of merit for reactor operation and are therefore discussed here.

To calculate these powers, the thermodynamic conversion efficiencies must be assessed. This can be done for two basic cooling concepts. The first is the concept of 'conservative' liquid water cooling with a thermal conversion efficiency $\eta_{th} = 0.33$ and moderate power for the balance of plant $P_{BOP} = 50$ MW. The second concept employs the idea of gaseous helium cooling for which technological advancements are required and therefore this scenario is called 'advanced cooling' in the following with a higher thermal efficiency $\eta_{th} = 0.5$ but a penalty for the additional pumping power resulting in $P_{BOP} = 200$ MW [3].

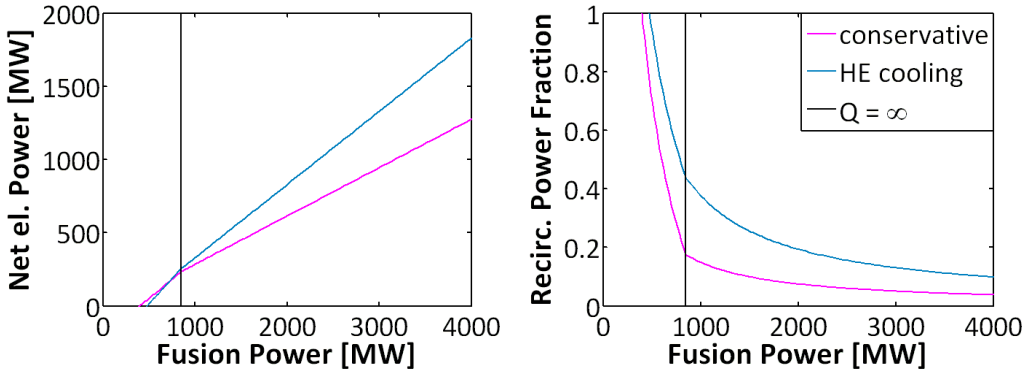

Figure 3.3: Net electrical power as function of fusion power (left) and recirculating power fraction in dependence of fusion power (right), with conservative cooling (magenta line) and advanced helium cooling (blue line), for HSR4 reactor parameters with an assumed 'optimisation' of $f_{ren} = 1.1$, see 3.4.

The left side of figure 3.3 shows that the reactor ignites at small values of

fusion power (black line) and from there the net electrical power linearly scales with the fusion power. The higher thermal efficiency of the helium cooling then leads to a higher net electrical power output compared with conservative water cooling. On the right side of figure 3.3 the recirculating power fraction drops drastically to the point, where the plasma ignites, because at this point no more external heating power is required. After ignition the higher pumping power of the helium cooling demands roughly twice the recirculated power fraction of the water cooling. In summary the advanced helium cooling needs more recirculating power for operation but this is easily compensated by the higher thermal conversion efficiency leading to a higher net electrical power output.

Magnetic field strength

As was seen in the derivation of the fusion power, the substitution of density and temperature leads to a magnetic field dependence of $P_{fus} \sim B^4$ for a constant β. If the magnetic field strength is augmented while keeping β constant, e.g. through higher density, the fusion power should increase strongly. This is the case as can be seen in figure 3.4 where the fusion power is shown as function of the magnetic field strength for two cases, namely for a constant $\beta = 3.6$ % (left) and $\beta = 4.9$ % (right). To keep β constant, the density was increased parallel to the magnetic field shown as the scale on top of the figure. Additionally two technological constraints are plotted in the graphs. Namely the maximum field strength on the axis of the magnetic field $B_t = 4.5$ T of a NbTi superconductor and the maximum field strength 5.6 T of advanced superconductors like Nb_3Sn or Nb_3Al. It can be seen in the figure, that a technological advancement from 4.5 T to 5.6 T has a great impact on the fusion power. If the density is in parallel increased to keep β constant, the fusion power for the $\beta = 3.6$ % case of the left side is doubled. This is also obvious on the right side of the figure where for the $\beta = 4.9$ % case an increase from 4.5 T to 5.6 T leads again to at least a doubling of the fusion power. It can be concluded that the magnetic field strength and the plasma β have a great impact on the resulting fusion power.

For this reason, the possibility of higher magnetic field strengths was investigated [54] and concluded that both Nb_3Sn and Nb_3Al superconductors could be safely applied to Stellarators. Both technologies would allow operation of

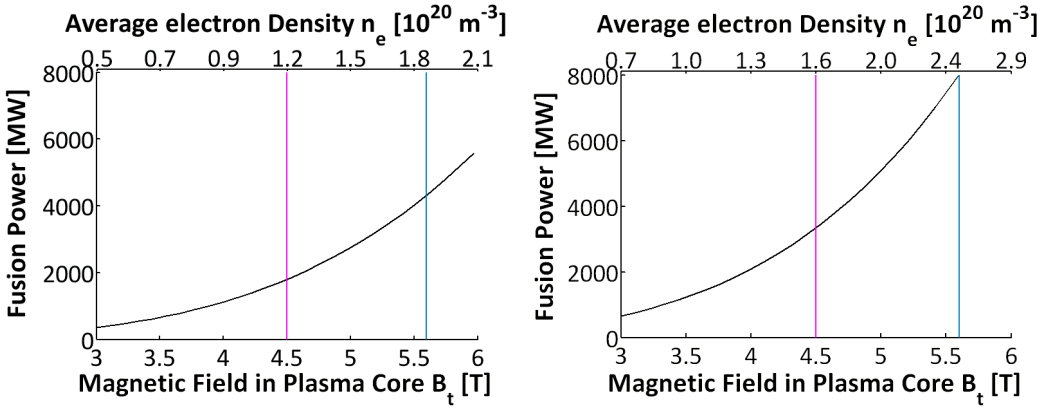

Figure 3.4: Fusion power as function of the magnetic field strength for HSR4 parameters with constant $\beta = 3.6$ % (left) and $\beta = 4.9$ % (right) where the magenta line is the maximum field strength of an NbTi superconductor at 4.2 K and the blue line is the maximum field strength of Nb_3Sn / Nb_3Al superconductors at 4.7 K.

a reactor at a higher magnetic field with the shown resulting improvement of plasma confinement. This, in turn, would permit a reduction of the machine size and an increase in the amount of space available for blanket and shield.

3.4 The renormalisation factor

The renormalisation factor f_{ren} is a parameter which was introduced into the ISS04 scaling law to account for different Stellarator magnetic configurations. Due to the different approaches used for the three dimensional magnetic field shaping, individual machines have different geometries and thus confinement behaviour. The renormalisation factor f_{ren} solved this issue by regression of device subgroups in the ISS04 scaling. Each Stellarator subgroup is assumed to have its own renormalisation factor to correct the energy confinement time with respect to the basic ISS04 scaling.

$$\tau_E = f_{ren} \cdot \tau_E^{\mathrm{ISS04}} \tag{3.20}$$

To demonstrate the importance of this renormalisation factor, calculations of the minimal radius required for ignition of a reactor with HSR4 parameters have been made. The results are seen in figure 3.5 with the red line showing the strong dependence of the minimal radius required for ignition on

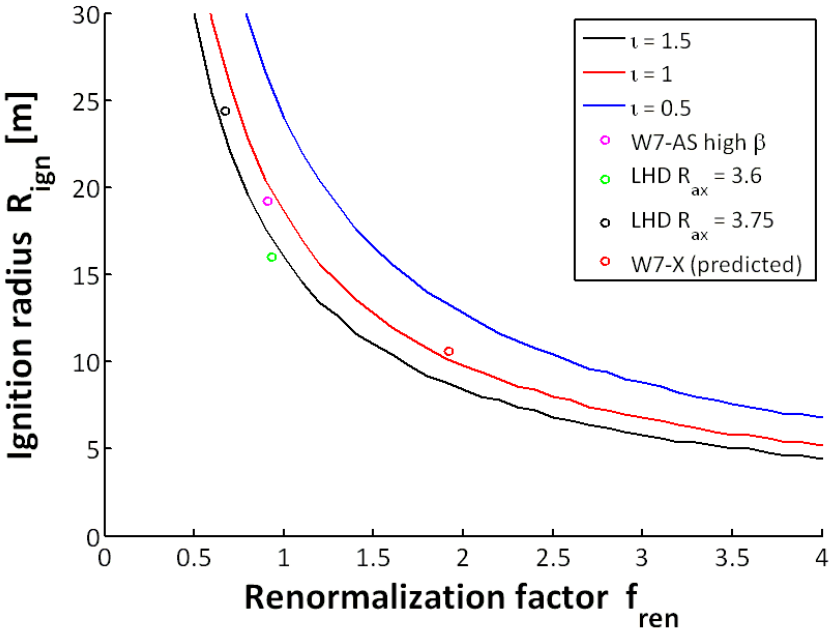

Figure 3.5: The minimum major radius for plasma ignition for a HSR4 Stellarator-type reactor is shown in dependence of the renormalisation factor with reference points for different devices. The lines show the sensitivity of this function by varying the least important parameter ι by $\pm 50\%$ around $\iota = 1$.

the renormalisation factor using the ISS04 scaling with $\iota = 1$. The sensitivity of this graph on this quantity is demonstrated by varying the parameter ι by ± 50 %. The figure also shows points of existing devices, namely W7-AS with $f_{ren} \approx 1$ starting igntion around 20 m major radius. The impact of the magnetic configuration can be seen from the two different LHD configurations. The less favourable '$R_{ax} = 3.75$' configuration would ignite beyond 25 m and the more favourable '$R_{ax} = 3.6$' configuration at around 16 m. The optimised W7-X magnetic configuration has a predicted renormalisation factor of $f_{ren} \approx 1.9$ significantly reducing the radius required for ignition to 11 m. It can be summarised that the optimisation of the magnetic configuration here represented by the introduced renormalisation factor has a great impact on plasma performance and size of the machine required for ignition or power plant operation.

3.5 Stepladder to a fusion power plant

To illustrate the capability and the parameter range of existing and planned devices in a broader context, dimensionless engineering parameters $B^* \propto B_t\, a^{5/4}$, $P^* \propto P_{Heat}\, a^{3/4}$ and $n^* \propto n\, a^{3/4} B_t^{-1}$ were introduced [55]. This choice of variables is not unique, but allows to use design parameters of envisaged devices rather than physics parameters of unknown performance. With these specifications it is possible to map and compare geometrical similar devices in this three dimensional parameter space. Using the empirical scaling law ISS04 it is then possible to produce isocontours for the commonly used dimensionless physics quantities β, ρ^* and ν^* in this coordinate system as can be seen in figure 3.6.

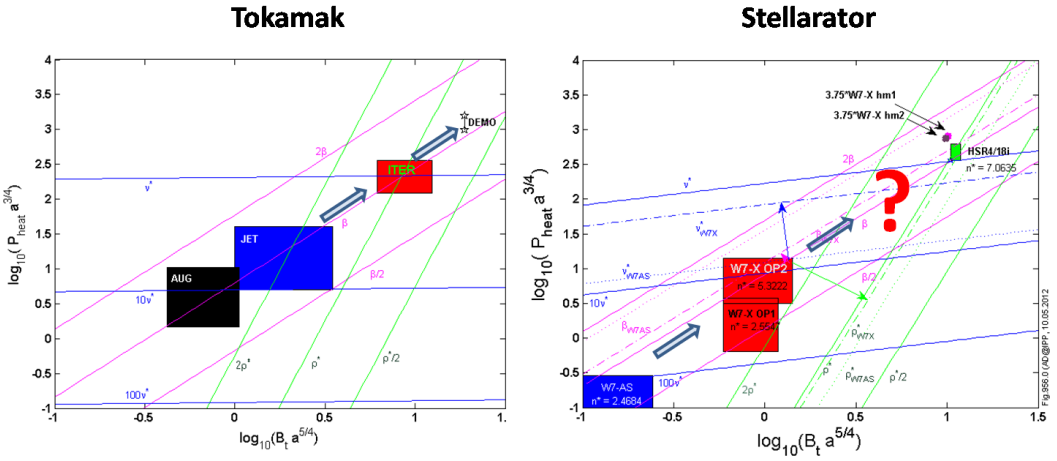

Figure 3.6: Dimensionless plasma physics parameters at constant n^* with the ITER-98y2 confinement law assumptions with corresponding isocontours of β, ρ^* and ν^* for Tokamaks (left) and analogoue for Stellarators under the assumptions of ISS04 scaling and non-constant n^* leading to a 3-D coordinate system where the dashed lines are projections into the plane of the HSR4/18i reactor (right). (A. Dinklage, personal communication 2012 [56])

The figure demonstrates that the parameter space for Tokamaks is well covered with reasonable steps between existing devices[2] and ITER being a keystone with regard to building a Tokamak DEMO reactor. For Stellarators it can be seen, that already the step from W7-AS to W7-X is very large. It

[2]The shown devices are AUG (Axially Symmetric Divertor-Experiment - Upgrade), the largest fusion device in Germany of the Tokamak type operated by the Max Planck Institute for Plasma Physics, Garching and JET (Joint European Torus), the largest Tokamak experiment in the world collectively used by the EURATOM Associations operated at Culham Centre for Fusion Energy, Great Britain.

is also evident that there exists a huge gap between W7-X and a DEMO-like reactor. This gap raises the question, whether it would be useful to build an intermediate device to decrease the development risk of a DEMO reactor. Such an intermediate machine could be used to explore, on the one hand, the reactor-like physics parameters ρ^* and ν^* and, on the other hand, the physics of an ignited plasma with $Q \geq 10$.

To answer this question an in-depth investigation of larger devices with the underlying physics is required. To start this task it is reasonable to advance from 0-D approximations to 1-D simulations which is done in the next chapter. But it can already here, in figure 3.6, be seen, that the three dimensionless quantities β, ρ^* and ν^* cannot be held constant at the same time while changing engineering parameters. This will become especially clear in subsection 4.2.2, where motivated from the isocontours of β of figure 3.6 a scaling simulation was performed with constant β.

Chapter 4

1-D Model

4.1 The 1-D Code

In this study, a one dimensional transport code [5, 57, 58] has been employed. The code numerically evaluates the energy and particle fluxes constrained by the plasma ambipolarity condition. Originally the transport code used here was developed by Yuriy Turkin [5, 57, 58], IPP Greifswald, to study confinement properties of W7-X and beyond to get an impression of the performance limits of the device. Moreover it is possible to linearly scale up W7-X with the predictive code which was done in the frame of this work. The advantage of the 1-D simulations over the 0-D approximations is the use of *profiles*. A profile means here a relevant physics quantity which is dependent on one space dimension, namely the radial coordinate r, measured from the plasma core to the plasma boundary. The profiles are dependent on the radial flux surface label. With the extension of the radial parameter compared to the 0-D scalings, profile effects and especially transport regimes can be simulated and investigated. The way the 1-D code calculates the plasma transport and the corresponding profiles will be explained in the following.

Power balance equations

The power balance of the plasma consists of two parts, one for electrons and one for ions. Both are similar on the left side describing the temporal and spatial evolution of the energy flux densities with V' being the Jacobian of the

magnetic field coordinates. The righthand side of the equations

$$\frac{3}{2}\frac{\partial n_e T_e}{\partial t} + \frac{1}{V'}\frac{\partial}{\partial \rho}V' Q_e = P_e - \Gamma_e E_r - P_{ei} - P_{rad} \quad (4.1)$$

$$\frac{3}{2}\frac{\partial n_i T_i}{\partial t} + \frac{1}{V'}\frac{\partial}{\partial \rho}V' Q_i = P_i + Z_i \Gamma_i E_r + P_{ei} \quad (4.2)$$

consists of the power sources and sinks, namely the external heating power P_α with the particle species $\alpha = e; i$, the power gain and loss due to electric field E_r, the bremsstrahlung P_{rad} and the term which describes the collisional power exchange between electrons and ions P_{ei}. In addition the ambipolarity constraint $Z_i \Gamma_i = \Gamma_e$ is solved to obtain the radial electric field E_r. However, this approach is in most cases not numerically suitable because of the discontinuity and the bifurcations of the solution. If the ambipolarity constraint is solved by means of root finding, multiple solutions for E_r could arise (cf. figure 2.5). The problem of the different roots and the transition between one root and another can be circumvented with a diffusion equation for the electric field, which follows from a thermodynamic approach [59, 60]

$$\frac{\partial E_r}{\partial t} - \frac{1}{V'}\frac{\partial}{\partial \rho}V' D_E \left(E_r' - \frac{E_r}{\rho} \right) = \frac{|e|}{\epsilon} \left(\Gamma_e - Z_i \Gamma_i \right) \quad (4.3)$$

with a diffusion coefficient D_E for the electric field. This approach avoids the named problems through its 'smearing' effect meaning that the diffusive nature of equation (4.3) leads automatically to a smooth electric field profile if multiple roots of the ambipolarity condition are present.

The power balance equations and the electric field equation are solved self-consistently using an implicit Runge-Kutta method and result in a stable solution with steady-state profiles.

The particle fluxes Γ_α and energy fluxes Q_α of the power balance are commonly divided into a neoclassical and an anomalous part.

$$\Gamma_\alpha = \Gamma_\alpha^{neo} + \Gamma_\alpha^{ano}, \quad Q_\alpha = Q_\alpha^{neo} + Q_\alpha^{ano} \quad (4.4)$$

The detailed analysis of neoclassical and anomalous fluxes will be given in the following.

Description of neoclassical transport

Following the principle of thermodynamic forces, see subsection 2.2.1, both energy and particle flux of neoclassical transport theory are described by the expressions

$$\Gamma_\alpha^{neo} = -n_\alpha \left[D_{11}^\alpha \left(\frac{n'_\alpha}{n_\alpha} - \frac{Z_\alpha E_r}{T_\alpha} \right) + D_{12}^\alpha \frac{T'_\alpha}{T_\alpha} \right] \quad \text{and} \tag{4.5}$$

$$Q_\alpha^{neo} = -n_\alpha T_\alpha \left[D_{21}^\alpha \left(\frac{n'_\alpha}{n_\alpha} - \frac{Z_\alpha E_r}{T_\alpha} \right) + D_{22}^\alpha \frac{T'_\alpha}{T_\alpha} \right]. \tag{4.6}$$

For the calculation of the fluxes, the diffusion coefficients D_{ij}^α are to be determined. In this representation are $D_{11} = L_{11}$, $D_{21} = L_{21}$, $D_{12} = L_{12} - \frac{3}{2}L_{11}$ and $D_{22} = L_{22} - \frac{3}{2}L_{21}$ compared with the L_{ij} of the transport matrix used in subsection 2.3.2. For this task the drift kinetic equation (2.43) has to be solved numerically. In the present case a database of monoenergetic coefficients [30] was precalculated using the DKES[1] code for different magnetic configurations of W7-X. Then the diffusion coefficients are produced for arbitrary plasma parameters by the appropriate energy convolutions of interpolated results from the DKES database. The results were used by the 1-D transport code [62].

Description of anomalous transport

Because of the fact that first principle descriptions of anomalous transport are still work in progress [47], semi-empirical models are used to characterise anomalous transport properties. Although anomalous energy and particle flux can be described by diffusion equations

$$\Gamma_\alpha^{ano} = -D^{ano} n'_\alpha \tag{4.7}$$

$$Q_\alpha^{ano} = -\chi_\alpha^{ano} n_\alpha T'_\alpha + \frac{5}{2}\Gamma_\alpha^{ano} T_\alpha, \tag{4.8}$$

it is possible to freely choose a model for the diffusion coefficients. The basic approach in this context is the so called $1/n$ model. In the Stellarator W7-AS it was indicated [63, 64] that the anomalous diffusion coefficients behave inverse to the density $\chi^{ano} \propto 1/n$. A similar model is the $1/n$-edge model. In this model the diffusion coefficients are proportional to the inverse of the density too, but decay exponentially to the plasma core, which incorporates

[1] Drift Kinetic Equation Solver [61, 41]

the idea, that neoclassical transport dominates the core while the edge region is dominated by anomalous transport. A somewhat different approach is the ion-temperature-gradient model. As the name states it is based on the ITG-phenomenon often observed in Tokamaks, where the anomalous diffusion is strongly present when the temperature gradient exceeds a critical value. The diffusion coefficients can be compared in figure 4.1.

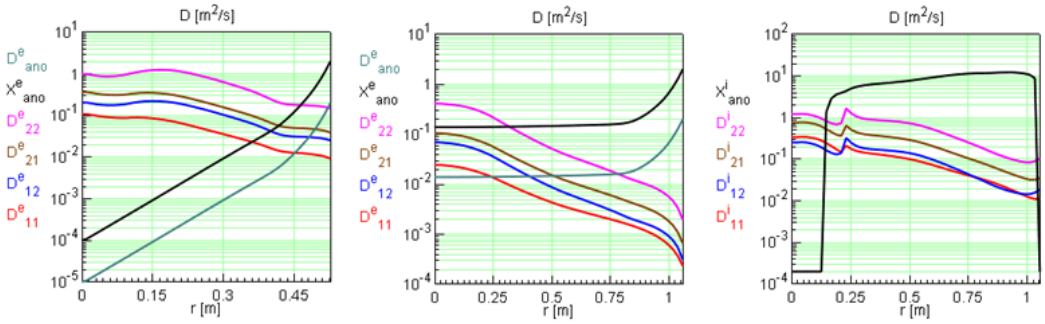

Figure 4.1: Coloured lines represent the neoclassical monoenergetic diffusion coefficients and the black line the anomalous diffusion coefficient of the corresponding model: $1/n$ (middle) $1/n$-edge (left) and ITG (right). (The plots are examples of different transport simulations and shall schematically demonstrate the behaviour of the diffusion coefficients)

4.2 Application of the 1-D-model

Input parameters

To operate and use the 1-D code correctly it is essential to carefully define an ensemble of physically reasonable input parameters. In the context of reactor scaling it is also important to account for material and technical constraints to avoid unrealistic simulation results.

A major input parameter is the density profile $n(r)$. Because it is not yet possible to create a self-consistent description of particle transport, it has been assumed, that density control is sufficient to keep a fixed density profile as seen on the left side of figure 4.2.

To heat the plasma and sustain an equilibrium state, an external heating source has to be defined. In W7-X this can either be done by NBI[2] or ECRH. To fully understand the ECRH heating a detailed description of plasma waves would be required (cf. [20]). This would be out of proportion for this work and is therefore not discussed here. However, the basic principle of the electron cyclotron resonance heating is the heating of electrons using radio waves. Two basically different heating modes can be distinguished. These are the ordinary waves (O-mode) polarised such that the electric field is parallel to the equilibrium magnetic field ($E \| B_0$) and the extraordinary waves (X-mode) correspondingly polarised perpendicular to the equilibrium magnetic field ($E \perp B_0$). Due to the inhomogentiy of the magnetic field strength ($B \sim 1/R_0$), only those electrons are heated which satisfy the cyclotron beam mode dispersion relation $\omega_e = l\frac{eB}{\gamma m_e} + kv_\parallel$ [65] with the mode number l, the relativistic factor γ and the wave number k. This leads to a very localised heating meaning, that in a sufficient approximation the full power of the ECRH gets deposited locally in the electrons. Therefore the heating power absorption has been modelled in a Gaussian shape, see right side of figure 4.2, which is a justifiable approximation compared to a real heating profile. Additionally it must be considered that ECRH heating only works up to a critical density of the electrons, the so-called cut-off density. The microwave does not penetrate into the plasma if its density is above the cut-off value. Those cut-offs have to be considered in the simulations and the relevant values are summarised in table 4.1.

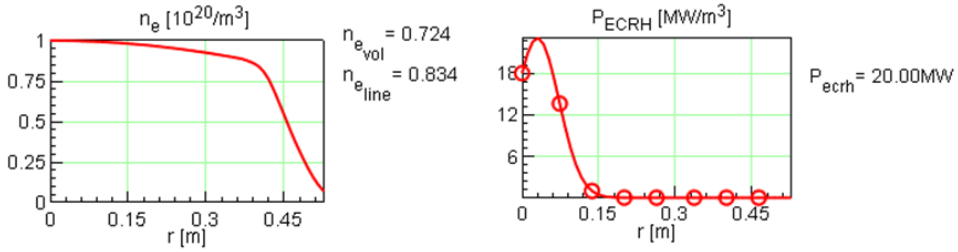

Figure 4.2: Example of a fixed density profile (left) and central Gaussian shaped ECRH heating profile (right).

[2]NBI (neutral beam injection) is the heating by means of accelerated neutrals. Other heating methods are, e.g., ICRH (ion cyclotron resonance heating), which uses microwaves of the ion cyclotron frequency, effectively heating the ions, and LH (lower hybrid heating) relevant for Tokamaks, but not considered for reactor-sized Stellarators.

Gyrotron	**B_t**	**O1-mode**	**O2-mode**	**X2-mode**
140 Ghz	2.5 T	-	2.4	1.2
140 Ghz	5.0 T	2.4	-	-
170 Ghz	6.1 T	3.6	-	-
280 Ghz	5.0 T	-	9.6	4.8

Table 4.1: Electron cut-off densities in $10^{20}\mathrm{m}^{-3}$ for different ECRH heating modes at different magnetic field strengths assuming W7-X, ITER and advanced gyrotrons with 140, 170 and 280 Ghz respectively.

In addition the code supports different equilibrium configurations of the magnetic field of W7-X. Without going into detail, it can be chosen between a standard configuration calculated for a plasma equilibrium with $\langle\beta\rangle = 4$ % and a high-mirror configuration with $\langle\beta\rangle = 4$ %, which has a major impact on the profiles. Additionally the magnetic field strength on the field axis B_0 can be varied. Also as stated in the description of the code a choice can be made regarding the anomalous transport model leading to problems which will be explained later on.

4.2.1 Scaling of the volume

In the transport code the geometric input quantities can be scaled. To illustrate this, a scale factor S can be introduced. This means for the scaling factor S the radii change to $R' = S \cdot R$, $a' = S \cdot a$ and the volume becomes $V' = S^3 \cdot V$. This allows a scaling study of the volume to be performed. In a first approach all input parameters are left constant and only the size of the machine is changed.

Scaling	Machine	R_0 [m]	a [m]	volume [m^3]
1	W7-X times 1	5.5	0.53	30.5
2	W7-X times 2	11.0	1.05	243.7
3	W7-X times 3	16.6	1.58	822.3
4	W7-X times 4	22.1	2.12	1949.2

Table 4.2: Scaling factor with the corresponding size parameters and the name used throughout the work.

The results of the modelling are shown in figure 4.3. It can be seen that the confinement time of the plasma increases with size. But the behaviour is different compared to the prediction by ISS04. Using basic logarithmic

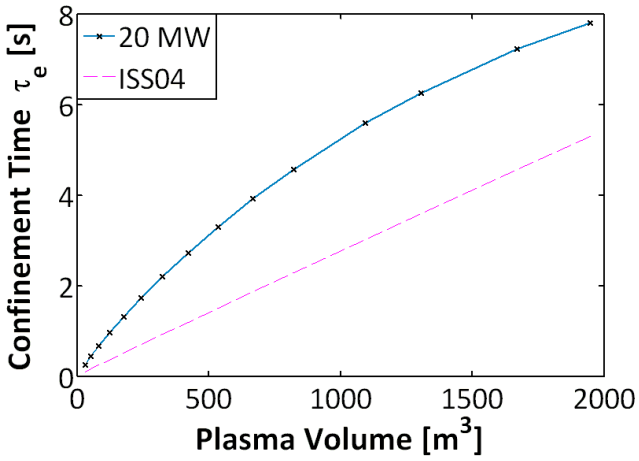

Figure 4.3: Upscaling of W7-X showing the confinement improvement with size (solid line) compared with ISS04 prediction (dashed line) with input parameters $n_0 = 10^{20}$ m^{-3}, $B_0 = 2.38$ T, standard magnetic configuration $\langle\beta\rangle = 2$ %, 20 MW heating power and anomalous $1/n$-edge model.

fitting of the results of figure 4.3, the ISS04 shows a nearly linearly scaling $\tau_E^{ISS04} \propto V^{0.97}$ while the simulation results seem to scale only with $\tau_E \propto V^{0.83}$. To explain the difference the global parameters β and $f_{ren} = \tau_E/\tau_E^{ISS04}$ are assessed in more detail.

Figure 4.4 shows the change of β and f_{ren} during the upscaling where only the size of the machine was changed. Both parameters decrease significantly over the range of the size variation. The strong decrease of β is comprehensible, because the heating power is constant and therefore the power-density of the plasma (P_{Heat}/V) decreases due to the larger size of the machine. As the density profile was also left constant, the temperature must decrease with the lower power-density and therefore also β. Somewhat more intricate is the decrease of the renormalisation factor, right side of figure 4.4. Although the confinement time of the simulation is larger than expected from the ISS04 scaling, the ratio of τ_E/τ_E^{ISS04} is decreasing.

As both β and f_{ren} show similar characteristics, a relation between those two parameters could be assumed. This assumption is supported by the evaluation of LHD data, which showed the same behaviour [66].

To investigate this issue further and to circumvent the problem of constant heating power a scaling in relation to the step-ladder plot 3.6 is useful. Referring in this context also to the similarity principle explained in the last chapter

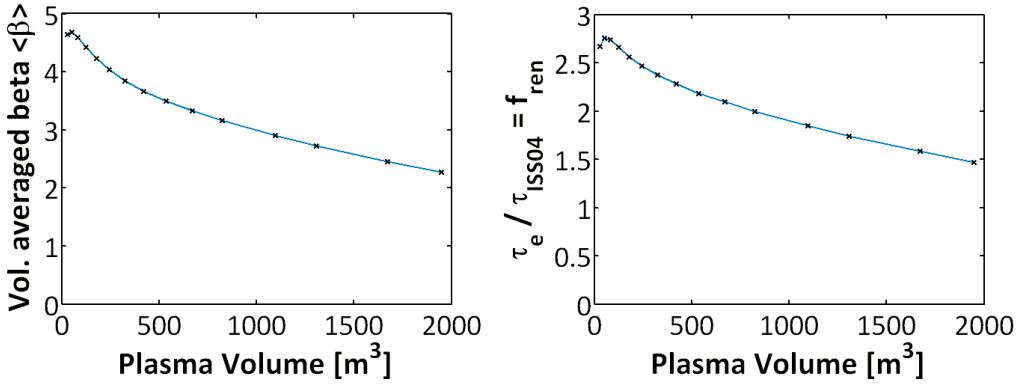

Figure 4.4: Upscaling of size with constant input parameters yields a decreasing β (left) and a decreasing renormalisation factor (right).

it is reasonable to change the dimensionless quantities β, ρ^* and ν^* only slightly over an upscaling to guarantee comparability. Due to the interplay between the particle and energy transport and the dimensionless quantities it is not easily possible, to keep β, ρ^* and ν^* constant at the same time. For that reason the following scalings were performed with one constant quantity, namely the plasma β, as previously discussed 3.5.

4.2.2 Scaling at constant β

To achieve a constant β for different sizes of a machine, the density, magnetic field and heating power can be changed. To keep the number of changing variables to a minimum, density and magnetic field were fixed and in parallel, volume and heating power increased. To ensure comparability all following simulations were done iteratively to achieve the same β value. For comparability with the HSR4/18i reactor study [67], $\beta = 3.6\%$ was choosen.

In order to study the underlying physics of the simulations, the scaling at constant β was performed using cases with low and high density and magnetic field strength. The results are shown in figure 4.5 demonstrating, that the renormalisation factor f_{ren} is still decreasing for all cases with size of the machine, although β was fixed. The decay of f_{ren} varies for the considered cases. This means that f_{ren} cannot be easily described by n and B. This makes it questionable to use the ISS04 for scaling studies and shows that it cannot be used for W7-X reactor predictions even with an assumed constant renormalisation factor [68].

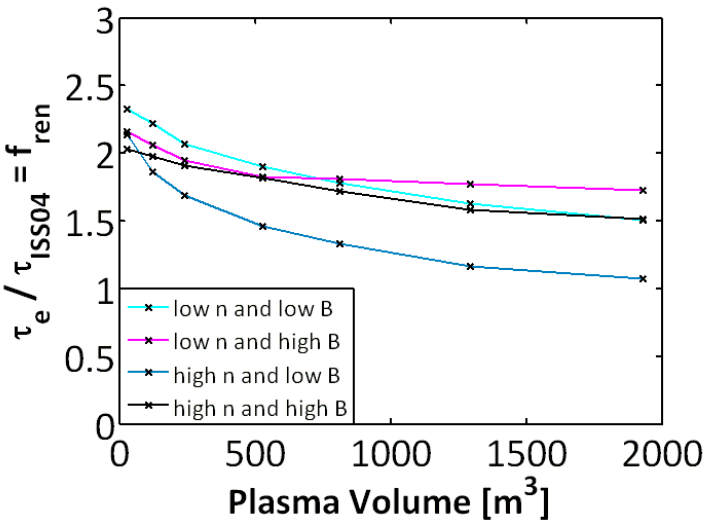

Figure 4.5: Renormalisation factor for upscaled W7-X like configurations with low and high density $\bar{n}_e$, 1.13 and $1.75 \cdot 10^{20}$ m^{-3} respectively, and low and high magnetic field strength B_0, 2.38 and 4.75 T respectively, for the high mirror configuration with a constant $\beta = 3.6\%$ achieved by variation of heating power.

As a general observation, there is a similar decay of f_{ren} for different cases of parameter choices. Since all upscaling simulations have shown this characteristic so far, it is reasonable to investigate this issue in more detail. How this issue is related with the ISS04 scaling will be addressed in the next subsection.

4.2.3 Change of the transport channel

To really understand the general phenomenon of the non-linear decay of the renormalisation factor with size, a detailed look at the transport is necessary. In a first step the electron and ion energy fluxes are compared for the scenario of low density and low magnetic field. As can be seen in figure 4.6, the main energy flux for 'W7-X times 1', especially in the centre, is due to the electrons. This feature changes over the upscaling, so that the main energy flux comes from the ions meaning, that a reactor sized W7-X is dominated by ion heat flux. It can be concluded that in this scenario the dominant transport channel changes from the electrons to the ions while going from a small to a large Stellarator.

Discussing the transport regimes, the electrons reside for every Stellarator size mainly in the $1/\nu$-regime, but the strong ion transport in reactor size plasmas suggests that the ions change their transport regime. To investigate

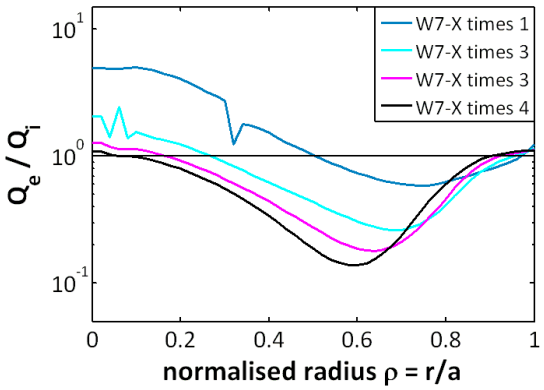

Figure 4.6: Ratio of electron heat flux to ion heat flux for the low density and low magnetic field case of the $\beta = 3.6\%$ scaling for different sizes of W7-X. (The spikes in the 'W7-X times 1' and '2' case are a numerical effect due to the electric field changeing its sign)

this, the ion transport regime must be determined. Because the ion diffusion coefficients depend strongly on the electric field in the 'W7-X times 1' case as seen in figure 4.7, the ions must be mainly in the $\sqrt{\nu}$-regime with regard to energy transport.

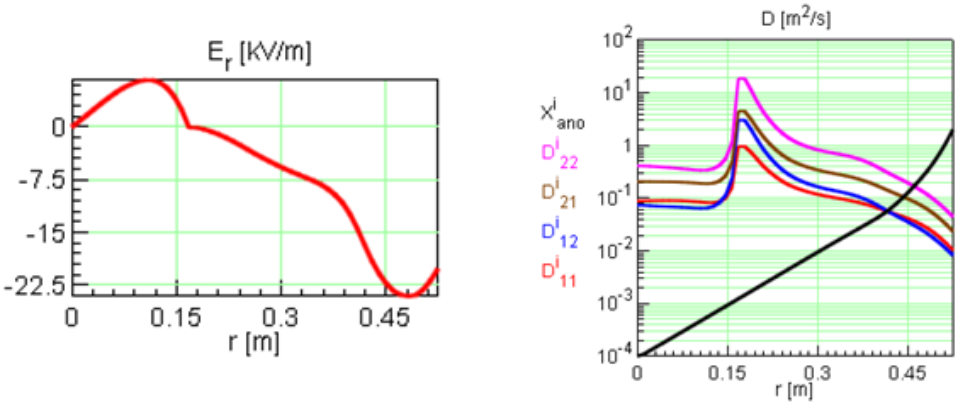

Figure 4.7: Radial electric field (left) and ion diffusion coefficients (right) for W7-X case of the low density, low magnetic field scenario.

To determine the ion transport regime of the reactor-size W7-X, an in-depth look at the underlying physics is necessary. The general observation made in an upscaling simulation is the increase of the collisionality. This indicates that a larger fraction of the ion distribution function finds itself in the pure plateau-regime and the transport becomes increasingly collisional. To find a criteria

for this transition, it is useful to look at the electrons. The electrons leave the long-mean-free-path (lmfp) regime when their plateau transport becomes larger than the $1/\nu$ transport, which means $D_{pl} \geq D_{1/\nu}$. If the analytical expressions for the corresponding regimes [42] are inserted, the criterion can be expressed using the effective helical ripple ϵ_{eff} and magnetic field elongation $\kappa = (\epsilon_t/\epsilon)^2$ as

$$\frac{\nu\, R}{v\, \iota} = \nu^* \geq \frac{16}{9\pi^2} \left(2\, \epsilon_{eff}\right)^{3/2} \kappa. \tag{4.9}$$

To compare this monoenergetic criterion with the thermal collisionality[3], it has to be taken into account, that the main contribution of the plateau regime does not come from the particles with thermal energy but from the particles with approximately twice the thermal energy. Because $\nu^* \propto \frac{1}{E^2}$ this results in a factor four in the criterion.

$$\nu^*_{th} = 4 \cdot \nu^* \tag{4.10}$$

This dependence ($\nu^* \propto \frac{1}{T^2}$) also explains the general increase of the collisionality with increasing radius, e.g. figure 4.8. Due to the strong temperature gradient of fusion plasmas with low temperatures at the plasma boundary, the collisionality must inversely increase strongly. This means that those reactor cases with a comparably extended region of low temperature have also a high collisionality and vice versa.

Using the dimensionless description introduced above, the demonstrated electron regime transition criterion is equivalent with the lmfp transition of the ions. Figure 4.8 shows, that in the 'W7-X times 1' case the ions remain in the lmfp-regime nearly up to the plasma edge and are therefore in the $\sqrt{\nu}$-regime. The figure also shows, that in this scenario the collisionality increases with size and especially strong at the plasma edge. This means, that during the upscaling the ion distribution function shifts more and more to the collisional plateau regime. In the 'W7-X times 4' case the ions are only in the plasma centre in the $\sqrt{\nu}$-regime while ions at outer radii reside in the more collisional plateau regime.

Now if one assumes, as in the 'W7-X times 4' case, that $Q_i >> Q_e$ as seen in figure 4.6, with the ions to a large degree in the plateau-regime, the heating

[3]Thermal collisionality means collisionality of the particle at thermal velocity.

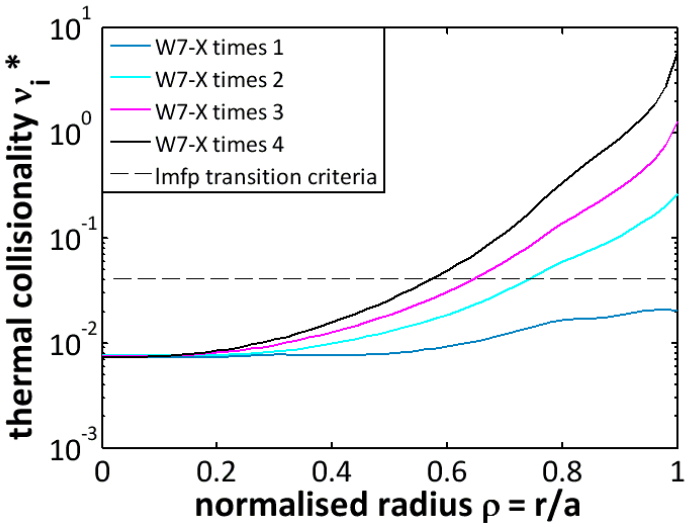

Figure 4.8: Thermal collisionality ν^* of the ions for the cases from W7-X to 'W7-X times 4' with the corresponding lmfp transition criterion (dashed line) for the low density, low magnetic field scenario.

power must be balanced by the ion heat flux

$$P \sim Q_i \propto nT_i D_{11}^i. \tag{4.11}$$

With the analytical representation of $D_{12}^i \propto \frac{T_i^{3/2}}{B_0^2 \bar{\iota}}$ the confinement time can be written as

$$\tau_E \propto \frac{nT_i}{P} \propto n^{0.6} P^{-0.6} B^{0.8}\, t^{0.4} \tag{4.12}$$

much resembling the ISS04 scaling [68]. Consequently, a scaling for high collisionality conditions should converge to a constant renormalisation factor.

In order to confirm a small variation of f_{ren} at high collisionalities, a scaling was performed using high density and low heating power. This ensures high collisionality for all cases with a sufficient part of the ions being in the plateau-regime. As can be seen on the left side of figure 4.9, the local collisionality may vary, but the line averaged value $\langle \nu^* \rangle$ is for all cases of the same order. Additionally all sizes of this scenario are well over the lmfp transition criterion. The right side of figure 4.9 shows the resulting renormalisation factor of this scenario. As expected the ratio τ_E / τ_E^{ISS04} is constant meaning that the exponential relations of the ISS04 scaling agree with the plateau regime scenario simulations. Therefore the ISS04 scaling is only valid for the collisional plateau regime with an average renormalisation factor of about $f_{ren} \approx 1.5$ in

this scenario. But it has to be stated that such a scaling is very sensitive to changes in collisionality once the plateau regime is left.

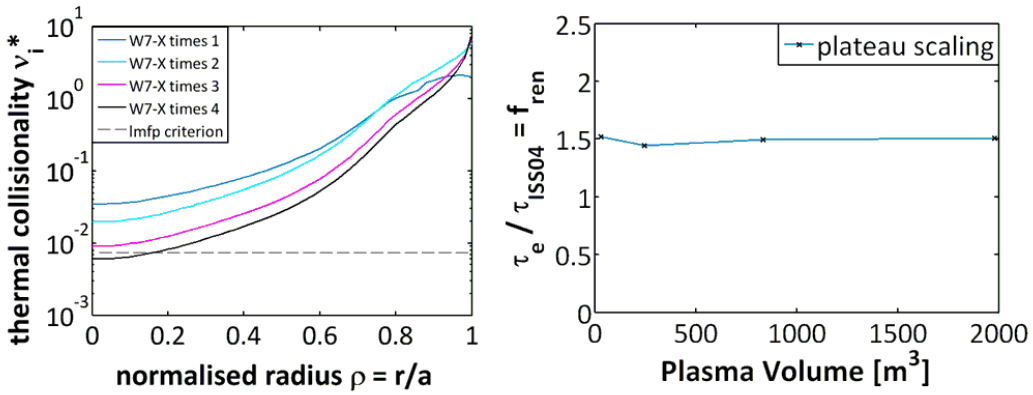

Figure 4.9: Thermal collisionalities of plateau scaling using high density and low heating power for different sizes of W7-X with dashed line being lmfp-transition criterion for the standard configuration (left) and resulting renormalisation factor (right).

In summary, this section was dedicated to investigate the differences between the τ_E predicted by ISS04 scaling and that resulting from 1-D modelling. In the dimensionless parameter space, β was held constant and the change of the normalised gyroradius ρ^* was small compared to the change of the collisionality ν^*. In this context it was shown that a change in collisionality involves a change of transport regime which has large impact on the confinement scaling. And although the used parameters of the 'W7-X times 4' case in this section did not yet have relevant reactor parameters, the sensitivity of the results to important variables was highlighted.

4.2.4 Analytical Evaluation of τ_E and f_{ren}

Following the procedure of the last subsection, a semi-analytical evaluation of f_{ren} can be done for all transport regimes. Starting form a global scaling approach, the heating power of the plasma P must be compensated by the total energy flux $P \sim Q$. Taking the flux equations (4.5) and neglecting gradient lengths $\nabla n/n$, $\nabla T/T$ and E_r/T the energy flux Q may be approximated by $Q \sim n\,T\,D_{11}$ [68]. The analytical expressions for the different transport regimes, equation (2.52), must be expressed in terms of temperature, density and magnetic field $D_{11} = D_{11}(n, T, B)$. Combining this with the energy flux Q yields an expression for the temperature $T = f(n, P, B)$ essentially allowing to write the confinement time scaling and renormalisation factor in the form of

$$\tau_E \sim \frac{n\,T}{P} \quad \sim \quad f_1(n, P, B), \tag{4.13}$$

$$f_{ren} = \frac{\tau_E}{\tau_E^{ISS04}} \quad \sim \quad f_2(n, P, B). \tag{4.14}$$

This analysis was carefully carried out for all important transport regimes and the results are summarised in table 4.3.

As mentioned above, during one simulation scan, density n, magnetic field strength B and β were kept constant while only varying the heating power P. Therefore it is only necessary to compare the heating power dependence of the simulations with the analytic scaling. The last section demonstrated the agreement of the analytic scaling of the plateau regime with corresponding simulations, see figure 4.9. Now it is argued whether the decaying renormalisation factor of the simulations with constant β, figure 4.5, can be explained.

The scaling of the $\sqrt{\nu}$ regime is not relevant for the constant β case, because an entire plasma can only be under very special circumstances in the $\sqrt{\nu}$ regime, namely if a sufficiently strong electric field is present that both the ion and electron distribution functions are to a large degree in the $\sqrt{\nu}$ regime. This leaves only the $1/\nu$ regime and the anomalous transport as possible candidates for decreasing renormalisation factor in the constant β scaling. As is visible from table 4.3, both $1/\nu$ and anomalous scaling show a decreasing behaviour for the renormalisation factor with increasing heating power. It is therefore reasonable that the so far observed decreasing renormalisation factor is mainly due to the exponential relations of the $1/\nu$ regime and the anomalous transport.

As an example the scenario of low density and high magnetic field strength shall be compared with the analytic scaling of the $1/\nu$ regime.

From the left side of figure 4.10 it can be concluded, that for this scenario both electrons and ions are well in the lmfp region with the electron energy flux dominating in all cases. Therefore the analytic $1/\nu$ scaling, normalised to f_{ren}, can be compared with the behaviour of the 1-D simulation results. This is shown on the right side of figure 4.10 demonstrating a surprisingly good agreement.

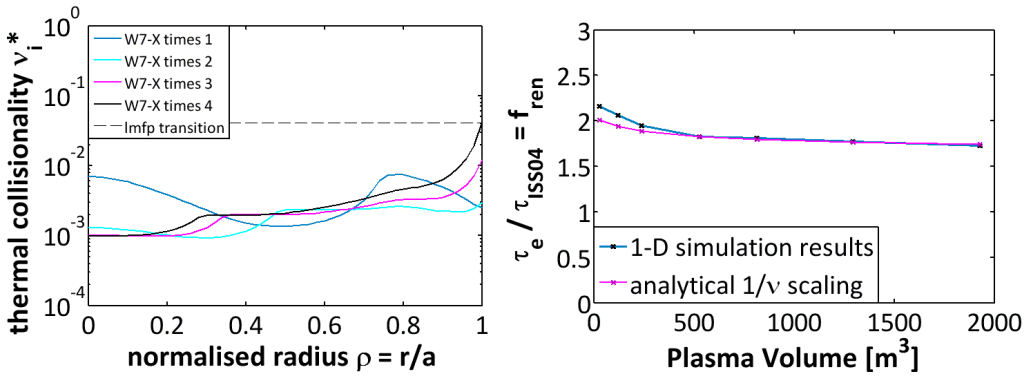

Figure 4.10: Thermal collisionalities of the low density and high magnetic field scenario with corresponding lmfp transition criterion (left) and comparison of the renormalisation factor of the 1-D simulations with the results from the analytical $1/\nu$ approach (right).

Regime	$D_{11}(n, P, B)$	$\tau_E \sim f_1$	$f_{ren} \sim f_2$
$1/\nu$	$\frac{T^{7/2}}{n\,B^2}$	$\frac{n\,B^{4/9}}{P^{7/9}}$	$n^{0.46}\,P^{-0.17}\,B^{-0.4}$
$\sqrt{\nu}$	$\frac{n^{1/2}}{T^{1/4}\,B^{1/2}}$	$\frac{P^{1/3}\,B^{2/3}}{n}$	$n^{-1.54}\,P^{0.94}\,B^{-0.17}$
Plateau	$\frac{T^{3/2}}{B^2}$	$\frac{n^{3/5}\,B^{4/5}}{P^{3/5}}$	$n^{0.06}\,P^{0.01}\,B^{-0.04}$
Dominating anomalous transport	const.	$\frac{n}{P}$	$n^{0.46}\,P^{-0.39}$
Fusion anomalous transport	$\frac{P^{3/4}}{n}$	$\frac{n}{P^{3/4}}$	$n^{0.46}\,P^{-0.14}$

Table 4.3: Summary of confinement time and renormalisation factor proportionalities for density, magnetic field strength and heating power as calculated from analytic theory for the transport regimes of neoclassical theory ($1/\nu$, $\sqrt{\nu}$ and plateau-regime) as well as a hypothetical dominating anomalous transport model ($D_{ano} = \text{const.}$) and the anomalous transport model introduced for the later used fusion calculations ($D_{ano} \sim P^{3/4}/n$) [5].

4.3 Physic issues

So far general scaling simulations were carried out with the investigation of the corresponding transport regimes and their scaling behaviour. With this background some specific physical issues of interest shall be investigated in the following. The influence of the shape of the density profile and in relation to that the impact of edge density gradient lengths. Also the critical gradient model of the anomalous transport shall be tested in reference to typical Tokamak behaviour.

4.3.1 Hollow density profile

In the course of the experimental campaign of LHD strongly hollow density profiles were observed. Additionally slightly hollow density profiles were already seen in the Stellarator W7-AS [44]. Therefore it is a relevant consideration to use the predictive code to investigate the effect of hollow density profiles on the performance of W7-X and upscaled devices.

The basic difference to the flat density profile used so far is a positive density gradient in the core acting on the particle and energy fluxes. A density profile with such a positive gradient $\nabla n > 0$ in the core is called *hollow*. Such a hollow density profile, as seen in LHD, was therefore selected from the International Stellarator-Heliotron Profile Database [6, 69] and fitted to remove the experimental scattering, see left side of figure 4.11. The resulting model profile, as seen on the right side of figure 4.11, is from here on used for all hollow density profile scenarios.

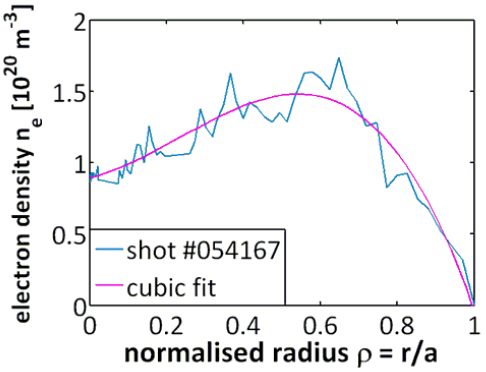

Figure 4.11: LHD hollow density profile (shot #054167 [6, 69, 70], blue) with corresponding fit to remove experimental scatter (magenta).

To achieve results comparable with the previous calculations, all input parameters were chosen to be as in the low density, low magnetic field scenario from subsection 4.2.2 and in addition the hollow density profile was scaled to arrive at the same volume averaged density. With that ensemble of input parameters a scaling study was performed and the volume averaged β and confinement time τ_E are compared between the low density, low magnetic field scenario and the corresponding hollow density profile scenario in figure 4.12. The figure shows, that the volume averaged β of the hollow profile scenario is only slightly smaller than the β of the flat profile scenario. The same applies for the confinement time, meaning that both profiles lead to a similar performance under the used input parameters.

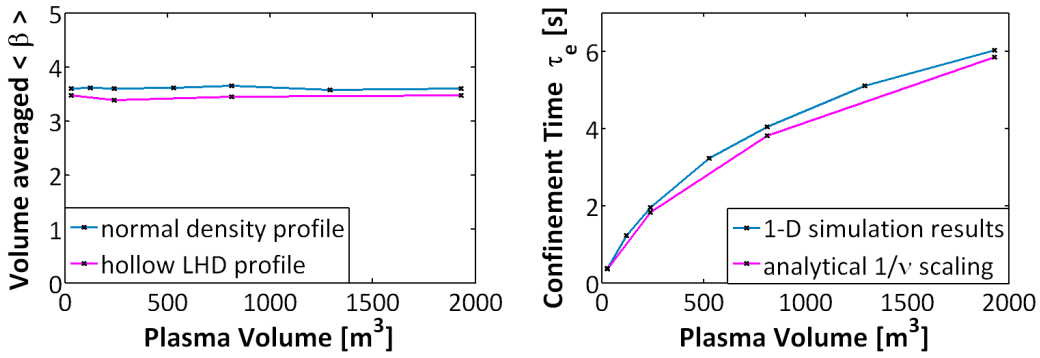

Figure 4.12: Comparison of volume averaged β (left) and confinement time τ_E (right) between hollow and standard density profile for $B_0 = 2.38\text{T}$, $n_{e,vol} = 0.98 \cdot 10^{20}$ m^{-3} and same heating powers.

The most significant difference arising from a hollow density profile, however, is a positive electric field in the core region of the plasma which was observed in all simulations with hollow density profile. This is reflected in figure 4.13 where the flat density profile and the hollow profile are shown on the left side for the equivalent low density, low magnetic field scenario for the 'W7-X times 3' case. On the right side of this figure, the corresponding electric fields are shown. It is visible, that the electric field of the flat density profile is everywhere negative which is the usual case for flat density profiles with $T_i \sim T_e$. In contrast to that, the electric field of the hollow profile shows a clear positive behaviour in the core region where also the positive gradient of density profile is located. Although figure 4.13 is just an example, the positive electric field in the core has been observed for all cases with hollow density profile.

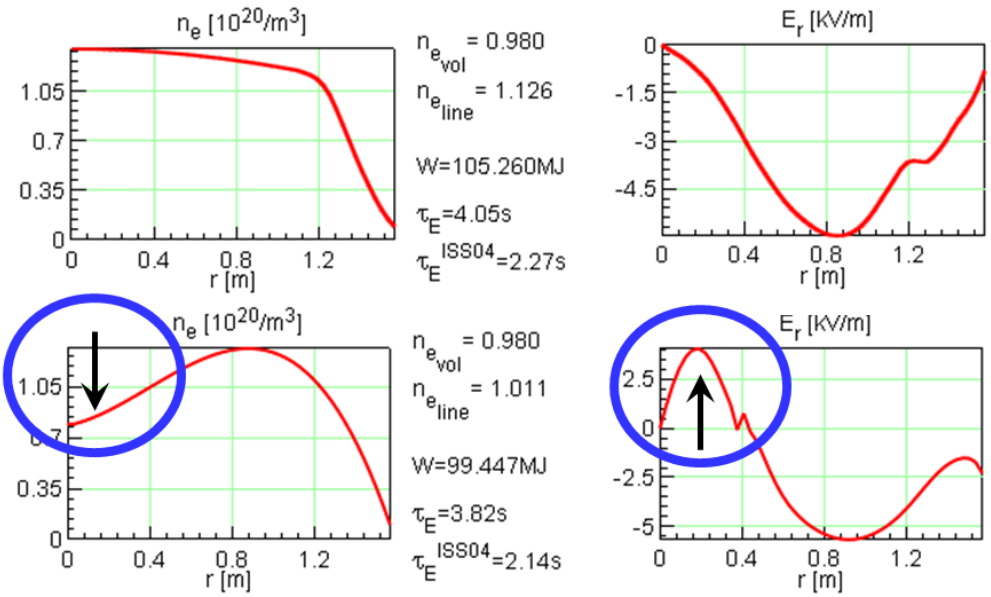

Figure 4.13: Flat density profile (upper left) and the corresponding electric field (upper right) as well as hollow density profile with positive gradient in the core (bottom left) and the resulting electric field with $E_r > 0$ in the core region (bottom right) for low density, low magnetic field scenario of 'W7-X times 3'.

This effect was already observed in W7-AS [71] and because it is in general assumed that the plasma core of a Stellarator is dominated by neoclassical transport, it is possible to estimate the electric field with the neoclassical ambipolarity condition (2.31). Because of the strong impact of the electric field on diffusion, the radial profiles are split into two regions defined by $E_r < 0$ and by $E_r > 0$.

In the case of negative E_r the approximation $D^i_{jk} >> D^e_{jk}$ can be made [42]. Taking the ambipolarity constraint $\Gamma_e = Z\Gamma_i$ and inserting in it the approximation with $n_e = n_i = n$, one arrives for $E_r = 0$ at the criterion

$$\frac{n'}{n} = -\delta^i_{12}\frac{T'_i}{T_i} \tag{4.15}$$

with $\delta^i_{12} = D^i_{12}/D^i_{11}$ being a fixed number in analytic theory of a pure transport regime.

It follows from this criterion that the formation of a positive electric field is dependent on the density and temperature gradient lengths. If the ratio of the density gradient length to the temperature gradient length is larger than

Regime	$1/\nu$	$\sqrt{\nu}$	ν	plateau	banana
δ^i_{12}	7/2	5/4	1/2	3/2	-1/2

Table 4.4: $\delta^i_{12} = D^i_{12}/D^i_{11}$ as predicted by analytic theory [42].

the corresponding delta value of the regime,

$$\left|\left(\frac{\nabla n}{n}\right)\right| / \left|\left(\frac{\nabla T_i}{T_i}\right)\right| > \delta^i_{12}, \tag{4.16}$$

a positive electric field appears.

The physics mechanism leading to a positive E_r is more complicated. The simulations have shown, that the value of $\delta^i_{12} < 1$. This indicates that the ion distribution function is not only in the $\sqrt{\nu}$-regime. Analytic theory [42] predicts $\delta^i_{12} = 5/4$ for the $\sqrt{\nu}$-regime. But there are only two regimes allowing δ^i_{12} to get smaller than one; the ν-regime and the 'banana'-regime with $\delta^i_{12} = 1/2$ and $\delta^i_{12} = -1/2$ respectively. For the high-mirror configuration used here, the DKES results did not show any indication of a ν-regime which therefore should not occur in a simulation [71]. The strong E-field suppresses the $\sqrt{\nu}$-regime and the transport is caused by the ions in the plateau- and 'banana'-regime, for an illustration see figure 2.4 in subsection 2.3.3. The electrons on the other hand are partly in the $1/\nu$-regime and due to the strong electric field partly in the $\sqrt{\nu}$-regime with $\delta^e_{12} \approx 5/4 \ldots 7/2$. Therefore a discrepancy arises in the diffusion coefficients with $D^i_{11} \geq D^e_{11}$, but more importantly $D^i_{12} \leq D^e_{12}$. Inserting these results in the ambipolarity constraint, a very rough estimation makes the resulting positive electric field obvious.

$$\frac{n'}{n} - \delta^e_{12}\frac{T'_e}{T_e} = \frac{eE_r}{T_e} > 0 \tag{4.17}$$

This effect indicates a problem for W7-X. Without central refuelling sources, like pellet injection, hollow density profiles could develop [42]. This could lead to a high density accumulation off-axis which would exceed the cutoff-density of the ECRH. The plasma could not be heated anymore leading to positive pressure gradients in the plasma core which are intrinsically MHD-instable.

On the other hand, if good plasma density control can be achieved, hollow density profile can even be used for favourable plasma scenarios. The positive electric field leads to favourable impurity transport out of the plasma core. Moreover, in a fusion reactor the helium ash could be transported outward in a controlled way. This discussion shows the importance of density control in a fusion device and gives reason to investigate this issue experimentally, e.g. in W7-X.

4.3.2 Constant edge density gradients

One problem while upscaling a Stellarator is the uncertainty of the density profile form. In an upscaling, the density profile can generally be treated in two different ways. Either the form of the profile is kept constant ($n(\rho) = const.$) which was done so far or the density gradient length is assumed to be constant ($L_n = const$).

$$L_n^{-1} = \frac{\nabla n(r)}{n(r)} = const. \tag{4.18}$$

This second method may be justified by atom physics which indicates, that the density gradient at the edge of the plasma is governed by the penetration depth of the recycling neutrals [56]. To investigate the impact of this assumption, a scaling was performed using constant density gradient lengths in the low density, low magnetic field scenario. The reference gradient length is here the flat standard profile as seen on the left side of figure 4.14. The right side of this figure shows the density profile for the 'W7-X times 4' case with the same gradient length as in the standard profile.

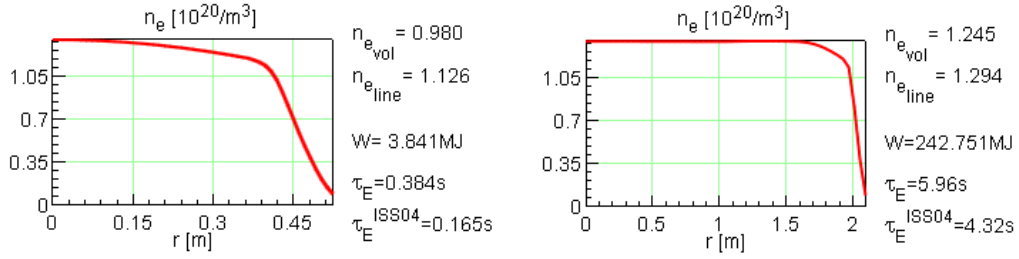

Figure 4.14: Normalised standard profile for 'W7-X times 1' (left) and modified profile with the same gradient length for 'W7-X times 4' (right) for high mirror configuration with $B_0 = 2.38$T, $n_0 = 1.35 \cdot 10^{20}$ m^{-3} and same heating powers as in the low density, low magnetic field case.

The difference between the flat standard profile and the profile with constant gradient length becomes clear if directly compared. This can be seen in figure 4.15 where on the left side the standard profile is accompanied by the modified profile for the case of 'W7-X times 3'. The modified profile is steeper at the edge and the mean density is higher. This behaviour is reflected in the plasma performance as the volume averaged β of the profile with constant edge density gradient is slightly higher compared with the normal density profile seen on the right side of figure 4.15.

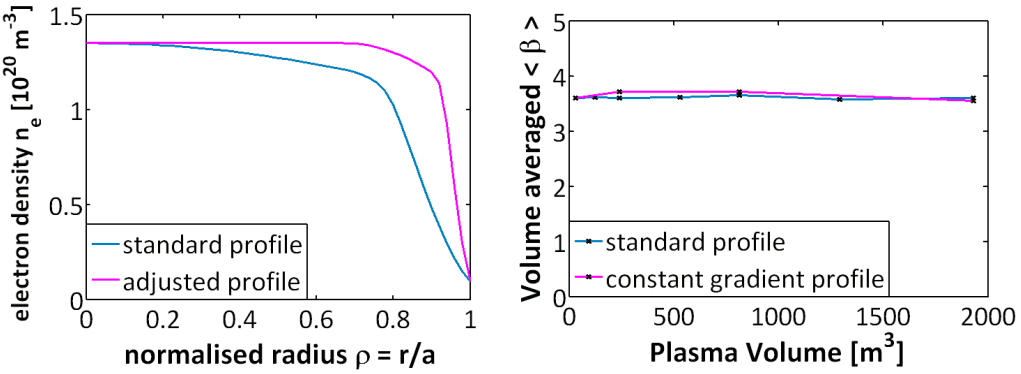

Figure 4.15: Comparison of the standard profile used so far (blue) with the modified profile with constant density gradient length (magenta) for the 'W7-X times 3' case (left) and volume averaged β for the whole scaling (right).

As the plasma performance is only marginally higher, the performance of both cases can be regarded as similar. As the anomalous transport is lower at the edge due to the assumed $1/n$-scaling behaviour and the neoclassical transport decreases too due to the higher density, these effects could be relevant for plasma edge modelling and should be included in refuelling scenarios but are only of minor interest for the overall plasma confinement and performance.

4.3.3 Critical gradient model

As already discussed in subsection 2.4.1, the ion-temperature-gradient instability is assumed to produce strong turbulence. Analytical parametrisation of numerical results [23] leads to high transport once the stability criterion is violated. Because the criterion has the form of a critical ion temperature gradient length

$$\frac{R}{L_T} = R\frac{\nabla T}{T} > c, \tag{4.19}$$

such a model forces the ion temperature profile to stay at this critical value. Therefore this description is known as *critical gradient model* [72]. Experimental results from Tokamaks show many characteristics connected with this model like profile stiffness and a strong link between central and pedestal temperature [73]. This kind of behaviour was not yet seen in Stellarators but such a model can be chosen in the 1-D code, see subsection 4.1. Since the anomalous transport is not understood, the model was applied to the W7-X case to investigate its effect. In the model, the temperature profile fluctuates around its critical gradient and therefore the model converges only very slowly to an equilibrium state. Due to the long calculation times only two cases were selected as example. Namely 'W7-X times 1' and 'W7-X times 4', both with parameters from the low density, low magnetic field scenario and with $a_{crit} = \frac{1}{A} \cdot \frac{R}{L_{Ti}} = 1$ and 4 respectively using the aspect ratio $A = R/a$.

As can be seen on the left side of figure 4.16, the temperature of the ions has only a small gradient and is high at the edge for the 'W7-X times 1' case. The right side shows the temperature profiles for the 'W7-X times 4' case. Both cases are presented with the corresponding temperature profiles of the anomalous $1/n$-model. The ITG simulations have a lower temperature compared to the $1/n$ cases presumably related to the higher anomalous heat flux.

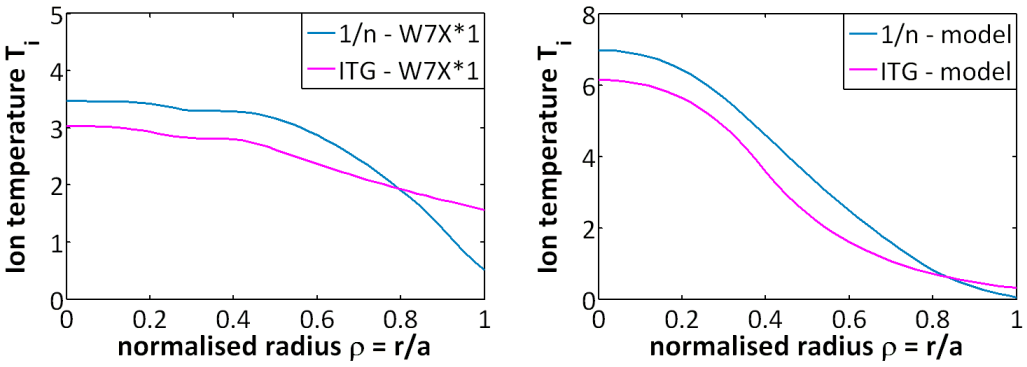

Figure 4.16: Temperature profiles for the anomalous critical gradient model for 'W7-X times 1' with $a_{crit} = 1$ (left) and for 'W7-X times 4' with $a_{crit} = 4$ (right) for high mirror configuration with $B_0 = 2.38$T, $\bar{n}_e = 1.13 \cdot 10^{20}$ m^{-3} and same heating powers as in the low density, low magnetic field scenario which is also shown as comparison.

As stated, once the temperature gradient exceeds the critical value, strong anomalous transport is expected to govern the heat flux. Assuming gyro-

Bohm scaling of the transport [49], $\chi \propto T^{3/2} f\left(\frac{R}{L_T}\right)$ with the critical function $f(R/L_T)$, the heat flux may be estimated to

$$Q_i = \chi n \nabla T \propto n T^{5/2} f\left(\frac{R}{L_T}\right) \tag{4.20}$$

for the ions [73]. The critical behaviour for the ITG cases can clearly be seen in figure 4.17, where the heat flux increases sharply once reaching the critical gradient $R/L_{Ti}|_{crit}$. The degree of profile stiffness is given by the slope of $Q/T^{5/2}$ above $R/L_{Ti}|_{crit}$ [73]. As the slope is very steep, the figure represents a strong profile stiffness for the ITG cases. This is in contrast to the $1/n$ model which shows a non-critical continuous behaviour over the radial profile.

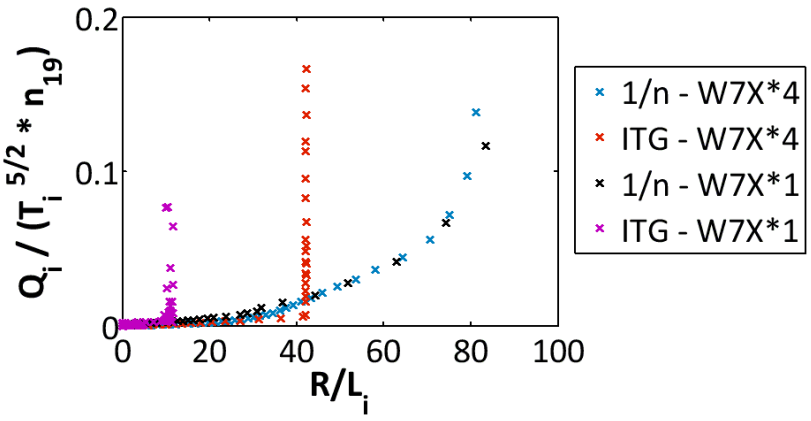

Figure 4.17: Variation of $Q_i/(T_i^{5/2}n)$ as function of R/L_{Ti} over the radial profile for the cases of 'W7-X times 1' with $a_{crit} = 1$ and 'W7-X times 4' with $a_{crit} = 4$ for low density, low magnetic field scenario parameters with the corresponding $1/n$ cases.

It can be summarised that the critical gradient model is very well able to incorporate the idea of strong ITG turbulence and shows features seen in Tokamak experiments. But to really test the relevance of the model, experimental data and gyrokinetic simulations are required.

4.4 Scaling with self-consistent Fusion Power

So far the 1-D code was used to investigate basic plasma performance and physics issues. To assess ignition or reactor capability of an upscaled W7-X, the 1-D code was expanded to account for self-consistent fusion power [5, 58].

In this context the anomalous transport model was modified [5, 58] to

$$D_{ano} = c \cdot P^{0.75} \cdot \frac{n(a)}{n} \tag{4.21}$$

in order to scale with the arising large heating power P (external and α-heating)[4].

As in the scalings before, β was kept at around 3.6% while only varying the heating power. But this holds only for non-ignited cases. After ignition the plasma will build a self-consistent equilibrium heated by the alpha particles. The operation point could be controlled by density and magnetic field but this issue was not investigated here. In this section two scenarios were studied, a conservative approach and an advanced scenario, see table 4.5. In this context, conservative and advanced are related to technological capabilities. For the conservative case a moderate magnetic field strength on axis of 4.5 T was choosen which could be realised in near-term by NbTi technology. Also moderate values were selected for the deuterium and tritium density leading to less fusion power and therefore to moderate heat flux on divertor and first wall reducing requirements for the material used in those components. The advanced case in contrast assumes technological progress, namely the use of Nb_3Sn or Nb_3Al superconductors with 5.5 T magnetic field strength on axis. Also the density was choosen to be higher. For both cases the high mirror configuration was used which is necessary to confine the alpha particles long enough to heat the plasma.

Property	Conservative	Advanced
B_0 [T]	4.5	5.5
n_{D0} [10^{20} m^{-3}]	0.87	1.38
n_{T0} [10^{20} m^{-3}]	0.93	1.47

Table 4.5: Parameters chosen for the conservative and advanced scenario.

With these input parameters the scaling was performed and the resulting volume averaged β can be seen on the left side of figure 4.18. At first β was chosen to be around 3.6 % but without further density and magnetic field variation the heating power by the alpha particles leads to an increasing β value up to 6 % for the maximal size. It can also be seen that the β of

[4]This anomalous transport model will later be called 'constant-in-centre model (cc)'.

the advanced scenario increases strongly at small sizes which is related to the higher density and the higher alpha particle heating. On the right side of figure 4.18 the renormalisation factor is illustrated for both cases. Both showing a decreasing behaviour which is due to the exponential relations of the $1/\nu$ regime and the anomalous transport investigated in section 4.2.3. This also explains the stronger decrease of the advanced scenario which is related to the higher heating powers.

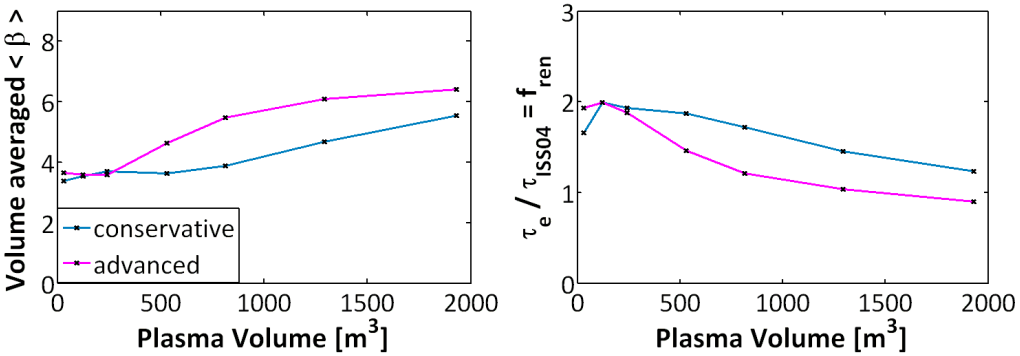

Figure 4.18: Self-consistent fusion power upscaling and resulting volume averaged β (left) and renormalisation factor (right) for the conservative and advanced scenario.

The higher fusion power and therefore higher alpha particle heating is quantified on the left side of figure 4.19. It can be seen that the higher density and the higher magnetic field lead to a very strong increase of fusion power compared with the conservative scenario. This was also found in the 0-D scaling studies (compare figure 3.4) and therefore confirms this behaviour. The right side of figure 4.19 shows the corresponding fusion gain Q. The lines in this graph stop at the point where ignition starts ($Q = \infty$). Therefore a step from conservative to advanced assumptions would reduce the necessary reactor size from 22 m to 16 m. The space gained could at least be used for relaxing the space requirements of shield and wall. For an ITER-like Stellarator with $Q = 10$, the size would be reduced in the same manner from roughly 15 m to 10 m when going from conservative to advanced assumptions.

The standard Lawson-Criterion states that a plasma must exceed a critical value of $nT\tau_E$ to achieve ignition. With standard parameters this ignition condition is usually formulated by

$$nT\tau_E \geq 3 \cdot 10^{21} \mathrm{m}^{-3}\ \mathrm{keV}. \tag{4.22}$$

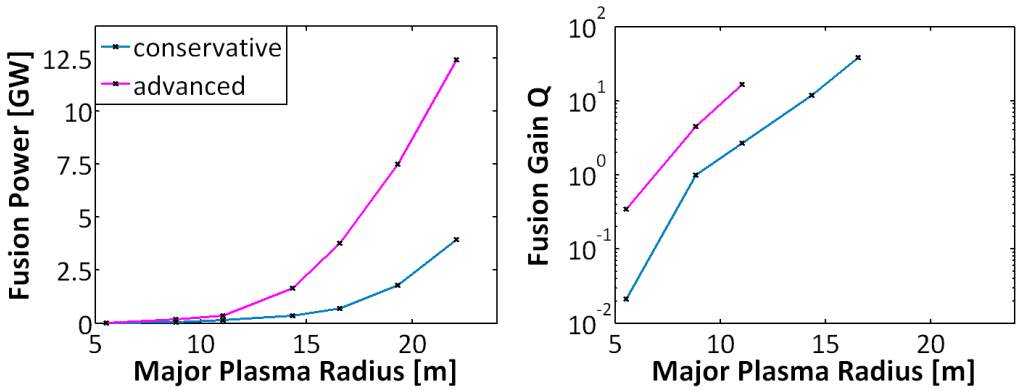

Figure 4.19: Self-consistent fusion power (left) and fusion gain (right) for the conservative and advanced scenario.

The criterion is represented by a curve using density and temperature profiles and 0-D scaling laws. This was done for the HSR4 reactor parameters and is shown in figure 4.20. The $nT\tau_E$ values for the conservative and advanced scenario of the simulations are also shown and comply with the Lawson curve for the ignited cases. In the range between $6 \ldots 7$ keV the value of $nT\tau_E$ increases sharply while the ion temperature changes only to a small degree. The cases in this range have similar density, temperature and heating powers with the volume being the only major changing parameter. The increase of the volume leads in those cases to a strong increase of confinement time explaining the increase of $nT\tau_E$. Additionally, possible operation points of W7-X, ITER and DEMO are shown in the figure for comparison.

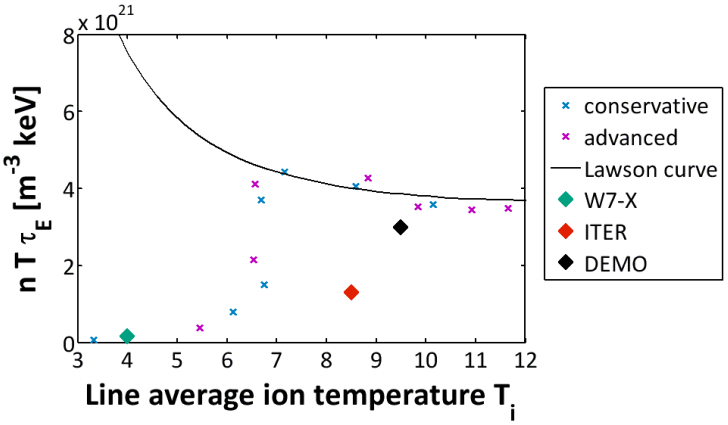

Figure 4.20: Tripple-product of conservative and advanced scenario with Lawson ignition curve for HSR4 parameters using ISS04 scaling (black line) and possible operation points of W7-X (green), ITER (red) and DEMO (black).

4.4.1 Reactor transport regime

The tools which were used to investigate the difference between ISS04 and 1-D scaling can now be applied to the case of self-consistent fusion power to characterise the transport in a fusion reactor [58].

At first the energy flux of the ions and electrons shall be compared. This is done on the left side of figure 4.21, where the heat flux relation Q_i/Q_e is plotted for the conservative scenario for different sizes. It can be seen that for the 'W7-X times 1' case the electron heat flux is dominating the plasma. But as the size of the device is increased the ion heat flux is increasing in relation to the electron heat flux, which was also seen in the simulations without self-consistent fusion (cf. figure 4.6). Finally in the 'W7-X times 4' case the ion and electron heat flux have nearly the same amount (black line) with $Q_i/Q_e \approx 1$ which is presumably related to the anomalous transport. Therefore on the right side of figure 4.21 the ratio between anomalous and neoclassical heat flux Q_{ano}/Q_{neo} is shown. It can be seen that in the 'W7-X times 1' and 'W7-X times 2' cases, the neoclassical heat flux is strongly dominating but the anomalous heat flux is increasing with size due to the coupling of the anomalous transport model to the heating power ($D_{ano} \sim P^{3/4}$). In the 'W7-X times 4' case the anomalous heat flux is dominating from the half radius to the edge. As the anomalous diffusion coefficients are in the model the same for both electrons and ions it is reasonable that this leads to the equal ion and electron heat flux in the 'W7-X times 4' case. It is unclear, whether this amount of anomalous transport is reasonable, since the real relation of anomalous to neoclassical fluxes is unknown.

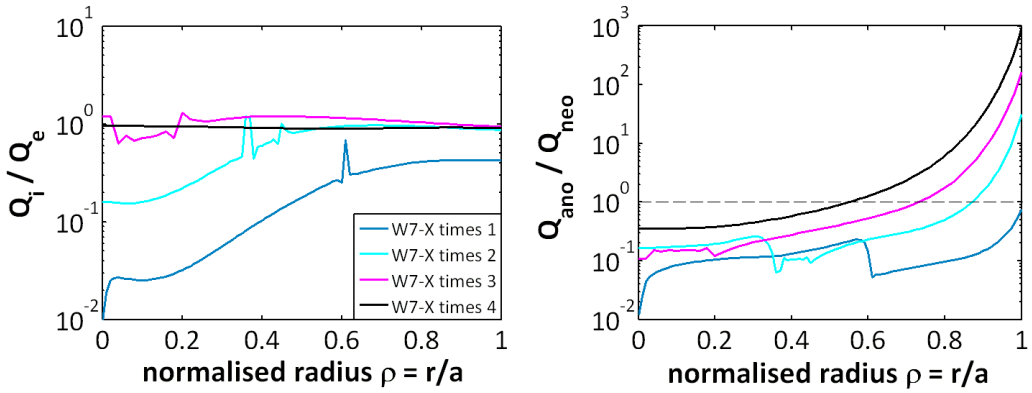

Figure 4.21: Ratio of ion to electron heat flux (left) and anomalous to neoclassical heat flux (right) for the conservative scenario.

At the beginning of this chapter the importance of the collisionality for transport regimes was demonstrated. Therefore in figure 4.22 the collisionality is plotted for different sizes of the conservative (left) and advanced scenario (right). It is clearly evident from the figure that in both scenarios the collisionality of the ions is well below the lmfp-transition criterion which means that the electron distribution function is predominantly in the $1/\nu$ regime while the largest fraction of the ion distribution function is in the $\sqrt{\nu}$ regime.

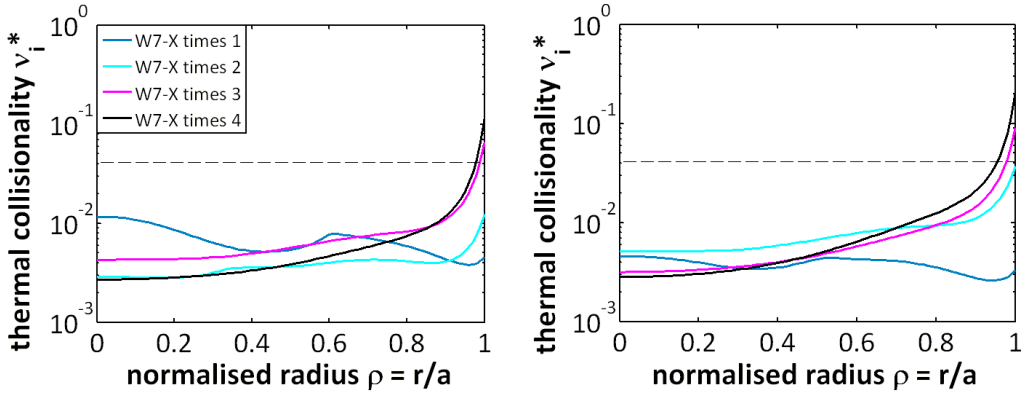

Figure 4.22: Thermal collisionality of ions for the conservative scenario (left) and advanced scenario (right) and dashed line being the lmfp-transition criterion.

Discussing the decreasing renormalisation factor as in subsection 4.2.4, the analytical $1/\nu$ scaling is compared with the results from the self-consistent fusion calculations in figure 4.23. The analytic scaling is again in good accordance with the 1-D simulation results, except for the 'W7-X times 1' cases. In those cases a too high heating power was chosen, which in the small volume heated only the electrons leading to a strong positive electric field (electron-root). Following that the whole plasma was in the $\sqrt{\nu}$ regime explaining the deviation. As the exponential relations of the analytic scalings for the $1/\nu$ regime and for the anomalous transport model in the fusion calculations are nearly the same, see table 4.3, it is not clear whether the behaviour seen in figure 4.23 is due to the neoclassical or anomalous transport.

Despite the $1/\nu$ transport and its unfavourable temperature dependence and the additional anomalous transport all the reactor relevant scenarios of the last subsection were in an ignited state. This result should be regarded as positive meaning that even under conservative assumptions with high transport the magnetic configuration of W7-X shows reactor capabilities.

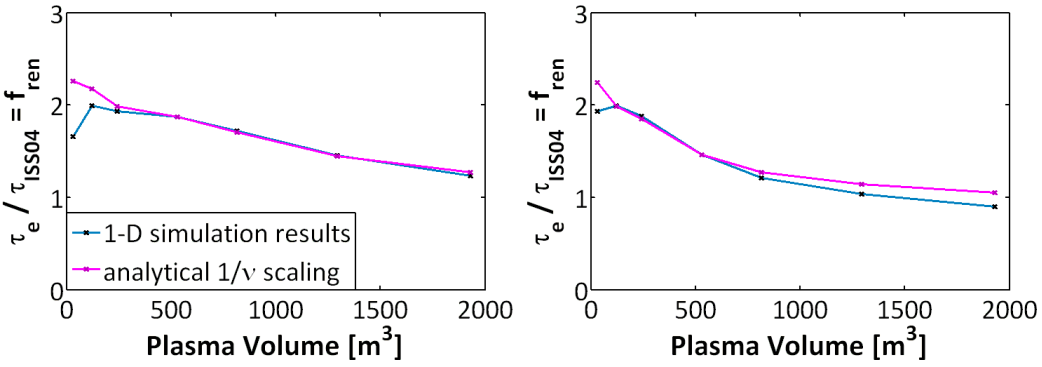

Figure 4.23: Renormalisation factor as calculated by 1-D simulations and by the analytic scaling for the conservative (left) and advanced scenario (right).

4.4.2 Impact of hollow density profile on fusion

The general effect of a hollow density profile on W7-X was investigated in subsection 4.3.1 without fusion reactions. The described hollow LHD profile is now used with self-consistent fusion heating to check the implications in the 'W7-X times 4' case of the conservative scenario. The deuterium and tritium density were fixed assuming sufficient density control. The code calculates the resulting α-particles and electron density, which is shown on the left side of figure 4.24. The resulting temperature profiles are shown on the right side of the figure. It can be seen that both the electron and ion temperature profiles have moderate gradients in the centre but a strong gradient at the edge.

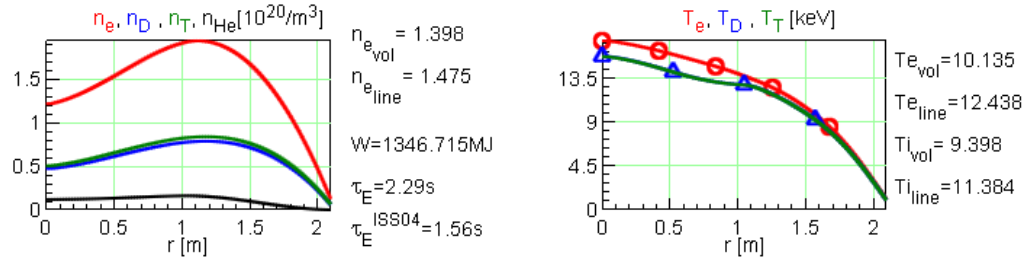

Figure 4.24: Hollow LHD density profile for deuterium and tritium and resulting electron and alpha particle density profile (left) and resulting temperature profiles (right) for the 'W7-X times 4' case of the conservative scenario.

The simulations confirm that such a hollow profile leads again to a positive electric field in the core region of the plasma, as seen on the left side of figure 4.25. Because the positive electric field is comparably small, it leads to very

high ion diffusion coefficients since the larger fraction of the ion distribution function is in the $\sqrt{\nu}$-regime and therefore strongly affected by a small positive electric field ($D_{\sqrt{\nu}} \propto E_r^{-3/2}$). Additionally it can be seen on the left side of the figure, that due to the strong positive density gradient in the core region and the relatively flat temperature profile, a positive pressure gradient arises in the plasma centre ($\nabla\beta > 0$). This positive gradient is MHD instable and would lead to a reduction of the pressure gradient through instabilities. Effectively, this corresponds to a reduction of the density gradient. Therefore such strong density gradients may not arise in fusion reactors and is subject to further investigation.

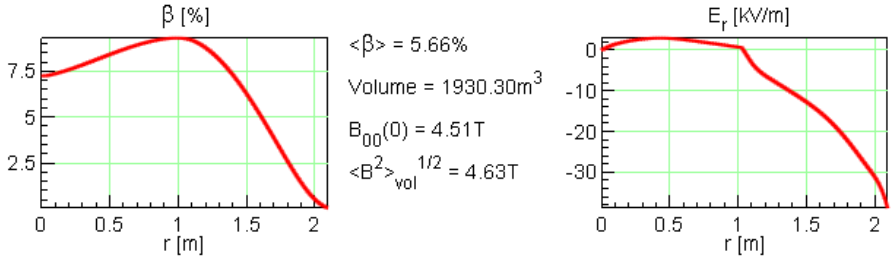

Figure 4.25: β profile (equivalent to pressure profile) (left) and electric field (right) for the 'W7-X times 4' case with LHD hollow density profile and conservative scenario parameters.

4.4.3 Performance comparison

It was highlighted in section 4.3.1 that the density profile form has great impact on the radial electric field and therefore on the plasma. The last subsection, however, indicated that strong positive density gradients may not arise in fusion reactors, nonetheless shall the hollow profile be used in the following for a comparative performance study. Throughout this work it arose under different aspects, that only few is known about anomalous transport in Stellarators. Therefore this section is to give a compact comparison between flat and hollow profiles and between two anomalous transport models, namely between the $1/n$-edge model ($D_{ano} \sim 1/n$) and the constant-in-centre (cc) model ($D_{ano} \sim P^{3/4}/n$). The used hollow and flat density profiles can be seen in the upper part of figure 4.26. The black lines in the lower part of the figure illustrate the behaviour of the anomalous diffusion coefficients of the corresponding models. All scenarios were normalised to the volume averaged electron density $n_{e,vol} =$

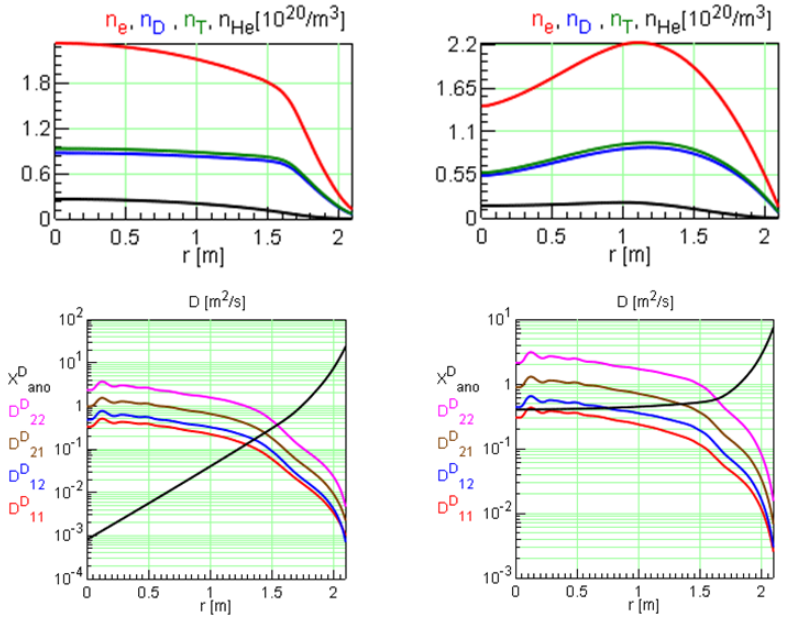

Figure 4.26: Illustration of input parameters used for performance comparison, namely flat density profile (upper left), hollow density profile (upper right), anomalous diffusion coefficients of $1/n$-edge transport model (black line - bottom left) as well as constant-in-centre (cc) transport model (black line - bottom right). (The plots are examples of different transport simulations and shall schematically demonstrate the behaviour of the diffusion coefficients and the density profiles)

$1.6 \cdot 10^{20}$ m^{-3} with a magnetic field strength of $B_t = 5$ T on the axis.

The left side of figure 4.27 shows the fusion power output of the different scenarios discussed above. The fusion power is for the cases with flat density profile higher than for those with hollow density profile. This is due to the lower density of the hollow profile in the core region. As all cases were normalised to the same volume averaged density, the core density of the hollow profiles is smaller than the density of the flat profiles. This lack of density leads therefore to the observed smaller fusion power. This evidently has also an impact on the fusion gain, shown on the right side of figure 4.27. As the external heating was the same for all cases of the same size, those simulations with hollow density must also have a smaller fusion gain. This means additionally that the scenarios with hollow profiles achieve ignition at larger radii compared with the flat density profiles. Therefore the profiles with flat density profile have a higher reactor performance in those cases. It must be added that impurities

were not taken into account in the simulations.

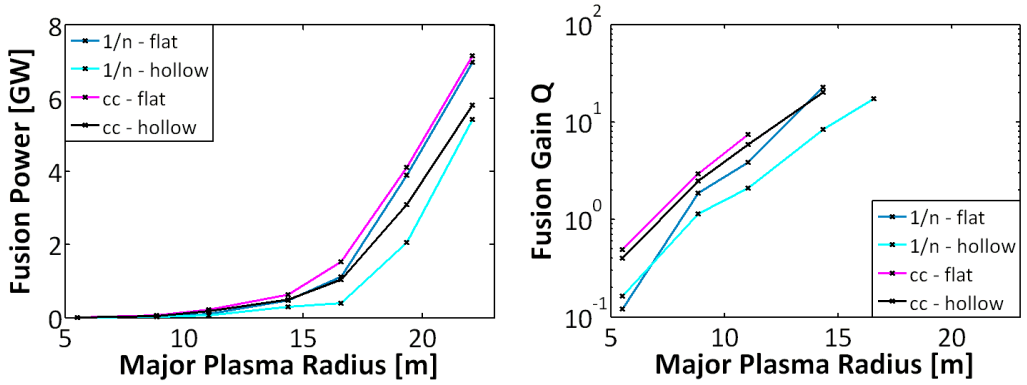

Figure 4.27: Fusion power (left) and fusion gain (right) for cases with hollow and flat density profile, all normalised to the volume averaged electron density $n_{e,vol} = 1.6 \cdot 10^{20}$ m^{-3} and $B_t = 5$ T with additional $1/n$-edge and constant-in-centre (cc) anomalous transport.

Following the above argumentation the different β values of the left side of figure 4.28 can be explained. The lower fusion power of the cases with hollow profiles leads consequently to less alpha heating power and therefore to smaller temperatures. This influences directly the plasma β leading to smaller values compared with the flat density scenarios. It seems also that the $1/n$-edge model decreases β for small reactor sizes while this effect cannot be seen for large reactor sizes. The right side of figure 4.28 now emphasises

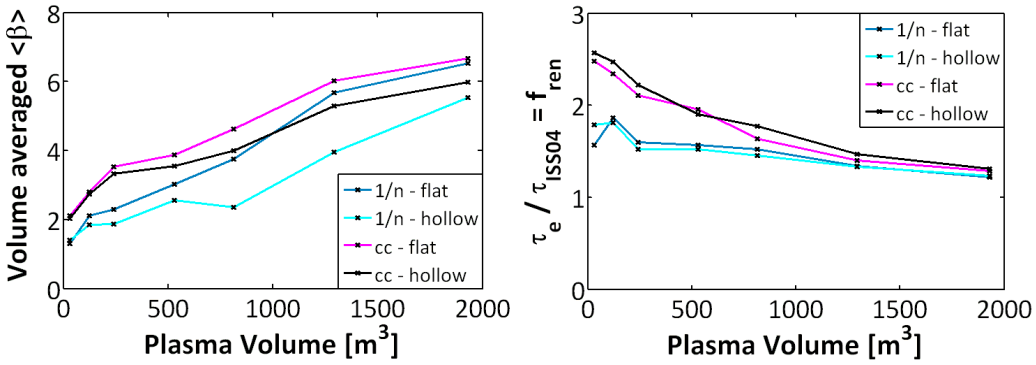

Figure 4.28: Plasma β (left) and renormalisation factor (right) for the scenarios of hollow and flat density profile form with $1/n$-edge and constant-in-centre anomalous transport.

this difference between the two anomalous transport models. The constant-in-centre model is by definition such, that it scales with the overall heating

power $D_{ano} \sim P^{3/4}$ leading to very low anomalous transport for small reactor sizes where only a small amount of fusion power takes place. The $1/n$-edge model on the other hand employs its full effect already on small sizes leading to high anomalous transport and therefore to lower confinement times and renormalisation factors. But it is also intriguing that at larger sizes the model of anomalous transport seems to become unimportant as the renormalisation factors seem to converge to a similar value.

It can be summarised that strong hollow density profiles would lead to less fusion power performance due to the lack of density in the hot core region. This emphasises the impact of the density profile form on the simulation results. It could also be seen that the different anomalous transport models have especially an impact on small reactor sizes. But it seems that this difference is getting smaller if one goes to larger sizes. The problem of the different anomalous transport models again highlights the uncertainty of this description.

Chapter 5

Summary and Conclusions

The results obtained in this work are discussed in the following.

0-D Scaling

The first approach to perform scaling studies is to use zero dimensional approximations. Such an approach was done for Tokamaks in [3]. The basic principle used in these studies to obtain the appropriate 0-D approximations was adopted for the use of Stellarators in this thesis. Applying the the empirical ISS04 confinement time scaling, the power balance of a Stellarator reactor could be simulated. The results showed the advantage of helium cooling over water cooling concerning the net electrical power output due to the significantly higher thermal conversion efficiency of the advanced helium cooling. It could also be demonstrated that technological advancement of superconductor technology employing Nb_3Sn or Nb_3Al with 5.6 T field strength on the axis of the magnetic field would greatly increase the fusion output of a reactor. Furthermore, if magnetic configurations could additionally be optimised, higher energy confinement times would be reached. Following that, an increase of the renormalisation factor in the ISS04 scaling from 1 to 1.5 would strongly reduce the radius required for ignition from $19 \ldots 21$ m to $13 \ldots 14$ m. As the costs of a fusion reactor scale with the volume of the machine, the reduction of size is very important. Reducing the major radius by a quarter would essentially mean a cut of half in costs on the level of billions. Finally, the 0-D scalings in form of dimensionless quantities showed that the step from W7-X to DEMO would be very large suggesting that an intermediate device such as an ITER-like Stellarator could become necessary but will depend on the

results of W7-X.

Importance of 1-D Simulations

Simulations with the 1-D code [5] showed larger discrepancies to the 0-D scalings. This was especially the case for the introduced renormalisation factor $f_{ren} = \tau_E/\tau_E^{ISS04}$ which showed in all simulations a decreasing behaviour for increasing R_0. It was demonstrated that a plasma may change its transport regime throughout an upscaling. The ISS04 scaling is compliant with the collisional plateau regime while most reactor relevant simulations showed transport characteristics of the $1/\nu$ regime for the electrons and $\sqrt{\nu}$ regime for the ions. Reflecting this result and using analytic theory, it was found that the behaviour of the renormalisation factor is due to the exponential relations of the $1/\nu$ regime which showed good agreement with the simulation results.

Anomalous Transport Model

Although motivated by the W7-AS experiment, the frequently used empirical $1/n$-edge model lacks a larger physics base. Little is known about the anomalous transport expected in W7-X. Different models for the anomalous transport can be employed for the simulations, but at present none of first principles. This gives rise to the need for exploring this new physics both experimental and theoretical. The anomalous heat and particle fluxes lead to a high degree of uncertainty in the simulations.

Ion Critical Gradient Model

The plasma transport of Tokamaks is to a large degree driven by turbulence and instabilities which can lead to a critical gradient behaviour of the temperature. Although such characteristics were in Stellarators only seen for electrons so far [64], a critical gradient model for the ions was tested in the frame of the 1-D code to show its effect on W7-X profiles. Due to the long calculation times only selected cases were assessed. In these cases it could be demonstrated that the critical gradient model brings up typical Tokamak characteristics such as strong profile stiffness.

Hollow Density Profile

An experimental hollow density profile from LHD [6] was taken to asses profile effects and has been incorporated into the 1-D simulations. The investigation of such a profile for reactor conditions and its effect was carried out in this work for the first time. It was shown that such a strong hollow density profile leads to a positive radial electric field in the core region capable to draw the electron distribution function partly into the 'banana' regime and diminishing the ion transport down to the level of equivalent Tokamaks. This positive electric field due to hollow density profiles opens possibilities for discharge scenario developments which, e.g. assess the control of impurity in-flux or the exhaust of helium ashes.

Constant edge density gradients

To explore the role of edge gradients which are largely unknown, the standard profile was taken and modified to arrive at constant gradient length L_n. The comparison with the standard profile showed that the overall plasma performance in terms of τ_E and β was marginally higher due to the higher density at the edge. Therefore it could be concluded that those effects, important for plasma edge modelling, have less impact for the fusion performance.

Self-Consistent heating by fusion α's

In the final stage of this thesis an augmented version of the 1-D code [5] was used which incorporated the fusion power self-consistently. To account for the higher temperatures, fusion reactions and heating power, an anomalous transport model contributing strongly to plasma transport was chosen. Investigation of two different scenarios (conservative, advanced) showed a very strong increase of fusion power from a technologically conservative scenario to a scenario with advanced assumptions. In the conservative case, a W7-X like reactor would still need a major radius of around $R \approx 21 \ldots 22$ m while technological advancements would reduce the reactor size significantly to $R \approx 15 \ldots 16$ m. Despite the high neoclassical and anomalous transport in those cases, ignition was reached indicating a positive reactor perspective for W7-X-like magnetic configurations.

A similar conclusion can be made for an intermediate step. If the aim was to build an ITER-like Stellarator with fusion gain $Q = 10$, the advanced

scenario would require $R \approx 10 \ldots 11$ m major radius while conservative assumptions would significantly increase the radius to $R \approx 14 \ldots 15$ m. This is also confirmed by the scenarios with different density profile forms and anomalous transport models which are in the same overall range between $10 \ldots 15$ m.

Outlook

The 1-D code [5] is a very useful tool for scaling procedures and physic investigations. The high flexibility of the code with respect to variables allow to study a variety of scenarios. The knowledge gained from the basic studies of this work could well be used for future studies. A lacking element is the anomalous transport model. It is therefore reasonable to incorporate gyrokinetic simulation results into the 1-D code. It is open, however, to what extent 'simple' anomalous transport models can be developed describing gyrokinetic results. A refined anomalous transport model in combination with an optimised reactor like magnetic configuration could be the first major step to an ITER-like Stellarator or DEMO. Additionally the strong impact of the technology on reactor performance suggests a technological investigation of such devices. Therefore, future studies should also integrate technological and physics aspects. An attempt could be to employ a so-called systems code [74].

In the course of this work hollow density profiles were studied for the first time in a reactor context compared to previous investigations [42]. As the profile was taken from LHD it should be explored, whether such profiles develop in W7-X, and if so to what extent. Furthermore it is mandatory to examine how such a profile can be controlled. Properties and possibilities of this approach should be investigated further, especially the impact on impurities and helium ash in a burning plasma.

Bibliography

[1] "Summary of the ITER final Design Report." International Atomic Energy Agency, Vienna (2001).

[2] G. Grieger and I. Milch. "Das Fusionsexperiment WENDELSTEIN 7-X." *Physikalische Blätter*, vol. 49, p. 1001 (1993).

[3] H. Zohm. "On the minimum size of DEMO." *Fusion Science and Technology*, vol. 58, p. 613 (2010).

[4] C. D. Beidler, E. Harmeyer, F. Herrnegger et al. "The Helias reactor HSR4/18." *Nuclear Fusion*, vol. 41, p. 1759 (2001).

[5] Y. Turkin. Personal communication, Greifswald, 2012.

[6] K. Toi, S. Ohdachi, F. Watanabe et al. "Formation of edge transport barrier in the ergodic field layer of helical divertor configuration on the Large Helical Device." *Plasma Physics and Controlled Fusion*, vol. 48, p. A295 (2006).

[7] S. Fukuda-Parr. "Human Developement Report 2003 - Millennium Developement Goals: A compact among nations to end human poverty." Palgrave Macmillan, Houndmills, Report (2003).

[8] J. Conti. "International Energy Outlook 2011." U.S. Energy Information Administration, Washington (2011). Report.

[9] T. Hamacher and J. Sheffield. "Developement of Fusion Power: What role could fusion power play in transitional and developing countries?" IPP-Report, Max-Planck-Institut für Plasmaphysik (2004).

[10] J. R. Petit, J. Jouzel, D. Raynaud et al. "Climate and atmospheric history of the past 420,000 years from the Vostok ice core, Antarctica." *Nature*, vol. 399, p. 429 (1999).

[11] E. Roeckner, G. Brasseur, M. Giorgetta et al. "Klimaprojektionen für das 21. Jahrhundert." Max-Planck-Institut für Meteorologie (2006).

[12] A. M. Bradshaw, T. Hamacher and U. Fischer. "Is nuclear fusion a sustainable energy form?" *Fusion Engineering and Design*, vol. 86, p. 2770 (2010).

[13] H.-S. Bosch and G. M. Hale. "Improved formulas for fusion cross-sections and thermal reactivities." *Nuclear Fusion*, vol. 32, p. 611 (1992).

[14] J. R. Roth. *Introduction to Fusion Energy*. Ibis Publishing, Charlottesville (1986).

[15] M. S. Weston. *Fusion: An introduction to the Physics and Technology of Magnetic Confinement Fusion*. Wiley-VCH, Weinheim (2010).

[16] R. König, P. Grigull, K. McCormick et al. "The Divertor Program in Stellarators." *Plasma Physics and Controlled Fusion*, vol. 44, p. 2365 (2002).

[17] R. König, P. Grigull, K. McCormick et al. "Divertors for helical devices: concepts, plans, results and problems." *Fusion Science and Technology*, vol. 46, p. 152 (2004).

[18] E. Strumberger. "SOL Studies for W7-X based on the island divertor concept." *Nuclear Fusion*, vol. 36, p. 891 (1996).

[19] N. Ohyabo, T. Watanabe, H. Ji et al. "The Large Helical Device (LHD) helical divertor." *Nuclear Fusion*, vol. 34, p. 387 (1994).

[20] F. F. Chen. *Plasma Physics and Controlled Fusion*. Plenum Press, New York (1984).

[21] R. J. Goldston and P. H. Rutherford. *Plasmaphysik*. Vieweg-Verlag, Braunschweig (1998).

[22] L. D. Landau and E. M. Lifschitz. *Lehrbuch der theoretischen Physik, Band 2: Klassische Feldtheorie*. Akademie-Verlag, Berlin (1992).

[23] J. Wesson. *Tokamaks*. Oxford University Press, Oxford, 4th edn. (2011).

[24] A. H. Boozer. "Physics of magnetically confined plasmas." *Reviews of Modern Physics*, vol. 76, no. 4, p. 1071 (2004).

[25] W. D. D'haeseleer, W. N. G. Hitchon, W. I. van Rij et al. *Flux Coordinates and Magnetic Field Structure.* Springer, New York (1991).

[26] F. Scheck. *Theoretische Physik 1 - Mechanik.* Springer, Berlin (2002).

[27] http://www.ipp.mpg.de/ippcms/de/images/pic/images_bereiche/allgemein/380x265/tokamak_schema.gif (2012).

[28] L. Spitzer. "The Stellarator Concept." *Physics of Fluids*, vol. 1, p. 253 (1958).

[29] B. Wolle. "Tokamak plasma diagnostics based on measured neutron signals." *Physics Reports*, vol. 312, pp. 1 (1999).

[30] C. D. Beidler, K. Allmaier, M. Y. Isaev et al. "Benchmarking of the mono-energetic transport coefficients - results from the International Collaboration on Neoclassical Transport in Stellarators (ICNTS)." *Nuclear Fusion*, vol. 51 (2011).

[31] P. Helander and D. J. Sigmar. *Collisional Transport in Magnetized Plasmas.* Cambridge University Press, Cambridge (2002).

[32] A. A. Galeev and R. Z. Sagdeev. "Theory of Neoclassical Diffusion." *Reviews of Plasma Physics*, vol. 7, p. 257 (1979).

[33] A. V. Luikov. *Analytical Heat Diffusion Theory.* Academic Press, New York (1968).

[34] Y. Turkin. "τ_E predictions for W7-X." Talk (2006).

[35] F. L. Hinton and R. D. Hazeltine. "Theory of plasma transport." *Reviews of Modern Physics*, vol. 48, p. 239 (1976).

[36] S. I. Braginskii. "Transport Processes in a Plasma." *Reviews of Plasma Physics*, vol. 1, p. 205 (1965).

[37] U. S. Inan and M. Golkowski. *Principles of Plasma Physics for Engineers and Scientists.* Cambridge University Press, Cambridge (2011).

[38] R. D. Hazeltine and J. D. Meiss. *Plasma Confinement.* Addison-Wesley, Redwood City (1992).

[39] R. D. Hazeltine. "Recursive derivation of drift-kinetic equation." *Plasma Physics*, vol. 15, p. 77 (1973).

[40] J.-Y. Ji. "Drift kinetic equation and neoclassical transport theory." (Logan, 2009). Lecture Notes.

[41] S. P. Hirshman, K. C. Shaing, W. I. van Rij et al. "Plasma transport coefficients for nonsymmetric toroidal confinement systems." *Physics of Fluids*, vol. 29, p. 2951 (1986).

[42] H. Maaßberg, C. D. Beidler and E. E. Simmet. "Density control problems in large stellarators with neoclassical transport." *Plasma Physics and Controlled Fusion*, vol. 41, p. 1135 (1999).

[43] A. Dinklage, T. Klinger and G. Marx, eds. *Plasma Physics: Confinement, Transport and Collective Effects.* Springer, Berlin (2005).

[44] M. Hirsch, J. Baldzuhn, C. D. Beidler et al. "Major results from the stellarator Wendelstein 7-AS." *Plasma Physics and Controlled Fusion*, vol. 50, p. 053001 (2008).

[45] F. Ryter. "Electron heat transport studies." *Plasma Physics and Controlled Fusion*, vol. 48, p. B453 (2006).

[46] V. Kornilov. *Global Ion-Temperature-Gradient Driven Instabilities in Stellarators within Two-Fluid and Gyrokinetic Descriptions.* Ph.D. thesis, Ernst-Moritz-Arndt-Universität Greifswald (2004).

[47] P. Xanthopoulos, F. Merz, T. Görler et al. "Nonlinear Gyrokinetic Simulations of Ion-Temperature-Gradient Turbulence for the Optimized Wendelstein 7-X Stellarator." *Physical Review Letters*, vol. 99, p. 035002 (2007).

[48] E. Buckingham. "On Physically Similar Systems." *Physical Review*, vol. 4, p. 345 (1914).

[49] J. W. Connor and J. B. Taylor. "Scaling Laws for Plasma Confinement." *Nuclear Fusion*, vol. 17, p. 1047 (1977).

[50] C. C. Petty. "Sizing up plasmas using dimensionless parameters." *Physics of Plasmas*, vol. 15, p. 080501 (2008).

[51] B. B. Kadomtsev. "Tokamaks and dimensional analysis." *Soviet Journal of Plasma Physics*, vol. 1, p. 295 (1975).

[52] H. Yamada, J. H. Harris, A. Dinklage et al. "Characterization of energy confinement in net-current free plasmas using the extended International Stellarator Database." *Nuclear Fusion*, vol. 45, p. 1684 (2005).

[53] C. D. Beidler, E. Harmeyer, F. Herrnegger et al. "Stellarator Reactor Concepts." IPP-Report, Max-Planck-Institut für Plasmaphysik.

[54] F. Schauer. "Coil winding pack FE-analysis for a HELIAS reactor." *Fusion Engineering and Design*, vol. 86, p. 636 (2011).

[55] K. Lackner. "Dimensionless engineering variables for measuring the iter and reactor relevance of tokamak experiments." *Fusion Science and Technology*, vol. 54, p. 989 (2008).

[56] A. Dinklage. Personal communication, Greifswald, 2012.

[57] Y. Turkin, H. Maaßberg, C. D. Beidler et al. "Current Control by ECCD for W7-X." *Fusion Science and Technology*, vol. 50, p. 387 (2006).

[58] Y. Turkin. "Annual Report IPP 2011." Max-Planck-Institut für Plasmaphysik, p. 99 (2011).

[59] K. C. Shaing. "Stability of the radial electric field in a nonaxisymmetric torus." *Physics of Fluids*, vol. 27, p. 1567 (1984).

[60] H. Maaßberg, R. Burhenn, U. Gasparino et al. "Experimental and neoclassical electron heat transport in the LMFP regime for the stellarators W7A, L2 and W7AS." *Phyiscs of Fluids B: Physics of Plasmas*, vol. 5, p. 3627 (1993).

[61] W. I. van Rij and S. P. Hirshman. "Variational bounds for transport coefficients in threedimensional toroidal plasmas." *Phyiscs of Fluids B: Physics of Plasmas*, vol. 1, p. 563 (1989).

[62] Y. Turkin, C. D. Beidler, H. Maaßberg et al. "Neoclassical transport simulations for stellarators." *Physics of Plasmas*, vol. 18, p. 022505 (2011).

[63] H. Maaßberg, R. Brakel, R. Burhenn et al. "Transport in stellarators." *Plasma Physics and Controlled Fusion*, vol. 35, p. B319 (1993).

[64] U. Stroth. "A comparative study of transport in stellarators and tokamaks." *Plasma Physics and Controlled Fusion*, vol. 40, p. 9 (1998).

[65] M. Kikuchi, K. Lackner and M. Q. Tran, eds. *Fusion Physics*. International Atomic Energy Agency (2012).

[66] A. Weller. "International Stellarator/Heliotron Database progress on high-beta confinement and operational boundaries." *Nuclear Fusion*, vol. 49, p. 065016 (2009).

[67] H. Wobig, T. Andreeva, C. D. Beidler et al. "Concept of Helias ignition experiment." *Nuclear Fusion*, vol. 43, p. 889 (2003).

[68] A. Dinklage, H. Maaßberg, R. Preuss et al. "Physical model assessment of the energy confinement time scaling in stellarators." *Nuclear Fusion*, vol. 47, p. 1265 (2007).

[69] https://ishpdb.ipp-hgw.mpg.de/ISS/public/index.html (18.12.2012).

[70] https://ishpdb.ipp-hgw.mpg.de/ISS/public/ISHPDB_public/devices/LHD/data/050000/054167/UFILE/lhd_054167_001856_v0001_2d.dat (18.12.2012).

[71] C. Beidler. Personal communication, Greifswald, 2012.

[72] M. Dimits, G. Bateman, M. A. Beer et al. "Comparisons and physics basis of tokamak transport models and turbulence simulations." *Physics of Plasmas*, vol. 7, p. 969 (2000).

[73] R. C. Wolf. "Characterization of ion heat conduction in JET and ASDEX Upgrade plasmas with and without internal transport barriers." *Plasma Physics and Controlled Fusion*, vol. 45, p. 1757 (2003).

[74] D. J. Ward. "Newly Developing Conceptions of DEMOs: Pulsing and Hydrogen." *Fusion Science and Technology*, vol. 56, p. 581 (2009).

[75] H.-S. Bosch. "Die Physik der Alpha-Teilchen in einem Fusionsreaktor mit Deuterium-Tritium-Plasmen." IPP-Report, Max-Planck-Institut für Plasmaphysik (1999).

[76] W. Heisenberg. *Physik und Philosophie*. S. Hirzel Verlag, Stuttgart (1984).

[77] W. Horton. "Drift waves and transport." *Reviews of Modern Physics*, vol. 71, p. 735 (1999).

[78] J. Johner. "HELIOS: A zero-dimensional Tool for next step Reactor Studies." *Fusion Science and Technology*, vol. 59, p. 308 (2011).

[79] G. Rudolph. "Vorlesungen zur Mathematischen Physik." (Leipzig, 2012). Teil I: Mannigfaltigkeiten, Tensorfelder und Hamiltonsche Systeme.

[80] F. W. Warner. *Foundations of Differentiable Manifolds and Lie Groups*. Springer, Berlin (1983).

Declaration of authorship

Hereby I, Felix Warmer, declare that this master thesis has been written entirely by my own without any assistance from third parties and without sources others than those indicated in the thesis itself. All passages of the work, taken from published and unpublished sources or documents have been mentioned as such. Moreover I declare, that this thesis, in same or similar form, has neither been available to any other authority.

Felix Warmer

I agree, that after positive assessment this work will be available in the library of University Leipzig and in the document archive of IPP.

Felix Warmer